
Electronic Thesis and Dissertation Repository

8-4-2015 12:00 AM


Signal Processing Methods for Quantitative Power Doppler Microvascular Angiography

Mai H. Elfarnawany
The University of Western Ontario

Supervisor
James C. Lacefield
The University of Western Ontario

Graduate Program in Biomedical Engineering
A thesis submitted in partial fulfillment of the requirements for the degree in Doctor of
Philosophy
© Mai H. Elfarnawany 2015

Follow this and additional works at: <https://ir.lib.uwo.ca/etd>

 Part of the [Bioimaging and Biomedical Optics Commons](#), [Biomedical Devices and Instrumentation Commons](#), and the [Other Biomedical Engineering and Bioengineering Commons](#)

Recommended Citation

Elfarnawany, Mai H., "Signal Processing Methods for Quantitative Power Doppler Microvascular Angiography" (2015). *Electronic Thesis and Dissertation Repository*. 3106.
<https://ir.lib.uwo.ca/etd/3106>

This Dissertation/Thesis is brought to you for free and open access by Scholarship@Western. It has been accepted for inclusion in Electronic Thesis and Dissertation Repository by an authorized administrator of Scholarship@Western. For more information, please contact wlsadmin@uwo.ca.

**SIGNAL PROCESSING METHODS FOR QUANTITATIVE POWER DOPPLER
MICROVASCULAR ANGIOGRAPHY**

(Thesis format: Integrated Article)

by

Mai Hafez El-Khaled Elfarnawany

Graduate Program in Biomedical Engineering

A thesis submitted in partial fulfillment
of the requirements for the degree of
Doctor of Philosophy

The School of Graduate and Postdoctoral Studies
The University of Western Ontario
London, Ontario, Canada

© Mai H. Elfarnawany 2015

Abstract

Operator-dependent instrument settings and the likelihood of image artifacts are two challenges for reliably using three-dimensional (3-D) power Doppler angiography in flow depiction and quantification applications.

To address the operator-dependent settings challenge, an automated method for wall filter cut-off selection, the *wall filter selection curve* (WFSC) method, was developed using flow-phantom images. The flow-phantom WFSCs guided the development of a theoretical signal model relating color pixel density (CPD) and wall filter cut-off frequency. Simulations using the theoretical model were used to define criteria for the WFSC method to be applied to unprocessed power Doppler signals from 3-D vasculature. The adapted WFSC method was combined with a 3-D skeletonization and vessel network reconstruction method to present a two-stage processing method aimed at improving vascular detection, visualization and quantification. The two-stage method was evaluated using two *in vivo* models; a murine tumor model was used to test the performance of the method in a flow quantification application and a chick embryo chorioallantoic membrane (CAM) model was used to evaluate the method's value for flow depiction applications.

Applying the WFSC method to flow-phantom images improved vessel delineation and vascular quantification to within 3% of the vascular volume fraction of the phantom. Criteria for the WFSC method from the simulations were to assess at least 100 cut-off frequencies and that the CPD variability should be less than 5% to ensure quantification accuracy. Large variations in the cut-off frequency selected using the WFSC among images acquired at different time points and across different animals in the murine tumor model signified the relevance of spatially and temporally adjusting the cut-off frequency. The two-stage method improved visualization of the vascular network and significantly reduced artifacts in both the tumor and CAM models in comparison to images using conventional Doppler processing. In the CAM model, vessel diameters measured in two-stage processed images were more accurate than measurements in images exported from a commercial scanner. The proposed signal processing methods increase accuracy and robustness of

qualitative and quantitative studies using 3-D power Doppler angiography to assess vascular networks for flow depiction and quantification.

Keywords:

Power Doppler ultrasound, microvascular imaging, quantitative angiography, preclinical imaging, cancer imaging, clutter filtering, three-dimensional vascular networks, vascularization index, vascularization flow index, power Doppler signal modelling, blooming artifact.

Co-Authorship Statement

Chapter 2 was published in *Ultrasound in Medicine and Biology* as: **M. Elfarnawany**, S. Z. Pinter, and J. C. Lacefield, "Improved objective selection of power Doppler wall-filter cut-off velocity for accurate vascular quantification," *Ultrasound Med. Biol.*, vol. 38, p. 1429, 2012. All authors contributed to editing the paper. The flow-phantom images used to evaluate the presented method were acquired by Stephen Pinter, a former Ph.D. student in Dr. Lacefield's laboratory. I redesigned the original wall filter selection curve method developed by Dr. Pinter by developing the automatic characteristic-interval detection and the cut-off frequency selection algorithms. I developed image processing methods and segmented the flow-phantom images to create reference masks for method evaluation. I tested the new method by applying to the flow phantom images and conducted analysis and statistical comparisons on the produced data. I worked on this project under the supervision of Dr. Lacefield.

Chapter 3 was published in *SPIE Conference Proceedings* as: **M. Elfarnawany** and J. C. Lacefield, "A new three-component signal model to objectively select power Doppler wall filter cut-off velocity for quantitative microvascular imaging," *Proc. SPIE*, vol.8670, article 86750J, 2013. Both authors contributed to editing the paper. For this paper, I developed the new signal model by constructing its equations and defining its constituting distributions. I developed the cost function used as a reference for the optimum cut-off selection. I conducted the simulations using the new model and performed all analysis and statistical comparisons on the simulation results. I worked on this project under the supervision of Dr. Lacefield.

Chapter 4 is in preparation to be submitted to: *Ultrasound in Medicine and Biology* as: **M. Elfarnawany**, M. R. Lowerison, M. N. Hague, A. F. Chambers and J.C. Lacefield, "A two-stage process to improve quantitative three-dimensional power Doppler angiography of tumor microvasculature." Matthew Lowerison, a Ph.D. student in Medical Biophysics and a member of Dr. Lacefield's laboratory and Nicole Hague, a laboratory technician in Dr. Chambers' laboratory, were responsible for animal models, including animal handling, animal care, cell injections and coordinating the necessary surgeries for creating the mouse

models. The power Doppler and contrast-enhanced ultrasound (CEUS) images of the tumor vasculature used in this study were acquired by Matthew, who was also responsible for computing CEUS quantification metrics. I was responsible for the development power Doppler processing software to produce 3-D images from quadrature demodulated data exported from the scanner. I developed and incorporated the two-stage method and power Doppler quantification metrics computations in the Doppler processing software. I processed and segmented all the acquired tumor power Doppler images and performed all post-analysis and statistical comparisons on resulting images and quantification. I worked on this project under the supervision of Dr. Lacefield.

Chapter 5 is in preparation to be submitted to *IEEE Transactions on Medical Imaging* as: **M. Elfarnawany**, N. Govindaraju, S. Pardhan, A. Makela, P. Foster, H. S. Leong, J. C. Lacefield, “Improving microvascular depiction in three-dimensional power Doppler ultrasound using a two-stage processing method,.” Nivitha Govindaraju, a summer student in Dr. Lacefield’s laboratory, and I worked on developing the optical image processing methods. Siddika Pardhan, a laboratory assistant in Dr. Leong’s laboratory at the time, prepared the *ex ovo* chick embryo based on the protocol developed in Dr. Leong’s laboratory. Ashley Makela, an Ontario-licensed sonographer and a master’s student in Medical Biophysics and a member of Dr. Fosters laboratory, help set up the power Doppler instrument settings during image acquisition sessions. I was responsible for conducting the experiment including transporting the chick embryos, experimental setup and image acquisition. I processed all the acquired power Doppler images and made all diameter measurements of the imaged vascular network. I performed all post-analysis and statistical comparisons on processed images and measurements. I worked on this project under the supervision of Dr. Lacefield.

*This thesis is dedicated to the shining lights in my path,
my son, Belal, my husband, Karim, my mother,
Hanan and my father, Khaled,
without you all I would lose my way.*

Acknowledgments

These last five years mark a transformational phase of my life during which I was privileged to meet and work with many fantastic people from the Robarts Research Institute and Western University communities.

First of all, I'd like to acknowledge my supervisor, Dr. James Lacefield, for giving me the freedom to explore, develop and tune my research directions while maintaining the balance of continuous follow-up on my progress. Dr. Lacefield has always been very supportive of my work and has enriched my experience as a graduate student with needed skills to lead a fruitful career after graduation. He always encouraged me to present my progress in conferences and he has a major role in developing my writing skills. With Dr. Lacefield's passion for teaching what he knows best, I have learned during the time I spent in his lab about ultrasound way beyond the scope of my project and more than what I have learned during all my undergraduate years.

I would like to thank my advisory committee: Dr. Tamie Poepping, Dr. Ting-Yim Lee, and Dr. Kevin Shoemaker. They were available to answer questions when needed and have provided insightful suggestions and comments that helped guide my research direction and design suitable studies for a smooth transition between my project phases. Dr. Poepping has also played the role of a supportive mentor and friend.

I also have to acknowledge present and past members of the Lacefield lab. Matthew Lowerison has been a great co-worker, acquiring all the images for my study in Chapter 4 and he is our contrast-enhanced ultrasound expert. We have had many great discussions about our projects and I have benefited from Matthew's strong physics background and analytical approach to tackle abstract concepts. Dr. Stephen Pinter laid the foundation for my project and provided me with a very organized and comprehensive data set, which I was able to directly use to evaluate my developed methods in Chapters 2 and 3. Previous lab members, Christopher Waring and Adem Hadj Boussaad and present members: Szymon Kowal and Omar Mansour, it has been great getting to know you and your expertise have been a

welcome help. Special thanks to Nivetha Govindaraju, our summer student who helped develop image-processing algorithm for the study in Chapter 5. Her enthusiasm, fast learning and speedy progress made working with her a delightful experience. I wish her luck in her future steps and career.

A thank you to our collaborators and co-authors from Dr. Ann Chambers, Dr. Hon Leong and Dr. Paula Foster labs. Special thanks to Nicole Hague from Dr. Chamber's lab who helped with the mouse model used in Chapter 4 and to Siddika Pardhan from Dr. Leong's lab who prepared and monitored the development of the chick embryo model used in Chapter 5. The study in Chapter 5 would not have been completed without the help of our licensed sonographer, Ashley Makela from Dr. Foster's lab who helped set the gold standard for the study in Chapter 5 by setting up the scanner using the set of optimum machine settings.

Thank you to Darlene Goodine for all the administrative help and guidance when I first joined Robarts. To Christine Ellwood, the current Biomedical Engineer Program Coordinator for her administrative help. An enormous thanks to our famous past BME coordinator, Diana Timmermans. Diana made the BME program run smoothly and was always there for students no matter when or for what. She played an important role in helping me apply for this program and matching my research interests with Dr. Lacefield's lab research focus. Diana was a fantastic person to work with and an even better person to get to know as a friend. I would like to add a thank you to Ann Leaist; we've spent most of the past few years in the same area in Robarts and she has always added a bit of cheer to the day and I will surely miss her occasional treats and chocolates.

Thanks to many people who provided valuable advice and feedback or shared brilliant ideas in casual chats in Robarts hallways. To Dr. Grace Parraga, Dr. Terry Peters, Dr. Jim Johnson, Dr. Aaron Fenster, Dr. Ali Tavallaei and Dr. Eli Gibson. To Mariama Henry, my lunchtime buddy and to Dr. Nour Ghonaim with whom I had many academic-related chats and who has become a dear friend to me.

I would like to acknowledge my funding sources over the years. I was funded by the Ontario Graduate Scholarships for 2011-2012 and by the National Science and Engineering Research Council from 2012 to 2015. I would also like to acknowledge funding and support from the UWO CIHR Strategic Training Program and the Western Graduate Research Scholarship.

To my friends who supported me and listened attentively to my stories of success or failure and gave me advice to help me keep going. To my best friend and true sister, Mariam El-feky who has always been and will continue to be my secret-keeper and my representative in all the events I have missed in Egypt while working on this degree. Your weekly phone call was like the fuel that keeps me motivated for the following week. A special thanks to my great friend Somiraa Said, who was my go to academic source of information and advice and my true friend away from home. Thank you for accepting to join me in my random spurts of having dinner out or going for ice-cream or even middle of the day shopping sprees. You and your amazing family have really filled the void of having family friends away from home.

To my family, thank you for being there through all my ups and downs, my frustrations and failed experiments, for supporting all my decisions and helping me take the next step. To my mother, Hanan Ezz Eldin, who has heard my tiniest details of progress everyday for five years through a long-distance phone call. Who has taught me how to always do everything in the best way I could and always reminded me of why I am doing what I am doing and what am I trying to reach. My mother is the one who laid the foundation of my character and my approach in life, and for that I can never ever thank her enough. To my father, Khaled Elfarnawani, the best role model one can ever have. He was always there for all my firsts, first presentation, first paper submission and even during my final stages of writing this thesis, he was just always there supporting me and cheering for me to continue, my father is just always there for support. To my young brothers, Ahmed and Osama, who even though are younger than me have always taught me new ways of looking at life, have given me that concealed support by the admiration in their eyes when they look at me. May you always achieve much more than you aim for and reach much higher ranks than you think you can reach.

Lastly but certainly not least, to my husband Karim and my baby Belal. Karim, you are my partner on this path to our common ultimate goal, my friend, and my sole mate. I can never ever thank you enough for being the main role player in my Ph.D. story. For all your support and patience, for listening to my presentation rehearsals hundreds of times and accompanying me on all my conference trips. and for proof reading my articles. For helping with Belal and accepting the occasional “Let’s order pizza” suggestions. For being so encouraging that you even know all the details of my work to the level that you can present it in a conference!. You were there all through and especially these last few months, your patience and understanding cannot be ever thanked enough. For Belal, my baby who spent long days in daycare since he was just six months old. Thank you Belal for letting me finish this degree and always motivating me with your happiness and laughter. You have added so much light to our life and filled our days with purity and unprecedented sense of accomplishment as we saw you grow, walk, talk and play. May you always be one of the righteous and grow to be an amazing man like your father.

And certainly, All praise is due to Allah the most Gracious the most Merciful.

الحمد لله رب العالمين

Table of Contents

| | |
|---------------------------------------------------------------|-------------|
| Abstract..... | ii |
| Co-Authorship Statement | iv |
| Acknowledgments | vii |
| Table of Contents | xi |
| List of Tables | xvi |
| List of Figures..... | xvii |
| List of Symbols | xx |
| List of Acronyms and Abbreviations | xxii |
| Chapter 1 | 1 |
| Introduction | 1 |
| 1.1 Overview..... | 1 |
| 1.2 The Age of Vascular Imaging..... | 2 |
| 1.3 Vascular Imaging Techniques..... | 2 |
| 1.3.1 X-Ray Catheter Angiography | 3 |
| 1.3.2 Computed Tomography (CT) Angiography | 3 |
| 1.3.3 Magnetic Resonance Angiography (MRA) | 3 |
| 1.3.4 Ultrasound..... | 4 |
| 1.4 Overview of Doppler Ultrasound Imaging | 5 |
| 1.4.1 The Doppler Equation..... | 5 |
| 1.4.2 Continuous-wave (CW) and pulsed-wave (PW) Doppler | 6 |
| 1.4.3 Principles of Doppler Color Flow Imaging (CFI)..... | 7 |
| 1.5 Power Doppler Imaging Applications | 13 |
| 1.5.1 Vascular Depiction Applications | 14 |

| | | |
|------------------|-----------------------------------------------------------------------------------------------------------------------------|-----------|
| 1.5.2 | Vascular Quantification Applications..... | 15 |
| 1.6 | Challenges in Power Doppler Imaging..... | 17 |
| 1.6.1 | Operator-Dependant Instrument Settings | 17 |
| 1.6.2 | Image Artifacts..... | 19 |
| 1.7 | Attempts to Overcome Challenges | 23 |
| 1.7.1 | Optimizing Instrument Settings using Flow Phantoms | 23 |
| 1.7.2 | Developing Application-Based Instrument Settings Standard | 23 |
| 1.7.3 | Optimizing Wall / Clutter Filter Processing | 24 |
| 1.7.4 | Image Post-Processing Methods to Reduce Artifacts..... | 25 |
| 1.8 | Hypothesis and Objectives..... | 26 |
| 1.9 | Thesis Outline..... | 27 |
| | References | 30 |
| Chapter 2 | | 41 |
| | Improved objective selection of power Doppler wall-filter cut-off velocity for accurate vascular quantification..... | 41 |
| 2.1 | Introduction..... | 41 |
| 2.2 | Materials and Methods..... | 45 |
| 2.2.1 | Dividing an ROI into subregions | 45 |
| 2.2.2 | Detection of characteristic intervals in a WFSC..... | 46 |
| 2.2.3 | Selection of operating cut-off velocity along a characteristic interval | 49 |
| 2.2.4 | ROI reconstruction..... | 50 |
| 2.2.5 | Power Doppler image acquisition..... | 50 |
| 2.2.6 | Performance analysis of WFSC method..... | 52 |
| 2.3 | Results..... | 53 |
| 2.3.1 | Characteristic interval detection | 53 |
| 2.3.2 | Selection of an operating point cut-off velocity | 55 |

| | |
|--------------------------------------------------------------------------------------------------------------------------------------------------------|-----------|
| 2.3.3 Reconstructed images | 56 |
| 2.4 Discussion | 57 |
| 2.5 Conclusion | 63 |
| References | 65 |
| Chapter 3 | 68 |
| A new three-component signal model to objectively select power Doppler wall filter cut-off velocity for quantitative microvascular imaging..... | 68 |
| 3.1 Introduction..... | 68 |
| 3.2 Materials and Methods..... | 71 |
| 3.2.1 Revised Mathematical Model | 71 |
| 3.2.2 Cost Function | 74 |
| 3.2.3 Generation of Simulated WFSCs and Cost Functions | 75 |
| 3.2.4 Performance Analysis of the WFSC Method..... | 76 |
| 3.3 Results..... | 79 |
| 3.3.1 Revised Mathematical Model | 79 |
| 3.3.2 Performance Analysis of the WFSC Method..... | 80 |
| 3.4 Discussion..... | 85 |
| 3.5 Conclusion | 90 |
| References | 91 |
| Chapter 4 | 93 |
| A two-stage process to improve quantitative three-dimensional power Doppler angiography of tumor microvasculature | 93 |
| 4.1 Introduction..... | 93 |
| 4.2 Materials and Methods..... | 96 |
| 4.2.1 Experimental Image Acquisition | 96 |
| 4.2.2 The WFSC method | 97 |
| 4.2.3 Vascular network skeletonization and reconstruction | 98 |

| | | |
|------------------|---------------------------------------------------------------------------------------------------------------------------------|------------|
| 4.2.4 | Applicability of WFSC method to tumor vascular imaging | 98 |
| 4.2.5 | Effect of WFSC method and skeletonization on vascular network visualization | 100 |
| 4.2.6 | Effect of WFSC method and skeletonization on vascular quantification | 100 |
| 4.3 | Results..... | 103 |
| 4.3.1 | Characteristics of WFSCs for tumor images | 103 |
| 4.3.2 | Histograms of WFSC-selected cut-off frequency..... | 103 |
| 4.3.3 | Longitudinal variability of WFSC-selected cut-off frequency | 106 |
| 4.3.4 | Vascular features corresponding to WFSC-selected cut-off frequency.. | 107 |
| 4.3.5 | Effect of WFSC method and skeletonization on vascular network visualization | 108 |
| 4.3.6 | Effect of WFSC method and skeletonization on vascular quantification | 109 |
| 4.4 | Discussion..... | 112 |
| 4.5 | Conclusion | 120 |
| | References | 121 |
| Chapter 5 | | 125 |
| | Improving microvascular depiction in three-dimensional power Doppler ultrasound using a two-stage processing method..... | 125 |
| 5.1 | Introduction..... | 125 |
| 5.2 | Material and Methods | 127 |
| 5.2.1 | Materials | 127 |
| 5.2.2 | Experimental protocol..... | 128 |
| 5.2.3 | Image acquisition | 128 |
| 5.2.4 | Image processing | 129 |
| 5.2.5 | Data analysis | 134 |
| 5.2.6 | Statistical analysis..... | 135 |
| 5.3 | Results..... | 136 |

| | | |
|-------------------------------------------------------------|-------------------------------------------------------------------------------------------------------------------------------------------------------------|------------|
| 5.3.1 | Vessel detection and visualization | 136 |
| 5.3.2 | Level of striping artifact..... | 139 |
| 5.3.3 | Accuracy of diameter measurement..... | 140 |
| 5.4 | Discussion..... | 146 |
| 5.5 | Conclusion | 151 |
| | References..... | 152 |
| Chapter 6 | | 157 |
| | Summary and Future Work..... | 157 |
| 6.1 | Summary..... | 157 |
| 6.1.1 | Chapter 2: Improved objective selection of power Doppler wall-filter cut-off velocity for accurate vascular quantification | 157 |
| 6.1.2 | Chapter 3: A new three-component signal model to objectively select power Doppler wall filter cut-off velocity for quantitative microvascular imaging | 158 |
| 6.1.3 | Chapter 4: A two-stage process to improve quantitative three-dimensional power Doppler angiography of tumor microvasculature | 159 |
| 6.1.4 | Chapter 5: Improving microvascular depiction in three-dimensional power Doppler ultrasound using a two-stage processing method | 159 |
| 6.2 | Future Work..... | 160 |
| 6.3 | Final Remarks..... | 161 |
| | References..... | 162 |
| Appendix A: Copyright Agreements..... | | 163 |
| Appendix B: Ethics Approval for Animal Subjects..... | | 164 |
| Curriculum Vitae..... | | 165 |

List of Tables

| | |
|---------------------------------------------------------------------------------------------------------------------------------------------------------------|-----|
| Table 2-1: Variation of selected cut-off velocities among subregions of high, medium, and low vascularity ROIs..... | 56 |
| Table 2-2: Relative accuracy of quantification of blood flow for high, medium, and low vascularity ROIs..... | 57 |
| Table 3-1: Ranges of variation of vascular parameters for the numerical analysis | 76 |
| Table 4-1: Effect of WFSC and skeletonization algorithms on power Doppler quantification metrics, VI, FI and VFI for overall and intra-tumor vasculature..... | 111 |
| Table 4-2: Correlation between power Doppler and CEUS quantification for overall and intra-tumor vasculature. | 112 |
| Table 5-1: Number and sizes of vessels depicted in two-stage processed images only. | 138 |
| Table 5-2: The number and mean diameter measurements of vessels of different orders used in this study. | 142 |

List of Figures

| | |
|-----------------------------------------------------------------------------------------------------------------------------------------------------------------------------------|----|
| Figure 1-1: Doppler effect: (a) the frequency of the reflected ultrasound wave from a moving target (red blood cells (RBC)) is different than the transmitted wave..... | 6 |
| Figure 1-2: A sample block diagram of Doppler color flow imaging system constituting of 2 sections: (a) Doppler Signal acquisition section and (b) Doppler Signal Processing..... | 7 |
| Figure 1-3: Illustration of hypothetical Doppler signal frequency spectrum..... | 11 |
| Figure 1-4: Sample Doppler color flow images of human right kidney using (a) color Doppler display mode showing only large vessels and (b) power Doppler mode..... | 14 |
| Figure 1-5: An example of a commercial power Doppler system (Vevo2100, VisualSonics, Toronto, Canada) user panel..... | 19 |
| Figure 1-6: Blooming artifact in a power Doppler image..... | 20 |
| Figure 1-7: Jail bar artifact in a power Doppler image..... | 22 |
| Figure 2-1: Theoretical wall-filter selection curve (Eqn 2-1) for a region of interest containing two vessels. | 44 |
| Figure 2-2: Iterative detection of characteristic intervals. | 48 |
| Figure 2-3: Flow chart for selection of an operating point cut-off velocity along a characteristic interval. | 51 |
| Figure 2-4: Image improvement produced by the redesigned wall filter selection curve (WFSC) method. | 54 |
| Figure 2-5: Analysis of accuracy of the selection of operating point cut-off velocity. | 55 |
| Figure 2-6: Original method for detecting characteristic intervals. | 59 |

| | |
|-------------------------------------------------------------------------------------------------------------------------------------------------------------------------------|-----|
| Figure 2-7: Effects of non-uniform and insufficient sampling of the wall filter selection curve (WFSC)..... | 60 |
| Figure 3-1: Theoretical wall filter selection curves (blue lines) fitted to experimental multiple-vessel flow-phantom data..... | 74 |
| Figure 3-2: A sample cost function (solid line) is produced from a weighted combination of false-positive (dashed line) and false-negative (dotted line) error fraction | 75 |
| Figure 3-3: The mean interval detection error (solid line) plotted as a function of the number of samples. | 80 |
| Figure 3-4: The correspondence between operating cut-off velocity selections using the automatic algorithm and the perfect binary selection method. | 82 |
| Figure 3-5: The relative vascular quantification error using the automatic algorithm as a function of the CPD value at the optimum cut-off velocity..... | 83 |
| Figure 3-6: Theoretical distribution of the vascular quantification error as a function of the interval length | 84 |
| Figure 3-7: Theoretical distribution of the vascular quantification error as a function of the minimum cut-off velocity | 85 |
| Figure 4-1: Sample WFSC curves constructed from (a) a multiple-vessel flow phantom and (b) an <i>in vivo</i> murine tumor model. | 104 |
| Figure 4-2: Variability of WFSC-selected cut-off frequency in 3-D images. | 105 |
| Figure 4-3: Longitudinal variations in cut-off frequency histograms as tumors grow | 106 |
| Figure 4-4: Longitudinal comparison of vascular features in the low and high-cut-off frequency portions of the 3-D vascular network identified using the WFSC method..... | 108 |
| Figure 4-5: Effect of WFSC method and skeletonization algorithm on tumor vasculature visualization | 110 |

| | |
|--------------------------------------------------------------------------------------------------------------------------------------------------------------------------|-----|
| Figure 4-6: Longitudinal trends of power Doppler quantification metric: | 119 |
| Figure 5-1: A sample optical photograph showing (a) the full vascular network of the chick embryo chorioallantoic membrane (CAM)..... | 130 |
| Figure 5-2: CAM optical image processing method with samples of results obtained at different stages of processing..... | 132 |
| Figure 5-3: Improved vessel detection and visualization in images processed using our two-stage method versus commercial scanner (Vevo 2100) processed images..... | 137 |
| Figure 5-4: Improved vessel detection and visualization in 3-D images processed using our two-stage method versus commercial scanner (Vevo 2100) | 139 |
| Figure 5-5: Quantified level of artifact from images processed using the two-stage method versus the commercial scanner (Vevo 2100) software for different animals. | 141 |
| Figure 5-6: Comparison of the distributions of diameter measurement percentage errors from all 83 vessels | 143 |
| Figure 5-7: Separate comparisons of the distributions of diameter measurement percentage errors for (a) arteries and (b) veins | 145 |
| Figure 5-8: Box plot evaluation of the performance of the two-stage methods versus the commercial scanner (Vevo 2100) processing. | 146 |

List of Symbols

| | |
|-----------------------|--------------------------------------------------------------------------------------------------------|
| f_r | the reflected ultrasound frequency |
| f_0 | the ultrasound transmit frequency |
| v | the target velocity |
| θ | the angle between the ultrasound beam and the direction of flow |
| c | the average speed of sound in the imaged tissue |
| v_c | the wall filter cut-off velocity |
| $TPF_i(v_c)$ | the true-positive fraction within the i th vessel |
| $FPF(v_c)$ | the false-positive fraction obtained as the cut-off velocity is varied |
| $F_{v(i)}$ | the volume fraction occupied by the i th vessel |
| CPD_1 & CPD_2 | the CPD values of two successive data points |
| $max(CPD)$ | maximum value of CPD along the WFSC. |
| $ \Delta CPD _{norm}$ | normalized absolute first difference of the CPD |
| w | is a weight parameter used to define the volume fraction of the perivascular compartment |
| ϕ | the standard-normal cumulative density function, $v_c \geq 0$ |
| μ_{ln} | the mean of the natural logarithm of the Doppler velocity estimates |
| σ_{ln} | the standard deviation of the natural logarithm of the Doppler velocity estimates |
| μ_i | the mean of the log-normally distributed velocity estimates for the intravascular pixels |
| σ_i | the standard deviation of the log-normally distributed velocity estimates for the intravascular pixels |
| σ_p | the standard deviations of velocity estimates for the perivascular pixels |
| σ_e | the standard deviations of velocity estimates for the extravascular pixels |

| | |
|-----------|--------------------------------------------------------------|
| U_{IFN} | the utility of the intravascular false-negative color pixels |
| U_{PCP} | the utility of the perivascular false-positive color pixels |
| U_{ECP} | the utility of the extravascular false-positive color pixels |

List of Acronyms and Abbreviations

| | |
|----------------|------------------------------------------------------|
| 2-D | Two-dimensional |
| 3-D | Three-dimensional |
| ANOVA | Analysis of variance |
| CAM | Chorioallantoic membrane |
| CEUS | Contrast enhanced ultrasound |
| CFI | Color flow imaging |
| CPD | Color pixel density |
| cpSNR | Color pixel signal-to-noise ratio |
| CT | Computed Tomography |
| CW | Continuous-wave |
| DCE-CT | Dynamic contrast-enhanced x-ray computed tomography |
| DCE-MRI | Dynamic contrast-enhanced magnetic resonance imaging |
| FI | Flow index |
| FIR | Finite impulse response |
| FPF | False positive fraction |
| ICPF | Intravascular color pixel fraction |
| IFNF | Intravascular false negative fraction |
| IIR | Infinite impulse response |
| IQ | Quadrature demodulated |
| MAPE | Median absolute percentage error |
| MEP | Maximum envelope peak |
| MIP | Mean intensity projection |

| | |
|----------------|-----------------------------------|
| MR | Magnetic resonance |
| MRA | Magnetic resonance angiography |
| MRI | Magnetic resonance imaging |
| PCPF | Perivascular color pixel fraction |
| PD | Power Doppler |
| PDA | Power Doppler angiography |
| PDF | Probability density function |
| PET | Positron emission tomography |
| PRF | Pulse repetition frequency |
| PW | Pulsed-wave |
| RBC | Red blood cell |
| RGB | Red, green, blue |
| ROC | Receiver operator characteristic |
| ROI | Region of interest |
| SEM | Standard error of mean |
| TOST | Two one-sided test |
| TPF | True-positive fraction |
| VFI | Vascularization flow index |
| VI | Vascularization index |
| VOCALTM | Volumetric calculations |
| VOI | Volume of interest |
| WFSC | Wall filter selection curve |

Chapter 1

Introduction

1.1 Overview

Ultrasound is a commonly used imaging technique for vascular imaging. Of the different modes of ultrasound used to display vascular information, power Doppler is characterized by an improved sensitivity and ability to image small vessels or slow flow. However, power Doppler imaging faces some challenges that possibly set limitations on its usability in quantitative microvascular applications.

This thesis presents and evaluates new Doppler signal processing methods to potentially overcome some challenges of using power Doppler imaging in vascular applications. In this thesis, an objective method to automatically select the wall filter cut-off frequency setting is developed and evaluated using flow phantom experiments. Results from these experiments were used to drive adjustments to the theoretical foundation of the method and define conditions needed for an online implementation of the method. These conditions were used to adapt the method to apply to unprocessed power Doppler signals and expand it to function on three-dimensional images. The cut-off selection method was combined with artifact-reduction image post-processing techniques to form a two-stage Doppler processing method. Lastly, in vivo evaluation of the two-stage method performance using a tumor model and a simpler, hierarchal vascular model of the chick embryo chorioallantoic membrane were performed.

In order to provide some context for subsequent chapters, this chapter starts by highlighting the role of vascular imaging in many clinical applications and summarizing and comparing the commonly used vascular imaging techniques for these applications. With the focus of the thesis being power Doppler ultrasound, an overview of Doppler ultrasound imaging explaining some physical principals, imaging system components and operation and different display modes is included. A review of vascular depiction and

quantification applications of power Doppler imaging is presented followed by a summary of the most common challenges in using power Doppler imaging. Finally, an overview of previous attempts to overcome the identified challenges in comparison to the method presented in this thesis followed by a detailed outline of the thesis chapters.

1.2 The Age of Vascular Imaging

As quoted from Gooding's 1999 editorial in *Emergency Radiology*, "the age of vascular imaging is upon us" [1]. With the vascular system being the fundamental communication and transportation vehicle to all body systems and organs, imaging blood vessels and studying its flow characteristics has become an integral part of almost all research efforts targeting the diagnosis, confirmation or interventional treatment of diseases. Vascular imaging is commonly used in cardiovascular, cerebrovascular and peripheral vascular diseases [2]. In the musculoskeletal field, vascular imaging has also become important for the diagnosis of inflamed entities that are linked to their vascular signature [3, 4]. In addition, studying tumor angiogenesis has become the focus of many researchers attempting to identify changes in vasculature as a marker of cancer and then target that vasculature for therapeutic defense [5, 6]. Vascular imaging is also playing an important role in testing the safety and efficacy of new drugs on the vascular systems of the target organs or hosts [1]. With the advancement in imaging technology, vascular imaging tools are now capable of providing three-dimensional (3-D) depictions of anatomical and/or functional features of vasculature. Furthermore, the unparalleled development in image analysis tools over the last three decades has empowered imaging technologies with artifact reduction, realistic visualization and quantification capability of vasculature.

1.3 Vascular Imaging Techniques

There are a number of different vascular imaging techniques that compete on achieving the balance between image quality, degree of invasiveness and cost. Commonly used vascular / angiographic imaging techniques include:

1.3.1 X-Ray Catheter Angiography

Angiography is a term that describes the process of acquiring images of blood vessels, particularly, arteries and veins. X-ray catheter angiography was the mainstay of vascular diagnostic imaging for almost half a century with its excellent spatial and temporal resolution and selective delineation of vessels [4]. In x-ray angiography, images are acquired by transmitting and receiving x-rays through the area of interest after injecting the subject with radio-opaque contrast agent. Rotational angiography presents the 3-D extension of catheter angiography allowing it to compete with the alternative vascular imaging. X-ray angiography is very useful in detecting abnormalities of the vessel lumen: stenosis, occlusion, aneurysms and other irregularities [3]. Nevertheless, its invasive nature, high radiation doses and injection of possibly nephrotoxic contrast media are among its drawbacks [3].

1.3.2 Computed Tomography (CT) Angiography

Computed tomography (CT) angiography allows 3-D imaging of vessels and surrounding structures. Cross sectional images are produced by rotating an x-ray tube 360° around the area of interest and collecting the information using rows of detectors on a circular gantry [7]. These images are assembled by a computer and post-processing methods such as 3-D volume rendering and maximum intensity projection (MIP) maps are used to best demonstrate the acquired information. CT angiography is useful for detecting thrombus, vessel wall thickening, calcification and abnormalities of adjacent structures such as infarction and hemorrhage [3]. Although CT has the highest spatial resolution of all imaging modalities, its high radiation doses and the need for injections of high concentrations of nephrotoxic contrast media limits its use for repeated scanning.

1.3.3 Magnetic Resonance Angiography (MRA)

Magnetic resonance angiography (MRA) allows imaging of blood vessels in several body parts and provides information about the vessel lumen, vessel wall and surrounding structures, thus adding important anatomical information [3]. In general, MR imaging is performed by placing the subject in a strong uniform magnetic field to align the proton spins in the direction of the magnetic field, then collecting the varying signals

from protons within different tissues after being interrogated by a radio-frequency electromagnetic pulse. The advantages of MRA include having high soft-tissue discrimination, no ionizing radiation and safer low-toxicity contrast agents. However, MRA's shortcomings include: prolonged acquisition time, being invasive, lack of information about direction of blood flow as well as some important exclusions [4]. Patients with pacemakers, metal implants, claustrophobia and first-trimester pregnant women are all not candidates for MRA. In addition, different practiced protocols and instrument preferences have a large effect on signal strength, making it difficult to compare data obtained from different instruments [6].

1.3.4 Ultrasound

Ultrasound is a medical imaging technique that uses the variations in transmission and reflection of super-audible range sound waves (*i.e.*, sound waves with frequencies beyond the human audible range of 20 kHz) from different types of tissues to produce images [7]. In the last two decades, ultrasound experts have proceeded to introduce a new area of vascular imaging as instrumentation expanded from real time to duplex Doppler, then color Doppler to power Doppler [1]. With the ability to provide information on both anatomy and flow characteristics, being the least invasive, lack of ionizing radiation, low cost, broad diagnostic applicability, portability and easy handling, ultrasound has become the initial screening and the fast-look follow-up examinations tool [8]. Its high resolution and ability to visualize blood flow using power Doppler as well as blood velocity and direction using color Doppler further extended its application to vascular diagnosis. Challenges for ultrasound imaging include the dependence of the image quality on the skill of the operator, limited field of view, inability to image bony or air-filled structures, and the tradeoff between resolution and depth of penetration when selecting the imaging frequency since sound penetration is best at low frequencies whereas resolution increases with frequency [4]. Limitation and challenges of Doppler ultrasound vascular imaging techniques will be discussed in detail later.

Contrast enhanced ultrasound (CEUS) is another ultrasound-based imaging technique that uses contrast agents, which are gas-filled microbubbles, to improve imaging of blood flow [8]. The highly echogenic microbubbles are injected into the

vasculature and remain in the systemic circulation for a certain amount of time. As these microbubbles pass the imaging window, they reflect echoes that differ significantly in their frequency content from echoes reflected from the surrounding tissue. These reflected echoes are then converted into a contrast-enhanced image of the area of interest. Although CEUS imaging improves flow detection, it is still of limited use in comparison to Doppler flow imaging techniques due to its invasive nature and increased cost of contrast agents.

1.4 Overview of Doppler Ultrasound Imaging

1.4.1 The Doppler Equation

Doppler ultrasound provides information about moving structures in the body by measuring the changes in frequency of an ultrasound wave as it is reflected from a moving target such as flowing blood [7]. This change in frequency is called the Doppler effect and is summarized in Figure1-1(a).

When a target is moving towards the ultrasound source, the frequency of the received wave will be higher than the frequency of the emitted wave, giving a positive Doppler shift signal. A negative Doppler shift signal is acquired when the target is moving away from the ultrasound source. In vascular imaging applications, the Doppler shift frequency $f_{Doppler}$ is related to the velocity of blood v by the Doppler equation:

$$f_{Doppler} = f_r - f_0 = \frac{2f_0v \cos\theta}{c} \quad \text{Eqn. 1-1}$$

where f_r is the reflected ultrasound frequency, f_0 is the ultrasound transmit frequency, v is the target velocity, theta θ is the angle between the ultrasound beam and the direction of flow as shown in Figure 1-1(b) and c is the average speed of sound in the imaged tissue.

Typical ranges of the Doppler shift frequencies are 10Hz-10 kHz corresponding to blood velocities of 1-100 cm s^{-1} [9].

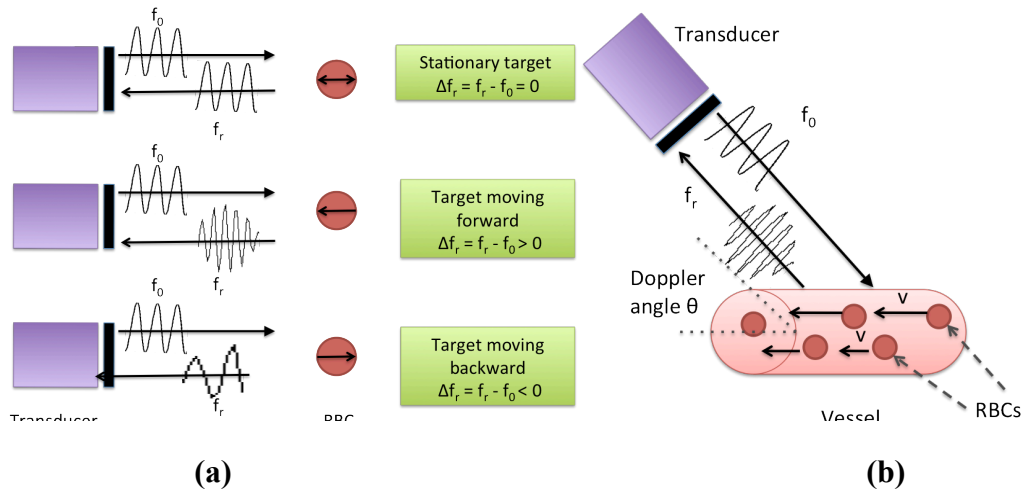


Figure 1-1: Doppler effect: (a) the frequency of the reflected ultrasound wave from a moving target (red blood cells (RBC)) is different than the transmitted wave. The detected frequency is increased or decreased depending on the direction of motion. The Doppler shift frequency is controlled by the Doppler equation (Eqn. 1-1) which is a function of the transmit frequency f_0 , RBCs velocity v , Doppler angle θ .

1.4.2 Continuous-wave (CW) and pulsed-wave (PW) Doppler

In general, Doppler systems for ultrasound-based flow estimation can be broadly categorized based on their excitation methods into: continuous-wave (CW) systems and the pulsed-wave (PW) systems [9]. The CW Doppler system is based on the use of continuous ultrasound waves, and it estimates flow velocities by measuring the Doppler frequency shifts between the transmitted wave and the received echoes. On the other hand, the PW Doppler system is based on the use of finite-duration ultrasound pulses, and it estimates flow velocities by measuring the time shifts between pulse echoes. In modern imaging instruments, pulsed-wave (PW) Doppler has virtually replaced CW Doppler as it allows more localization of the signal source within the field of view [9].

The Doppler shift signal acquired from a pulsed wave (PW) Doppler system contains a wealth of information, which can be displayed in a few ways [7]. A spectral trace or spectrogram is a graph showing the time-varying flow velocity distribution derived from the measured Doppler frequencies [7]. This information is acquired from a

single sample volume in the field of view. The spectrogram is typically used to provide information about flow dynamics or blood velocity within a sample volume inside a blood vessel in coordination with the cardiac cycle. If multiple sample volumes are defined to fill out a field-of-view, and the locations of these sample volumes are mapped to a 2-D display using color-coded values in response to the amplitude or the frequency of the Doppler signal, blood flow images maybe produced [9]. Producing these types of 2-D images of blood flow is called real time Doppler color flow imaging.

1.4.3 Principles of Doppler Color Flow Imaging (CFI)

A Doppler color flow imaging system can be divided into two stages: Doppler signal acquisition and Doppler signal processing. A sample block diagram illustrating the components of the two stages of a Doppler color flow imaging system is shown in Figure 1-2.

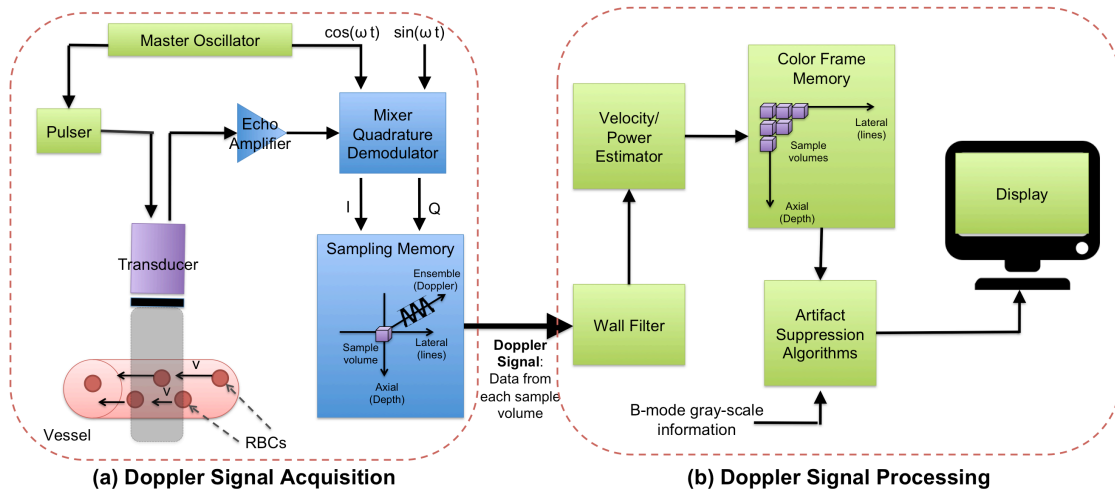


Figure 1-2: A sample block diagram of Doppler color flow imaging system constituting of 2 sections: (a) Doppler Signal acquisition section and (b) Doppler Signal Processing.

1.4.3.1 Doppler Signal Acquisition

A simplified layout of the Doppler signal acquisition stage is illustrated in Figure 1-2(a). Almost all modern CFI systems use array transducers, where the transducer consists of a large number of piezoelectric elements to transmit and receive ultrasound

pulses. The master oscillator and pulser blocks control the combination and sequence of signals to the individual transducer elements to generate a suitable transmitted beam formed of multiple scan lines within the region-of-interest (ROI). For each scan line, corresponding to the lateral position within the ROI, the received beam is then amplified to compensate for attenuation of echoes returning from deep portions of the field of view. The mixer (quadrature demodulator) block is responsible for extracting the directional Doppler shift signals from the returning echoes. This is achieved by demodulating the returning signal with the transmit signal from the master oscillator ($\cos(\omega t)$) and with a 90° phase shifted version ($\sin(\omega t)$) of the transmit signal. The demodulated signals are then sampled at time points that correspond to the different depths (axial position) of the sample volumes within the ROI whereas the lateral position of the sample volume is determined by its corresponding scan line within the ROI. For each sample volume, the ensemble of pulse echo samples referred to as the Doppler signal is determined for further processing. In the next sections, we discuss in detail some of the Doppler signal acquisition building blocks that directly contribute to the resulting images.

Pulser Block: Velocity Resolution and Aliasing Limit

The pulser block controls the number, N , and rate of pulses (*i.e.*, pulse repetition frequency (PRF)) transmitted through each scan line. Within an individual sampling region, each pulse reflected from moving red blood cells represents a sample in the signal to be used to calculate the Doppler shift (referred to as ensemble in Figure 1-2). Therefore, the greater the number of pulses N , the more samples in the signal; leading to a more accurate estimate of the Doppler shift. The number of transmitted pulses N for each scan line is limited by the depth of the region of interest, the required number of scan lines to be acquired and the necessary frame rate to maintain the images to be updated in real time [10]. The minimum detectable velocity (*i.e.*, velocity resolution), controlled by the pulser block, is inversely proportional to the period of the Doppler signal, which equals to the product of the number of pulses N and the interval between pulses ($1/\text{PRF}$). Therefore, decreasing PRF or increasing the number of pulses N can improve the velocity resolution (*i.e.*, decrease v_{min}). Another performance measure determined by the pulser block is the maximum detectable velocity. As defined by the

Nyquist sampling theory, the rate of pulsing (the pulse repetition frequency (PRF)) must be greater than twice the maximum frequency shift to be detected (*i.e.*, the Doppler shift corresponding to the maximum velocity of imaged blood flow) to avoid aliasing [10]. Aliasing is an inaccurate display of color that occurs in an image when the detected velocity in the corresponding sample volume exceeds the maximum detectable velocity [11]. Thus, the PRF setting on an ultrasound instrument affects the velocity resolution and sets the limit to the maximum accurately detectable blood velocity.

Sampling Memory Block: Axial Resolution and Sampling

In order to produce images with accurate estimates of the location of the source of a Doppler shift, a method known as range-gating is used. Range-gating is identifying a location along a scan line, the placement of which and the size determine the time instances for sampling of the received beams along that line to construct the Doppler signal for the location [12]. In color flow imaging (CFI) systems, this process is repeated for multiple gates to divide the ROI into sample volumes corresponding to samples of the received beams at different depths for the different scan lines within the ROI. Typically, the size of the gates is determined by the length of the transmitted pulse and defines the axial resolution in an ROI of CFI frame [12]. The Gate setting on an ultrasound instrument defines the size of the gates and thus the axial resolution of a CFI image.

1.4.3.2 Doppler Signal Processing

A simplified layout of the Doppler signal processing stage is illustrated in Figure 1-2(b). Data from each sample volume, identified as the Doppler signal, is filtered to reject clutter components and processed to form estimates of the power and velocity of the source of the Doppler signal. The average power of each clutter-filtered Doppler signal is computed as the mean-squared value of the signal, whereas the velocity estimate is determined by computing the mean Doppler frequency of the filtered signal and inserting it into the Doppler equation Eqn. 1-1 to calculate the corresponding velocity of scatterers within the sample volume. The results from each sample volume are stored in a color frame memory in which each sample volume is positioned in its locations within the region of interest using its lateral and axial coordinates to form an image. The color

frame image is then combined with the B-mode gray-scale information from the sample volume in the artifact suppression block to determine the probability that flow is present and accordingly, determine whether the corresponding pixel will be displayed as a colored or gray-scale pixel. Finally, depending on which display mode is used, the resulting Doppler color map is superimposed onto a B-mode image of the underlying structure. In the next sections, we discuss some of the Doppler signal processing building blocks in detail.

Wall / Clutter Filter Block

The Doppler signal acquired from a sample volume may constitute a range of frequencies (frequency spectrum) corresponding to the potentially different velocities of the moving targets within the sample volume [9]. Since any blood vessel is generally surrounded by other scattering sources like tissues and vessel walls, the Doppler signal may also contain undesired components corresponding to such non-blood scatterers. A “hypothetical” Doppler signal spectrum obtained from a sample volume including flowing blood is shown in Figure 1-3 [13]. The distribution centered at 0 Hz, “clutter”, corresponds to the signal coming back from slow-moving tissue, vessel wall motion or external mechanical vibrations. These sources of motion are characterized by being strong but significantly slower than blood flow resulting in the clutter signal having a high amplitude and a low frequency as shown in Figure 1-3. The range of frequencies (velocities) of red blood cells in the sample volume is represented by the “blood” distribution. A high-pass filter, called the wall or clutter filter, is typically applied to the Doppler signal to eliminate the clutter spectrum. The cut-off frequency of that filter defines the line within the Doppler signal spectrum that differentiates the clutter signal to be eliminated from the blood signal as shown in Figure 1-3(a). In the case of the blood and clutter distributions overlapping, the selection of the wall filter cut-off frequency becomes more challenging as illustrated in Figure 1-3(b). Selecting a low cut-off frequency would allow the detection of slow blood flow but would falsely include clutter signal, whereas selecting a high cut-off frequency would achieve sufficient clutter removal but would cause the loss of the signal from slow-moving blood. In a typical

Doppler imaging instrument, the selection of the filter's cut-off frequency is accomplished by the operator using the wall/clutter filter setting.

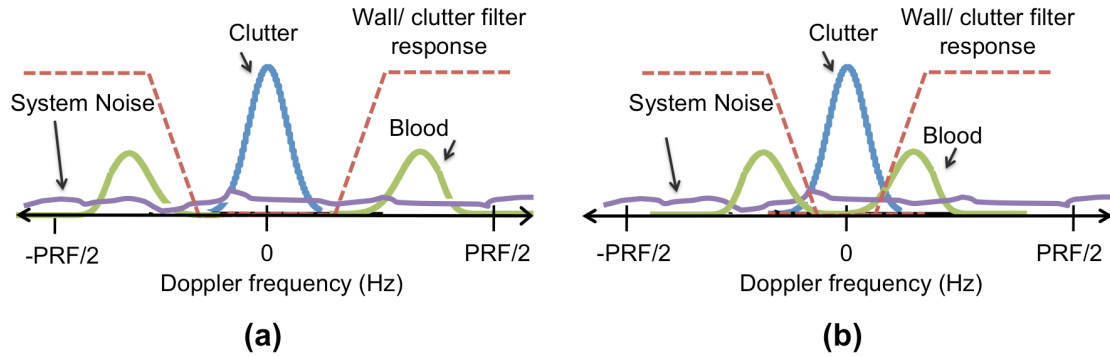


Figure 1-3: Illustration of hypothetical Doppler signal frequency spectrum. A high-pass filter, the wall/clutter filter, is used to suppress the high-energy, low-frequency clutter in the Doppler signal. Determining the filter cut-off can be (a) simple or (b) challenging if the clutter and blood spectra overlap.

Artifact Suppression Algorithms Block

With its stochastic nature, Doppler signal parameters may vary in a random fashion and therefore require some post-processing techniques such as spatial and temporal averaging and thresholding to reduce sharp fluctuations and signal dropouts in the final displayed image. The following are some of these techniques:

Noise Threshold

The purpose of the noise threshold is to eliminate the signal coming back from the noise spectrum (shown in Figure 1-3). If the estimate of average Doppler signal power is less than a minimum threshold level, the color pixel is not displayed. The exact value of the noise threshold is not controlled by the user but is a function of the gain setting [9].

Priority Setting

Despite applying clutter filtering and noise thresholding to Doppler signals within an ROI, some artifactual signals may still be displayed as blood [9]. For example, signals from highly echogenic solid structures that are characterized by very large amplitude

gray-scale echoes may be displayed as colored pixels and misinterpreted as blood in a color flow image. To suppress such signals from the image, the priority threshold, controlled by the priority instrument setting determines the maximum level of gray-scale intensity that would be displayed as color. If a pixel gray-scale value exceeds the priority level, it is likely to have come from a region containing solid tissue and therefore would not be assigned color.

1.4.3.3 Display Modes

The Doppler shift signals computed from the different sample volumes within a region of interest are used to produce two- or three-dimensional images of blood flow. There are two commonly used modes of display of color flow images:

Color Doppler Mode

A color Doppler image is a map of the mean Doppler frequency (corresponding to the mean flow velocity) computed from the phase shift or the delays between the echoes returning from the sample volume during subsequent pulses [12]. The mean frequency is computed for multiple sample volumes throughout the ROI and a color is assigned to each pixel depending on the speed and direction of flow. Blood flowing towards the transducer is typically mapped in blue color whereas blood flowing away from the transducer is assigned a red color. The pixel intensity displayed as the shade within the color scale represents the speed of the flow. An example of this type of display is illustrated in Figure 1-4(a).

One of the shortcomings of color Doppler imaging is its susceptibility to aliasing artifacts. The inaccurate display of color due to aliasing occurs when the detected velocity in the sample volume exceeds the maximum detectable velocity defined by the PRF setting [11]. If a higher PRF is used to avoid aliasing, the system becomes less sensitive to slow flow. Another major limiting factor for color Doppler is the inherent tendency for noise to overwhelm its signal if the gain is too high or the threshold is too low [14]. With its wide frequency range and random phase shift (as represented by the “noise” distribution in Figure 1-3), noise can appear as flow of any speed and direction. If these signals were of an amplitude above the noise threshold used in the system, they

would obscure the vascular signals coming from slow flow [15]. Color Doppler images are also angle dependant, by which in the worst case, flow perpendicular to the ultrasound beam would not be detected or displayed as there will be equal flow towards and away from the transducer resulting in zero mean velocity.

Power Doppler (PD) Mode

The power Doppler mode is an alternative mode to color Doppler mode that produces two- or three-dimensional color maps of the total power of the Doppler signal within each sample volume instead of the mean Doppler frequency [16]. An example of a power Doppler image is shown in Figure 1-4(b). The estimate of the Doppler signal power is computed using the area under the signal's power spectrum and is related to the red blood cell density in the sample volume. Power Doppler mode has several advantages over color Doppler. First, power Doppler signal is independent of flow velocity and direction, since the area under the spectrum is not affected by the wrapping of signal frequencies when Nyquist sampling is not met (*i.e.*, flow faster than twice the PRF is imaged) and thus is not subject to aliasing. In addition, power Doppler has an improved sensitivity to slow flow and a higher tolerance to noise since the power of signal from slow flow, when integrated with respect to frequency, is relatively higher than the noise power and, therefore, its signal can be maintained after applying the noise threshold. Since velocity information is not of interest in this mode, power Doppler is nearly angle independent, allowing it to detect and display even blood flowing perpendicular to the ultrasound beam. When comparing the color and power Doppler images of a kidney (Figure 1-4), it is clear that the power Doppler mode is able to depict the full cortical perfusion network, while color Doppler displays the large vessels only.

1.5 Power Doppler Imaging Applications

With these advantages of power Doppler ultrasound, it has rapidly earned its position as a tool to evaluate and quantify vascularity and perfusion in a wide variety of applications. These applications can be broadly divided into vascular depiction applications that depend on the improved sensitivity of power Doppler and vascular quantification

applications that use these depicted vascular networks to quantify blood flow in the area of interest.

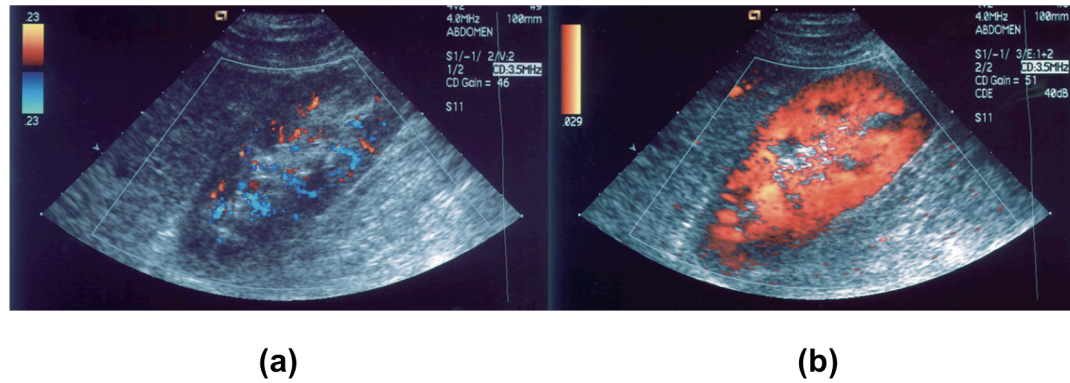


Figure 1-4: Sample Doppler color flow images of human right kidney using (a) color Doppler display mode showing only large vessels and (b) power Doppler mode with higher sensitivity showing the full cortical perfusion network [Downloaded from *Power Doppler Sonography, GE Healthcare, Medical Diagnostics: Medcyclopaedia.com* according to the term of use attached in Appendix A].

1.5.1 Vascular Depiction Applications

1.5.1.1 Vessel Morphology Depiction Applications

Firstly, power Doppler (PD) has been used in depiction of vessel morphology depending on its improved ability to display continuous vessel segments and better define edges of vascular structures [17]. The ability to display continuous flow has been particularly useful when studying a number of organs and systems, including: evaluating the anatomy of orbital arteries [18], differentiating normal and abnormal fetal anatomical structures [19], studying vascularity of intestinal structures related to Crohn's disease [20], and in screening thyroid nodules at high risk of malignancy [21]. Another application that has benefited from the improved ability of PD to depict small flow vessels that are possibly running in unfavorable angles to the Doppler beams is transcranial imaging. PD was used to detect and analyze intracranial aneurisms [22-24], imaging small-caliber, low-flow vessels [25, 26] and evaluating morphological and hemodynamic information in patients with severe head injury [27]. In large arteries,

power Doppler's improved definition of vessel edges enhance the accuracy of luminal and vessel diameters measurements used in diagnosing high-grade stenosis in the renal artery [28] and the carotid artery [29-33].

1.5.1.2 Inflammation Evaluation Applications

The second application is using power Doppler to image and evaluate inflammation specifically in the musculoskeletal tissues [34, 35]. Due to its enhanced sensitivity, PD is valuable in depicting increased flow in vessels that are dilated owing to inflammatory response such as the intra-articular knee vasculature in rheumatoid arthritis patients [36-39]. In addition, PD can be used to distinguish inflammatory and infectious musculoskeletal fluid collections from those that are noninflammatory and may help guide the decision to perform diagnostic biopsy procedure [40].

1.5.1.3 Tumor Vasculature Depiction Applications

The combined effect of power Doppler's sensitivity to slow flow and improved delineation of tortuous and irregular vessels makes it a promising technique to image intratumoral vessels [17]. Studies assessing vasculature of hepatocarcinoma [41, 42] and analyzing the lymph node involvement and vascular invasion with breast cancer [43] have found power Doppler to be a very effective tool. Moreover, other investigators used power Doppler to differentiate benign and malignant tumors in breast [44, 45], ovarian [46] and adnexal lesions [47].

1.5.2 Vascular Quantification Applications

Three-dimensional power Doppler became available for medical purposes towards the end of the last century [48, 49], giving rise to the possibility of extracting quantifiable objective measures describing full vasculature networks or trees in a volume of interest (VOI). A number of 3-D power Doppler quantification metrics were developed [13, 50, 51] based on the direct correlation of the power Doppler signal and the number or concentration of moving particles and their relation to fractional blood volumes and perfusion in the VOI. In 1999, while studying blood flow in adnexal masses; Pairleitner

et al. presented a standardized set of metrics that could give a mathematical expression of vascularization and flow [52]:

$$\text{Vascularization index} = \frac{\text{color voxels}}{\text{total voxels in VOI}}, \quad \text{Eqn. 1-2a}$$

$$\text{Flow index} = \frac{\text{sum of power in colored voxels}}{\text{color voxels}}, \quad \text{Eqn. 1-2b}$$

$$\text{Vascularization flow index} = \frac{\text{sum of power in colored voxels}}{\text{total voxels in VOI}} \quad \text{Eqn. 1-2c}$$

As defined in [52], VI, also known as color pixel density (CPD), measures the proportion of color voxels in the cube, representing the amount of moving blood in the tissue, FI, the mean power signal of blood flow, represents the intensity of flow at the time of acquisition and VFI is a combination of vascularization and flow indices representing both blood flow and vascularization. The software developed by Pairleitner et al. was later implemented in GE ultrasound scanners under the name VOCAL™: volumetric calculations.

The use of these quantification indices and VOCAL™ software, currently known as 3-D power Doppler angiography (3-D PDA), has produced an abundance of research communications in a variety of applications.

Quantifying tumor vascularity is the primary application for 3-D power Doppler angiography, especially as it offers unique ways for assessing women with gynecological cancers [53] such as ovarian [54, 55] and endometrial cancers [56, 57] and for diagnosis of malignant pelvic solid tumors [58]. Moreover, 3-D PDA was shown to serve as a useful tool in distinguishing benign and malignant breast [59, 60] and prostatic tumors [61].

These quantification indices are progressively being applied to studying the fetoplacental unit. Attempts to correlate the VI, FI and VFI indices to regional perfusion in fetal brain [62, 63], liver [64] and lungs [65, 66] have been reported. The most promising field in applying 3-D PDA is the analysis of placental vascularity in different stages of normal pregnancy [67-71] as well as adverse pregnancy outcomes [72-75]. These indices

have also shown promising results when assessing the endometrium for assisted reproductive techniques and *in vitro* fertilization treatments [47, 76, 77].

1.6 Challenges in Power Doppler Imaging

Despite this abundance of literature on the applications of power Doppler imaging, there exist a number of challenges and limitations that are consistently being highlighted in these studies.

1.6.1 Operator-Dependant Instrument Settings

The first and most commonly reported challenge is the sensitivity of the acquired power Doppler signal to numerous operator-dependent instrument settings. An example of a commercial ultrasound scanner user panel shown in Figure 1-5 illustrates that 16 different instrument settings need to be setup prior to image acquisition in power Doppler mode, each of which has an effect on the amount of blood depicted in images. Some studies and opinion letters were published analyzing and discussing further the impact of these settings on power Doppler signal. In a letter to the *Radiology* editor, Cardinals et al. stated that machine settings such as PRF, filters, ensemble length, and transmit power can all contribute to false appearance of color from stationary structures in power mode [78]. Many studies were conducted to understand and evaluate how these settings influence flow information displayed by the power Doppler mode [79-84]. An increase in PRF and wall filter cut-off decreases flow areas significantly, whereas decreasing frame rate increases the flow area [79]. In accordance with these results, Gudmundsson et al. also reported that many instrument settings can influence power Doppler signal intensity and emphasized the need for optimum fixed presets of settings when attempting to measure flow from power Doppler images [80].

1.6.1.1 The wall filter cut-off setting

Due to its larger source of variability and effect on the amount of blood depicted in images, the wall-filter cut-off setting was one of the prevalent settings that received a lot of interest from researchers. Deverson et al. studied factors affecting the relationship between power signal and imaged vessel sizes and found the high-pass clutter filter to be

a source of a non-linearity between the two parameters [81]. Similarly, it was shown that the signal intensity of power Doppler images of flow is clearly affected by the clutter filter [82]. Browne et al. emphasized the importance of understanding the effect of instrument settings such as wall filter cut-off on the Doppler signal when interpreting the clinical significance of the Doppler information, particularly when evaluating serial examinations for changes in blood flow characteristics [84]. In a more recent study by Garcia et al., it was shown that the wall filter can induce severe power Doppler signal losses that could negatively influence assessment of vascular stenosis [85]. They recommended that clinicians should consider these signal losses when interpreting power Doppler images.

1.6.1.2 Operator-dependant settings and 3-D PDA

More specific studies and editorial notes on the effects of instrument settings on the quantification of the power Doppler signal using the three indices (VI, FI, and VFI) are also found in literature [86-90]. Due to the arbitrary nature of these indices and their dependence on the color pixel count, any factor that alter this count could affect the vascularity assessment. Instrument settings (gain, wall filter cut-off, pulse repetition frequency (PRF), and frame rate) play a major role in these alterations [86]. Therefore, the need for care with adjustments in instrument settings is important and, accordingly, more studies evaluating how these settings affect the quantification indices are required [87]. A study by Raine-Fenning et al. concluded that all three indices are affected significantly by variations in power Doppler instrument settings and recommended maintaining the settings in order to obtain meaningful comparisons within and between subjects [88]. It was also found that the degree of overestimation of moving blood volume in small tubes (vessels) depends on instrument settings and should be taken into account when quantifying small vessels in a clinical setting [90]. With the fast growing body of literature using 3-D PDA, W. P. Martins points out, in a note published in *Ultrasound in Obstetrics and Gynecology*, the necessity to formulate a proposal for standardized instrument settings to be used worldwide [91]. These standards would have to be developed in collaboration with the manufacturers and incorporated into machines to be available to the operators. Only then will researchers be able to establish normal

PDA indices reference values for different applications and test if pathologic conditions are related to abnormal 3-D PDA indices.

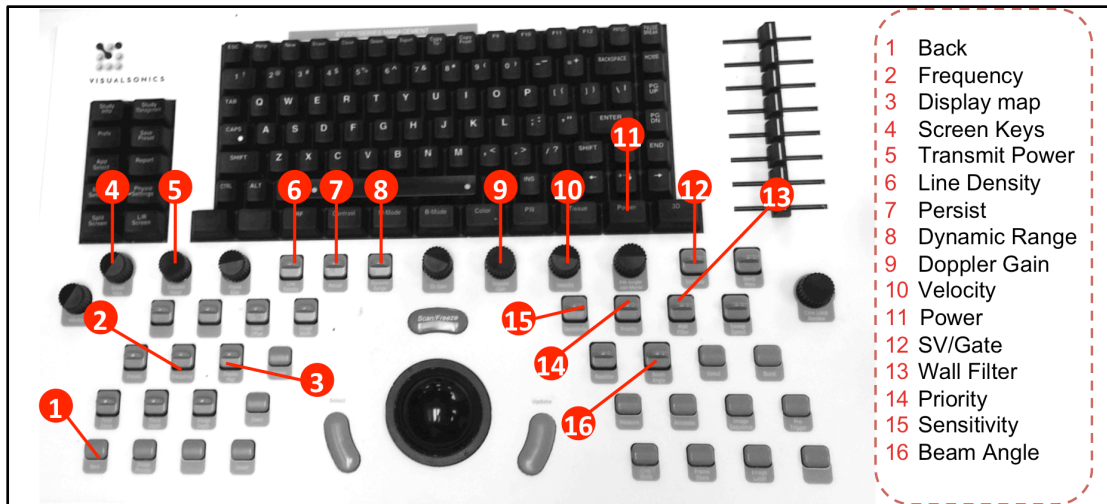


Figure 1-5: An example of a commercial power Doppler system (Vevo2100, VisualSonics, Toronto, Canada) user panel having 16 user-dependent settings to be set prior to image acquisition.

1.6.2 Image Artifacts

The other major challenge for power Doppler vascular imaging is the presence of Doppler artifacts, which cause the misassignment of color to signal from sources other than blood flow [92]. A variety of Doppler artifacts have been documented in literature; however, we will be focusing on artifacts that specifically affect vascular imaging applications of power Doppler. These artifacts are: blooming, perivascular, flash, pseudoflow and jail-bar artifacts.

1.6.2.1 Blooming and Perivascular Artifacts

Blooming is commonly known as “color bleed” because the color spreads out from within the vessel and bleeds beyond the wall into adjacent areas [11]. An example of an image with blooming artifact is shown in Figure 1-6. Theoretically, it occurs due to multiple reflections or reverberations from the vessel wall, which are misinterpreted as reflections occurring further along the beam axis, making blood flow within the vessel to

appear outside the vessel [93]. In practice, the blooming artifact is directly related to the combined effect of the gain and color rejection (*i.e.* wall filter cut-off and priority) settings due to the tradeoff between having enough gain to visualize flow in small vessels and having so much gain that it causes an exaggerated depiction of larger vessels [93, 94]. Excessive gain may also cause the overlap of signals from adjacent vessels, resulting in their appearance as a single vessel [94].

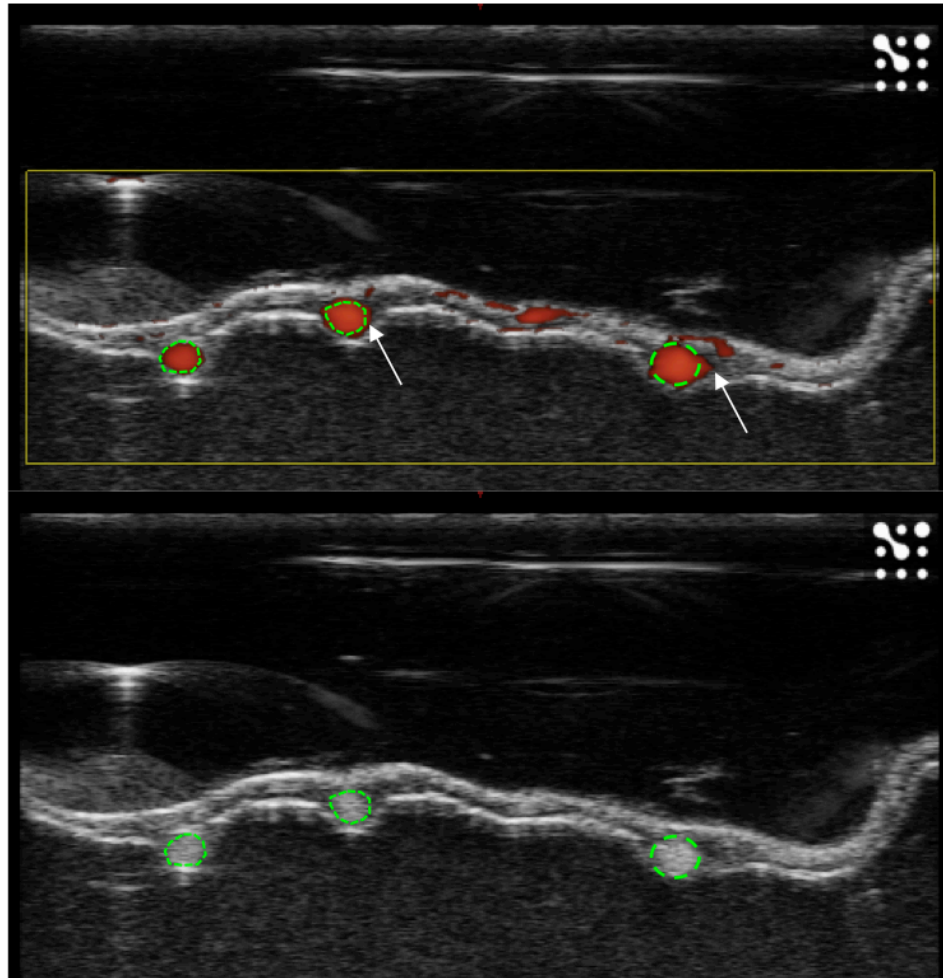


Figure 1-6: Blooming artifact in a power Doppler image. Color “bleeds” (marked by white arrows) outside vessel boundaries (dashed green line) produced by manually segmenting vessels from B-mode image (lower image).

The perivascular artifact is essentially a blooming artifact that occurs in cases of turbulent flow, which causes tissue vibrations that result in a single hue of power around vessels and is a marker of stenotic vessel segments [95].

Blooming and perivascular artifacts have been reported to cause overestimation of vessel diameters using power Doppler [31, 96-99].

1.6.2.2 Flash and Pseudoflow Artifacts

Flash artifact is a sudden burst of random color that fills the ROI and is caused by tissue or transducer motion and is most commonly seen in hypo-echoic areas such as cysts or fluid collections [92]. Flash artifacts are related to the priority instrument setting, which suppresses color pixels if a strong gray-scale echo is detected. In the case of hypo-echoic areas, the absence of gray-scale echoes will cause color pixels to be displayed for nearly stationary regions [92]. Power Doppler is more susceptible to flash artifacts than other Doppler modes due to its increased sensitivity to motion [11].

Pseudoflow artifact is closely related to flash artifact in being dependant on motion, but it is specifically dependant on fluid (other than blood) motion [92]. The color or power Doppler signal will appear as long as the fluid motion continues, such as motion of fluid collection in the gastrointestinal or urinary systems.

The presence of flash and pseudoflow artifacts was reported to significantly hamper visualization and quantification of vasculature and necessitated the repetition of scans to ensure enough artifact-free images are acquired for further analysis [19, 100, 101]

1.6.2.3 Jail Bar / Vertical Lines Artifact

Jail bar artifact is a set of periodic colored vertical lines that are displayed across the full region of interest and is observed in power Doppler images [102]. An example of an image displaying jail bar artifact is shown in Figure 1-7. It is caused by an error in lateral interpolation while processing backscattered signals that approach the saturation level of the system. When the transducer is saturated by a very high-amplitude received signal, it appears to affect the efficiency of the pulse transmission of the following scan

line. Interpolation of the weaker than expected scan lines causes a lack of color, which appears as the striping effect. Martins et al. have reported observing artifactual vertical lines when imaging a flow-free water tank [91]. They associated these artifactual lines to strong reflections from the base of the tank (a nearly perfect reflector) and validated their assumption by placing a 2 cm layer of bovine muscle tissue at the bottom of the tank, causing the vertical lines to disappear. The artifact causes the loss of signal from some lines and an overlay of color on other lines, which significantly affect the quality of the image and is specifically problematic when imaging vasculature in a thin tissue layer placed on a strong reflector.

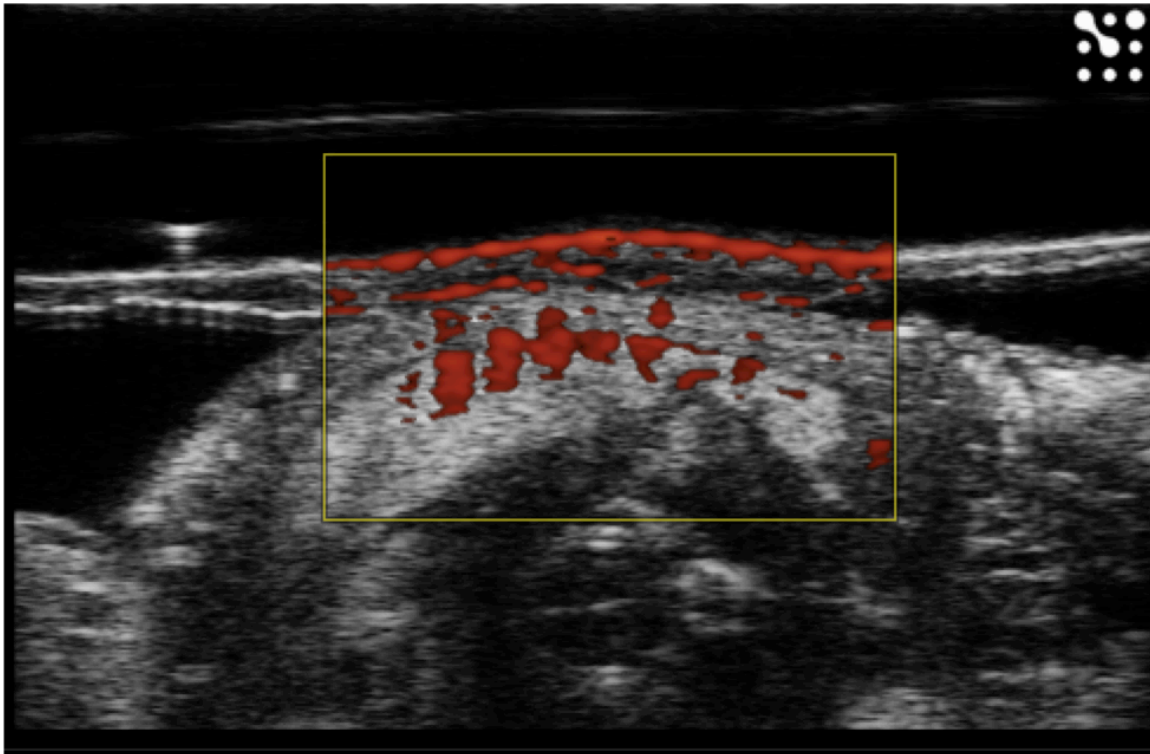


Figure 1-7: Jail bar artifact in a power Doppler image. Vertical bars of color separated with blank lines are seen overlaying different structures in the image.

1.6.2.4 Doppler Artifacts and 3-D PDA

With all the above-mentioned artifacts affecting the amount of displayed colored pixels in power Doppler images, it is expected that any subsequent quantification of such artifactual Doppler information would result in false values of the 3-D PDA indices. The

over- or underestimation of these indices would present a limitation to their use in clinical settings or even by researchers attempting to use 3-D PDA to study different subjects or study longitudinal variations within the same subject [91].

1.7 Attempts to Overcome Challenges

1.7.1 Optimizing Instrument Settings using Flow Phantoms

In an attempt to overcome some of the challenges of having operator-dependent instrument settings, some investigators performed *in vitro* studies using microvessel flow phantoms to better understand the effect of the different settings on images [91, 99, 103-105]. Understanding the individual and combined effects of these settings on the acquired images provided these investigators with the opportunity to calibrate these settings for specific applications or formulate guidelines on how to set them up to acquire good quality images. For example Kruse et al. presented an optimized set of instrument settings and tested its reliability to locate and measure blood flow in nail bed of human finger [103]. Camfferman et al. was able to calibrate the instrument settings to improve imaging of preterm brain vessels [99], whereas Sakano et al. presented a means to optimize the PRF setting to calibrate different types of ultrasound machines and enable direct comparison of finger joint images between ultrasound machine models [105]. In a similar study comparing different machines, Ten Cate et al. reported the different sets of machine settings needed to detect the lowest flow velocity in a microvessel flow phantom [104].

1.7.2 Developing Application-Based Instrument Settings Standard

Other investigators performed clinical studies to test and define a set of optimum settings for a specific application. Collins et al. investigated the feasibility of using the sub-noise gain level (a subject-based gain level determined by increasing the gain to the level at which obvious noise artifacts are present then slowly lowering it to a level just below this threshold) to quantify placenta vascularity using 3-D PDA indices [100]. This study showed that the sub-noise gain setting could be used to represent a patient-specific optimum gain level. Employing their expertise in using and analyzing Doppler flow imaging, some physicians and radiologists were able to formulate guidelines for

instrument setting optimization for specific applications, such as diagnosis of liver lesions [106]. Similarly, Kruskal et al. presented a comprehensive guide to setting up Doppler flow instrument settings for a number of different applications in hepatic sonography [83]. A comparable guide for optimizing machine settings and avoiding artifacts in rheumatological Doppler imaging applications was presented by Torp-Pedersen et al. [107].

1.7.3 Optimizing Wall / Clutter Filter Processing

While all the above mentioned studies did not attempt to improve or change how the Doppler imaging system performed, other investigators worked on improving the signal processing methods in Doppler imaging systems to overcome its limitations. As highlighted previously, the wall filter cut-off setting has been reported frequently to affect the quality and accuracy of blood flow display and quantification in Doppler flow images; therefore, many investigators have worked on developing more optimized filter designs or more advanced filtering approaches. Some investigators explored and analyzed different classes of filters (finite impulse response (FIR), infinite impulse response (IIR), and regression filters) [108] or different IIR filter initialization techniques to improve clutter filter performance [109]. Thomas and Hall proposed a “DC removal technique” that involves shifting the undesired clutter signals to zero frequency then removing these signals by subtracting their average from each of them. This technique results in a narrow band high pass filter without reducing the number of samples available for velocity estimation [110]. Further advancement of the wall filter involved the use of adaptive clutter filtering techniques [111-116]. In adaptive clutter filtering techniques, an optimum filter is dynamically selected at individual or multiple sample volumes by adapting its stopband or filter coefficients to the local clutter spectral characteristics.

1.7.3.1 The Original WFSC Method

A different approach of clutter filter tuning was proposed in our lab in 2009 [117]. Based on the idea of power Doppler flow detection performance assessment presented by Zemp and Insana [118], receiver operator characteristic (ROC) curves for the quality of

clutter filtering were constructed from flow-phantom experiments using several single - vessel flow phantoms of 160, 200, 250, 300 and 360 μm diameters, with blood-mimicking fluid with flow velocity (4, 3, 2, 1 and 0.5 mm/s) imaged with different transducer frequencies (30 and 40 MHz). For the cases demonstrating high performance, the relationship between the amount of colored pixels in the ROI, represented by the color pixel density (CPD), and the wall filter cut-off frequency was represented by the *wall filter selection curve* (WFSC) [119]. A consistently identified characteristic plateau was recognized at intermediate cut-off frequencies along this curve, which was hypothesized to enclose the optimum cut-off frequency for that specific image. A mathematical model based on ROC statistics was developed to study the behavior of the wall filter selection curve for ROIs enclosing multiple vessels and were compared to experimental data acquired with a 30-MHz transducer and a custom-designed multiple-vessel flow phantom with vessel sizes (200–300 μm), blood flow velocities (1–10 mm/s), and different blood vessel orientations [120]. Monte Carlo simulations using the mathematical model helped analyze properties of the WFSC that yield accurate estimates of the optimum cut-off frequency for a specific image. These simulations showed that WFSCs for multiple-vessel regions include a plateau whose CPD corresponds to the total vascular volume fraction when the plateau is $> 0.5\text{mm/s}$ in length and begins at a wall filter cutoff $< 2\text{mm/s}$. The WFSC method is proposed to automate the selection of the wall filter cut-off frequency setting without the need for any input from the user. Further development and evaluation of the WFSC method is presented later in this thesis.

To our knowledge, there are no other similar methods to the WFSC method presented in the scientific literature; however, there are some automated wall filter cut-off setting techniques proposed in the patent literature. A summarized review of the methods published in the patent literature can be found in Chapter 2 of this thesis.

1.7.4 Image Post-Processing Methods to Reduce Artifacts

In cases when presence of Doppler artifacts was inevitable and only images with artifacts could be acquired and to be used to study or quantify vasculature, researchers have proposed some image processing algorithms to enhance power Doppler images prior to further processing. Hashimoto et al. developed a set of post-processing methods

including surface rendering, filtration, rotation and magnification to produce 3-D images suitable for a new 3-D view that allows the endoscopic view of flow such as arterial branches and curved vessels to be visualized [121]. Other investigators implemented 3-D vessel reconstruction algorithms to enhance the signal from small vessels and improve the continuity of big vessels, which may not be entirely perceived due to the signal loss from regions of low backscattered pressure within a vessel [122]. Another post-processing algorithm proposed by Lai et al. involved applying thresholding, morphological transformations such as dilations and erosions and 3-D skeletonization and reconstruction of vascular networks to help extract diagnostic features from breast cancer vasculature [45]. Further information and development of this method is provided later in Chapter 4 of this thesis. Echoscintigraphy is a novel image-processing algorithm developed by Schlosser et al. in 2003 that provided reduction of color blooming in power Doppler images [123]. It improves the detection of low-intensity color signals by applying special summation algorithms to multiple frames and resulted in more accurate vessel diameter estimations.

1.8 Hypothesis and Objectives

We hypothesize that a more efficient power Doppler signal processing method that involves the automation of the wall filter cut-off instrument setting and post-processing 3-D power Doppler images to reduce artifacts will improve the accuracy and robustness of vascular depiction and quantification using power Doppler imaging.

Driven by the research hypothesis, the overall goal of this thesis study is to develop, evaluate and validate a new power Doppler data processor that uses an improved version of the wall filter selection curve method and 3-D vascular network reconstruction algorithms to produce more accurate representations of imaged vascular networks for depiction and quantification purposes.

To achieve our overall research goal, this thesis study has been broken down into the following four specific objectives:

- 1) Design an improved, more fully automated version of the original WFSC method using image data from a multiple-vessel flow phantom such that the resulting image is the most accurate, artifact-reduced representation of the actual imaged vessels.
- 2) Strengthen the theoretical foundation of the WFSC method by redesigning the mathematical model of the CPD-wall filter cut-off relationship and use it to guide the design of an online implementation of the method.
- 3) Develop and evaluate, by comparison with contrast-enhanced ultrasound imaging, the effect of applying a two-stage power Doppler data processor (including the improved WFSC method and 3-D vascular network reconstruction method) for a power Doppler angiography (vascular quantification) application (Section 1.5.2) using a longitudinal study of a murine breast cancer xenograft model.
- 4) Evaluate, by comparison with *in vivo* optical imaging, the effect of applying the two-stage power Doppler data processor for a power Doppler vascular depiction application (Section 1.5.1) using the vascular networks of the chorioallantoic membrane (CAM) of chicken embryos.

1.9 Thesis Outline

This thesis presents and evaluates new signal processing methods for power Doppler microvascular depiction and quantification applications. Each of the four specific objectives is addressed in one of the chapters summarized below. Chapters 2 through 5 represent work that is either published or in preparation for submission to a peer-reviewed journal and Chapter 6 includes concluding remarks and some future directions.

Chapter 2 presents an improved implementation of the wall filter selection curve (WFSC) method that automatically detects characteristic intervals in a selection curve. A multiple-step decision algorithm that selects an operating point along the automatically detected characteristic intervals is presented. When applied to a power Doppler image,

the method divides a region of interest (ROI) into subregions to adapt the operating point cut-off velocity to local variations in vascularity. The method is validated by comparing the method's vascular quantification metric color pixel density (CPD), to known vascular volume fraction estimate of a multiple-vessel flow phantom. The results are a promising indication of the potential to fully automate the wall-filter cut-off velocity setting in a power Doppler system using the WFSC method.

Chapter 3 presents a new three-component mathematical model developed to guide the design of an online implementation of the improved WFSC method (Chapter 2) for in vivo imaging. The model treats Doppler imaging as a signal detection task in which the scanner must distinguish pixels inside, adjacent to and outside a vessel. The model includes a cost function developed to identify the optimum cut-off velocity that provides accurate vascular quantification and minimizes the effect of color pixel artifacts on visualization of vascular structures. Monte Carlo simulations using the new model were used to define WFSC curve characteristics (number of samples, upper bound on CPD variability and criteria for optimum cut-off selection) to ensure robust performance of the method and reliable vascular quantification accuracy. The model provides an intuitive, empirical description of the relationship between system settings and blood-flow detection performance in power Doppler imaging.

Chapter 4 combines the improved WFSC method (Chapter 2) after adapting to three-dimensional (3-D) power Doppler images with a 3-D vascular network reconstruction method into a new two-stage Doppler processing method. The two-stage method is evaluated for improving 3-D power Doppler visualization and quantification using a murine breast cancer tumor model. The variations of WFSC-selected cut-off frequencies within a 3-D image and across time points in a longitudinal study are analyzed using histograms. Power Doppler angiography (PDA) indices, visualization index (VI), visualization flow index (VFI) and flow index (FI), were computed to evaluate the effect of individually applying or combining one or both stages of the method when quantifying the tumor vasculature. Contrast enhanced ultrasound (CEUS) images were acquired as a reference for vascular quantification. Results show that the proposed two-stage process presents increased accuracy and robustness to qualitative and

quantitative outcomes of studies using 3-D power Doppler angiography to assess complex, dense vascular networks.

Chapter 5 evaluates the effect of processing power Doppler images of the simple vascular network in a chick embryo chorioallantoic membrane (CAM) using the two-stage process developed in Chapter 4 as a vascular depiction application of 3-D power Doppler imaging. The processed images are compared to exported raw images from a commercial scanner using the optical images of the CAMs as a reference. The comparison between the Doppler processing methods (two-stage and commercial scanner software) is based on improvement in vessel detection, visualization, artifact reduction and accurate depiction of vessels for diameter measurement. Results indicate that the proposed Doppler processing method can potentially improve the usability of 3-D power Doppler imaging in vascular depiction applications such as assessment of vessel stenosis or studying vascular morphology to help in diagnosing pathology.

References

- [1] G. A. W. Gooding, "The Age of Vascular Imaging," *Emergency Radiology*, vol. 6, pp. 2-2, 1999.
- [2] N. E. Green, S. Y. Chen, J. C. Messenger, *et al.*, "Three-Dimensional Vascular Angiography," *Curr Probl Cardiol*, vol. 29, pp. 104-142, 2004.
- [3] A. L. Herrick and C. Hutchinson, "Vascular Imaging," *Best Practice & Research Clinical Rheumatology*, vol. 18, pp. 957-979.
- [4] A. W. Reid, D. B. Reid, and G. H. Roditi, "Vascular Imaging: An Unparalleled Decade," *J Endovasc Ther*, vol. 11 Suppl 2, pp. II163-179, 2004.
- [5] S. Delorme and M. V. Knopp, "Non-Invasive Vascular Imaging: Assessing Tumour Vascularity," *Eur Radiol*, vol. 8, pp. 517-527, 1998.
- [6] J. C. Miller, H. H. Pien, D. Sahani, *et al.*, "Imaging Angiogenesis: Applications and Potential for Drug Development," *J Natl Cancer Inst*, vol. 97, pp. 172-187, 2005.
- [7] W. R. Hendee and E. R. Ritenour, *Medical Imaging Physics*, Fourth edition. ed. New York: Wiley-Liss., 2002.
- [8] F. Kiessling, S. Fokong, J. Bzyl, *et al.*, "Recent Advances in Molecular, Multimodal and Theranostic Ultrasound Imaging," *Adv Drug Deliv Rev*, vol. 72, pp. 15-27, 2014.
- [9] D. H. Evans and W. N. McDicken, *Doppler Ultrasound : Physics, Instrumentation and Signal Processing*, 2nd ed. Chichester ; New York: Wiley, 2000.
- [10] R. S. C. Cobbold, *Foundations of Biomedical Ultrasound*. Oxford ; New York: Oxford University Press, 2007.
- [11] D. J. Rubens, S. Bhatt, S. Nedelka, *et al.*, "Doppler Artifacts and Pitfalls," *Radiol Clin North Am*, vol. 44, pp. 805-835, 2006.
- [12] J. r. A. Jensen, *Estimation of Blood Velocities Using Ultrasound : A Signal Processing Approach*. Cambridge ; New York, NY, USA: Cambridge University Press, 1996.
- [13] J. M. Rubin, "Power Doppler," *Emerg Radiol*, vol. 9, pp. S318-S322, 1999.

- [14] J. E. MacSweeney, D. O. Cosgrove, and J. Arenson, "Colour Doppler Energy (Power) Mode Ultrasound," *Clin Radiol*, vol. 51, pp. 387-390, 1996.
- [15] R. O. Bude, J. M. Rubin, and R. S. Adler, "Power Versus Conventional Color Doppler Sonography: Comparison in the Depiction of Normal Intrarenal Vasculature," *Radiology*, vol. 192, pp. 777-780, 1994.
- [16] J. M. Rubin, R. O. Bude, P. L. Carson, *et al.*, "Power Doppler Us - a Potentially Useful Alternative to Mean Frequency-Based Color Doppler Us," *Radiology*, vol. 190, pp. 853-856, 1994.
- [17] C. Martinoli, L. E. Derchi, G. Rizzatto, *et al.*, "Power Doppler Sonography: General Principles, Clinical Applications, and Future Prospects," *Eur Radiol*, vol. 8, pp. 1224-1235, 1998.
- [18] F. Giovagnorio and L. Quaranta, "Power Doppler Sonography Enhances Visualization of Orbital Vessels," *J Ultrasound Med*, vol. 14, pp. 837-842, 1995.
- [19] S. J. Fortunato, "The Use of Power Doppler and Color Power Angiography in Fetal Imaging," *Am J Obstet Gynecol*, vol. 174, pp. 1828-1831; discussion 1831-1823, 1996.
- [20] G. Maconi, G. M. Sampietro, A. Russo, *et al.*, "The Vascularity of Internal Fistulae in Crohn's Disease: An in Vivo Power Doppler Ultrasonography Assessment," *Gut*, vol. 50, pp. 496-500, 2002.
- [21] M. C. Chammas, R. Gerhard, I. R. de Oliveira, *et al.*, "Thyroid Nodules: Evaluation with Power Doppler and Duplex Doppler Ultrasound," *Otolaryngol Head Neck Surg*, vol. 132, pp. 874-882, 2005.
- [22] J. M. Wardlaw, J. C. Cannon, and R. J. Sellar, "Use of Color Power Transcranial Doppler Sonography to Monitor Aneurysmal Coiling," *AJNR Am J Neuroradiol*, vol. 17, pp. 864-867, 1996.
- [23] C. L. Turner and P. J. Kirkpatrick, "Detection of Intracranial Aneurysms with Unenhanced and Echo Contrast Enhanced Transcranial Power Doppler," *J Neurol Neurosurg Psychiatry*, vol. 68, pp. 489-495, 2000.
- [24] P. M. White, J. M. Wardlaw, E. Teasdale, *et al.*, "Power Transcranial Doppler Ultrasound in the Detection of Intracranial Aneurysms," *Stroke*, vol. 32, pp. 1291-1297, 2001.
- [25] A. R. Kenton, P. J. Martin, and D. H. Evans, "Power Doppler: An Advance over Colour Doppler for Transcranial Imaging?," *Ultrasound Med Biol*, vol. 22, pp. 313-317, 1996.

- [26] K. Kimura, M. Yasaka, M. Koga, *et al.*, "Successful Application of Three-Dimensional Transcranial Power Doppler Imaging in Two Stroke Patients," *Intern Med*, vol. 37, pp. 770-773, 1998.
- [27] T. Shiogai, K. Nagayama, G. Damrinjap, *et al.*, "Morphological and Hemodynamic Evaluations by Means of Transcranial Power Doppler Imaging in Patients with Severe Head Injury," *Acta Neurochir Suppl*, vol. 71, pp. 94-100, 1998.
- [28] A. Manganaro, G. Ando', A. Salvo, *et al.*, "A Comparison of Power Doppler with Conventional Sonographic Imaging for the Evaluation of Renal Artery Stenosis," *Cardiovasc Ultrasound*, vol. 2, p. 1, 2004.
- [29] B. Griewing, C. Morgenstern, F. Driesner, *et al.*, "Cerebrovascular Disease Assessed by Color-Flow and Power Doppler Ultrasonography. Comparison with Digital Subtraction Angiography in Internal Carotid Artery Stenosis," *Stroke*, vol. 27, pp. 95-100, 1996.
- [30] W. Steinke, S. Ries, N. Artemis, *et al.*, "Power Doppler Imaging of Carotid Artery Stenosis. Comparison with Color Doppler Flow Imaging and Angiography," *Stroke*, vol. 28, pp. 1981-1987, 1997.
- [31] O. E. Elgersma, M. S. van Leeuwen, R. Meijer, *et al.*, "Lumen Reduction Measurements of the Internal Carotid Artery before and after Levovist Enhancement: Reproducibility and Agreement with Angiography," *J Ultrasound Med*, vol. 18, pp. 191-201, 1999.
- [32] M. Müller, P. Ciccotti, W. Reiche, *et al.*, "Comparison of Color-Flow Doppler Scanning, Power Doppler Scanning, and Frequency Shift for Assessment of Carotid Artery Stenosis," *J Vasc Surg*, vol. 34, pp. 1090-1095, 2001.
- [33] S. O. Oktar, C. Yücel, D. Karaosmanoglu, *et al.*, "Blood-Flow Volume Quantification in Internal Carotid and Vertebral Arteries: Comparison of 3 Different Ultrasound Techniques with Phase-Contrast Mr Imaging," *AJNR Am J Neuroradiol*, vol. 27, pp. 363-369, 2006.
- [34] W. A. Schmidt, "Technology Insight: The Role of Color and Power Doppler Ultrasonography in Rheumatology," *Nat Clin Pract Rheumatol*, vol. 3, pp. 35-42; quiz 59, 2007.
- [35] R. J. Wakefield, A. K. Brown, P. J. O'Connor, *et al.*, "Power Doppler Sonography: Improving Disease Activity Assessment in Inflammatory Musculoskeletal Disease," *Arthritis Rheum*, vol. 48, pp. 285-288, 2003.
- [36] J. S. Newman, T. J. Laing, C. J. McCarthy, *et al.*, "Power Doppler Sonography of Synovitis: Assessment of Therapeutic Response--Preliminary Observations," *Radiology*, vol. 198, pp. 582-584, 1996.

- [37] M. Carotti, F. Salaffi, P. Manganelli, *et al.*, "Power Doppler Sonography in the Assessment of Synovial Tissue of the Knee Joint in Rheumatoid Arthritis: A Preliminary Experience," *Ann Rheum Dis*, vol. 61, pp. 877-882, 2002.
- [38] R. Kasukawa, K. Shio, Y. Kanno, *et al.*, "Power Doppler and Spectral Doppler Measurements of Knee-Joint Synovitis in Rheumatoid Arthritis Patients with Superficial Pattern Signals and in Those with Deep Pattern Signals," *Mod Rheumatol*, vol. 17, pp. 267-272, 2007.
- [39] E. M. Bouta, P. D. Banik, R. W. Wood, *et al.*, "Validation of Power Doppler Versus Contrast-Enhanced Magnetic Resonance Imaging Quantification of Joint Inflammation in Murine Inflammatory Arthritis," *J Bone Miner Res*, vol. 30, pp. 690-694, 2015.
- [40] W. H. Breidahl, J. S. Newman, M. S. Taljanovic, *et al.*, "Power Doppler Sonography in the Assessment of Musculoskeletal Fluid Collections," *AJR Am J Roentgenol*, vol. 166, pp. 1443-1446, 1996.
- [41] B. I. Choi, T. K. Kim, J. K. Han, *et al.*, "Power Versus Conventional Color Doppler Sonography: Comparison in the Depiction of Vasculature in Liver Tumors," *Radiology*, vol. 200, pp. 55-58, 1996.
- [42] R. Lencioni, F. Pinto, N. Armillotta, *et al.*, "Assessment of Tumor Vascularity in Hepatocellular Carcinoma: Comparison of Power Doppler Us and Color Doppler Us," *Radiology*, vol. 201, pp. 353-358, 1996.
- [43] T. S. Mehta and S. Raza, "Power Doppler Sonography of Breast Cancer: Does Vascularity Correlate with Node Status or Lymphatic Vascular Invasion?."
- [44] S. Raza and J. K. Baum, "Solid Breast Lesions: Evaluation with Power Doppler Us," *Radiology*, vol. 203, pp. 164-168, 1997.
- [45] Y. C. Lai, Y. S. Huang, D. W. Wang, *et al.*, "Computer-Aided Diagnosis for 3-D Power Doppler Breast Ultrasound," *Ultrasound Med Biol*, vol. 39, pp. 555-567, 2013.
- [46] A. Kurjak, S. Kupesic, T. Anic, *et al.*, "Three-Dimensional Ultrasound and Power Doppler Improve the Diagnosis of Ovarian Lesions," *Gynecol Oncol*, vol. 76, pp. 28-32, 2000.
- [47] S. Kupesic and A. Kurjak, "Contrast-Enhanced, Three-Dimensional Power Doppler Sonography for Differentiation of Adnexal Masses," *Obstet Gynecol*, vol. 96, pp. 452-458, 2000.
- [48] D. B. Downey and A. Fenster, "Vascular Imaging with a Three-Dimensional Power Doppler System," *AJR Am J Roentgenol*, vol. 165, pp. 665-668, 1995.

- [49] Z. Guo, L. G. Durand, L. Allard, *et al.*, "In Vitro Evaluation of Multiple Arterial Stenoses Using Three-Dimensional Power Doppler Angiography," *J Vasc Surg*, vol. 27, pp. 681-688, 1998.
- [50] P. L. Carson, L. Xu, J. Pallister, *et al.*, "Approximate Quantification of Detected Fractional Blood Volume and Perfusion from 3-D Color Flow and Doppler Power Signal Imaging," in *Ultrasonics Symposium, 1993. Proceedings., IEEE 1993*, pp. 1023-1026 vol.1022, 31 Oct-3 Nov 1993.
- [51] P. L. Carson, J. B. Fowlkes, M. A. Roubidoux, *et al.*, "3-D Color Doppler Image Quantification of Breast Masses," *Ultrasound Med Biol*, vol. 24, pp. 945-952, 1998.
- [52] H. Pairleitner, H. Steiner, G. Hasenoehrl, *et al.*, "Three-Dimensional Power Doppler Sonography: Imaging and Quantifying Blood Flow and Vascularization," *Ultrasound Obstet Gynecol*, vol. 14, pp. 139-143, 1999.
- [53] J. L. Alcázar and M. Jurado, "Three-Dimensional Ultrasound for Assessing Women with Gynecological Cancer: A Systematic Review," *Gynecol Oncol*, vol. 120, pp. 340-346, 2011.
- [54] J. L. Alcazar, L. T. Merce, and M. Garcia Manero, "Three-Dimensional Power Doppler Vascular Sampling: A New Method for Predicting Ovarian Cancer in Vascularized Complex Adnexal Masses," *J Ultrasound Med*, vol. 24, pp. 689-696, 2005.
- [55] M. J. Kudla, I. E. Timor-Tritsch, J. M. Hope, *et al.*, "Spherical Tissue Sampling in 3-Dimensional Power Doppler Angiography: A New Approach for Evaluation of Ovarian Tumors," *J Ultrasound Med*, vol. 27, pp. 425-433, 2008.
- [56] L. T. Merce, J. L. Alcazar, C. Lopez, *et al.*, "Clinical Usefulness of 3-Dimensional Sonography and Power Doppler Angiography for Diagnosis of Endometrial Carcinoma," *J Ultrasound Med*, vol. 26, pp. 1279-1287, 2007.
- [57] R. Galván, L. Mercé, M. Jurado, *et al.*, "Three-Dimensional Power Doppler Angiography in Endometrial Cancer: Correlation with Tumor Characteristics," *Ultrasound Obstet Gynecol*, vol. 35, pp. 723-729, 2010.
- [58] A. C. Testa, S. Ajossa, G. Ferrandina, *et al.*, "Does Quantitative Analysis of Three-Dimensional Power Doppler Angiography Have a Role in the Diagnosis of Malignant Pelvic Solid Tumors? A Preliminary Study," *Ultrasound Obstet Gynecol*, vol. 26, pp. 67-72, 2005.
- [59] S. J. Kuo, Y. H. Hsiao, Y. L. Huang, *et al.*, "Classification of Benign and Malignant Breast Tumors Using Neural Networks and Three-Dimensional Power Doppler Ultrasound," *Ultrasound Obstet Gynecol*, vol. 32, pp. 97-102, 2008.

- [60] J. J. Chen, S. Y. Fu, C. S. Chiang, *et al.*, "A Preclinical Study to Explore Vasculature Differences between Primary and Recurrent Tumors Using Ultrasound Doppler Imaging," *Ultrasound Med Biol*, vol. 39, pp. 860-869, 2013.
- [61] A. P. Moskalik, M. A. Rubin, K. J. Wojno, *et al.*, "Analysis of Three-Dimensional Doppler Ultrasonographic Quantitative Measures for the Discrimination of Prostate Cancer," *J Ultrasound Med*, vol. 20, pp. 713-722, 2001.
- [62] L. M. Nardoza, E. Araújo Júnior, C. Simioni, *et al.*, "Evolution of 3-D Power Doppler Indices of Fetal Brain in Normal Pregnancy," *Ultrasound Med Biol*, vol. 35, pp. 545-549, 2009.
- [63] A. Rossi, I. Romanello, L. Forzano, *et al.*, "Evaluation of Fetal Cerebral Blood Flow Perfusion Using Power Doppler Ultrasound Angiography (3d-Pda) in Growth-Restricted Fetuses," *Facts Views Vis Obgyn*, vol. 3, pp. 175-180, 2011.
- [64] C. H. Chang, C. H. Yu, H. C. Ko, *et al.*, "Assessment of Normal Fetal Liver Blood Flow Using Quantitative Three-Dimensional Power Doppler Ultrasound," *Ultrasound Med Biol*, vol. 29, pp. 943-949, 2003.
- [65] M. Dubiel, G. H. Breborowicz, M. Ropacka, *et al.*, "Computer Analysis of Three-Dimensional Power Angiography Images of Foetal Cerebral, Lung and Placental Circulation in Normal and High-Risk Pregnancy," *Ultrasound Med Biol*, vol. 31, pp. 321-327, 2005.
- [66] R. Ruano, M. C. Aubry, B. Barthe, *et al.*, "Quantitative Analysis of Fetal Pulmonary Vasculature by 3-Dimensional Power Doppler Ultrasonography in Isolated Congenital Diaphragmatic Hernia," *Am J Obstet Gynecol*, vol. 195, pp. 1720-1728, 2006.
- [67] N. Bozkurt, A. Başgöl Yigiter, H. Gokaslan, *et al.*, "Correlations of Fetal-Maternal Outcomes and First Trimester 3-D Placental Volume/3-D Power Doppler Calculations," *Clin Exp Obstet Gynecol*, vol. 37, pp. 26-28, 2010.
- [68] O. Morel, F. Pachy, P. Chavatte-Palmer, *et al.*, "Correlation between Uteroplacental Three-Dimensional Power Doppler Indices and True Uterine Blood Flow: Evaluation in a Pregnant Sheep Model," *Ultrasound Obstet Gynecol*, vol. 36, pp. 635-640, 2010.
- [69] H. A. Guimarães Filho, R. Mattar, E. Araujo Júnior, *et al.*, "Reproducibility of Three-Dimensional Power Doppler Placental Vascular Indices in Pregnancies between 26 and 35 Weeks," *Arch Gynecol Obstet*, vol. 283, pp. 213-217, 2011.
- [70] N. W. Jones, N. J. Raine-Fenning, H. A. Mousa, *et al.*, "Evaluating the Intra- and Interobserver Reliability of Three-Dimensional Ultrasound and Power Doppler Angiography (3d-Pda) for Assessment of Placental Volume and Vascularity in the Second Trimester of Pregnancy," *Ultrasound Med Biol*, vol. 37, pp. 376-385, 2011.

- [71] R. Negrini, L. C. de Silva Bussamra, L. da Silva Valladão de Freitas, *et al.*, "Assessment of Placental Blood Flow between 22 and 34 Weeks of Gestation by 3d-Sonography Power Doppler Vascular Indices," *Arch Gynecol Obstet*, vol. 284, pp. 53-57, 2011.
- [72] G. Rizzo, A. Capponi, O. Cavicchioni, *et al.*, "First Trimester Uterine Doppler and Three-Dimensional Ultrasound Placental Volume Calculation in Predicting Pre-Eclampsia," *Eur J Obstet Gynecol Reprod Biol*, vol. 138, pp. 147-151, 2008.
- [73] P. Dar, J. Gebb, L. Reimers, *et al.*, "First-Trimester 3-Dimensional Power Doppler of the Uteroplacental Circulation Space: A Potential Screening Method for Preeclampsia," *Am J Obstet Gynecol*, vol. 203, pp. 238.e231-237, 2010.
- [74] A. O. Odibo, K. R. Goetzinger, K. M. Huster, *et al.*, "Placental Volume and Vascular Flow Assessed by 3d Power Doppler and Adverse Pregnancy Outcomes," *Placenta*, vol. 32, pp. 230-234, 2011.
- [75] M. Pomorski, M. Zimmer, J. Florjanski, *et al.*, "Comparative Analysis of Placental Vasculature and Placental Volume in Normal and Iugr Pregnancies with the Use of Three-Dimensional Power Doppler," *Arch Gynecol Obstet*, vol. 285, pp. 331-337, 2012.
- [76] E. H. Ng, C. C. Chan, O. S. Tang, *et al.*, "Endometrial and Subendometrial Blood Flow Measured by Three-Dimensional Power Doppler Ultrasound in Patients with Small Intramural Uterine Fibroids During Ivf Treatment," *Hum Reprod*, vol. 20, pp. 501-506, 2005.
- [77] L. T. Merce, M. J. Barco, and S. Bau, "2d and 3d Power Doppler Ultrasound of Endometrium as Implantation Marker," *DSJUOG*, vol. 2, pp. 1-11, 2008.
- [78] M. Cardinal E Fau - Lafortune, P. Lafortune M Fau - Burns, and P. Burns, "Power Doppler Us in Synovitis: Reality or Artifact?," *Radiology*, vol. 200, p. 868, 1996.
- [79] S. P. Jain, P. H. Fan, E. F. Philpot, *et al.*, "Influence of Various Instrument Settings on the Flow Information Derived from the Power Mode," *Ultrasound Med Biol*, vol. 17, pp. 49-54, 1991.
- [80] S. Gudmundsson, L. Valentin, J. Pirhonen, *et al.*, "Factors Affecting Color Doppler Energy Ultrasound Recordings in an in-Vitro Model," *Ultrasound Med Biol*, vol. 24, pp. 899-902, 1998.
- [81] S. Deverson and D. H. Evans, "Using Doppler Signal Power to Detect Changes in Vessel Size: A Feasibility Study Using a Wall-Less Flow Phantom," *Ultrasound Med Biol*, vol. 26, pp. 593-602, 2000.
- [82] K. Mizushige, T. Ueda, M. Yuba, *et al.*, "Dependence of Power Doppler Image on a High Pass Filter Instrumented in Ultrasound Machine," *Ultrasound Med Biol*, vol. 25, pp. 1389-1393, 1999.

- [83] J. B. Kruskal, P. A. Newman, L. G. Sammons, *et al.*, "Optimizing Doppler and Color Flow Us: Application to Hepatic Sonography," *Radiographics*, vol. 24, pp. 657-675, 2004.
- [84] J. E. Browne, A. J. Watson, P. R. Hoskins, *et al.*, "Validation of a Sensitivity Performance Index Test Protocol and Evaluation of Colour Doppler Sensitivity for a Range of Ultrasound Scanners," *Ultrasound Med Biol*, vol. 30, pp. 1475-1483, 2004.
- [85] D. Garcia, M. Fenech, Z. Qin, *et al.*, "Signal Losses with Real-Time Three-Dimensional Power Doppler Imaging," *Ultrasound Med Biol*, vol. 33, pp. 1632-1639, 2007.
- [86] A. Welsh, "Quantification of Power Doppler and the Index 'Fractional Moving Blood Volume' (Fmbv)," *Ultrasound Obstet Gynecol*, vol. 23, pp. 323-326, 2004.
- [87] J. L. Alcázar, "Three-Dimensional Power Doppler Derived Vascular Indices What Are We Measuring and How Are We Doing It?," *Ultrasound Obstet Gynecol*, vol. 32, pp. 485-487, 2008.
- [88] N. J. Raine-Fenning, N. M. Nordin, K. V. Ramnarine, *et al.*, "Evaluation of the Effect of Machine Settings on Quantitative Three-Dimensional Power Doppler Angiography an in-Vitro Flow Phantom Experiment.," *Ultrasound Obstet Gynecol*, vol. 32, pp. 551-559, 2008.
- [89] W. P. Martins, "Three-Dimensional Power Doppler: Validity and Reliability," *Ultrasound Obstet Gynecol*, vol. 36, pp. 530-533, 2010.
- [90] M. J. Schulten-Wijman, P. C. Struijk, C. Brezinka, *et al.*, "Evaluation of Volume Vascularization Index and Flow Index: A Phantom Study," *Ultrasound Obstet Gynecol*, vol. 32, pp. 560-564, 2008.
- [91] W. P. Martins, N. J. Raine-Fenning, R. A. Ferriani, *et al.*, "Quantitative Three-Dimensional Power Doppler Angiography: A Flow-Free Phantom Experiment to Evaluate the Relationship between Color Gain, Depth and Signal Artifact," *Ultrasound Obstet Gynecol*, vol. 35, pp. 361-368, 2010.
- [92] S. C. Campbell, D. J. Cullinan Ja Fau - Rubens, and D. J. Rubens, "Slow Flow or No Flow? Color and Power Doppler Us Pitfalls in the Abdomen and Pelvis," 2004.
- [93] C.-Y. Wu, M.-T. Lo, J. Tsao, *et al.*, "Factor Analysis in Both Spatial and Temporal Domains of Color Blooming Artifacts in Ultrasound Investigations Utilizing Contrast Agents," *Comput Med Imaging Graph*, vol. 28, p. 129, 2004.
- [94] T. R. Nelson, D. H. Pretorius, A. Hull, *et al.*, "Sources and Impact of Artifacts on Clinical Three-Dimensional Ultrasound Imaging," *Ultrasound Obstet Gynecol*, vol. 16, pp. 374-383, 2000.

- [95] A. Nilsson, "Artefacts in Sonography and Doppler," *European radiology*, vol. 11, pp. 1308-1315, 2001.
- [96] Z. Guo and A. Fenster, "Three-Dimensional Power Doppler Imaging: A Phantom Study to Quantify Vessel Stenosis," *Ultrasound Med Biol*, vol. 22, pp. 1059-1069, 1996.
- [97] B. I. Choi, T. K. Kim, J. K. Han, *et al.*, "Vascularity of Hepatocellular Carcinoma: Assessment with Contrast-Enhanced Second-Harmonic Versus Conventional Power Doppler Us," *Radiology*, vol. 214, pp. 381-386, 2000.
- [98] M. Claudon, D. Winninger, S. Briançon, *et al.*, "Power Doppler Us: Evaluation of the Morphology of Stenoses with a Flow Phantom," *Radiology*, vol. 218, pp. 109-117, 2001.
- [99] F. A. Camfferman, G. M. Ecury-Goossen, J. E. La Roche, *et al.*, "Calibrating Doppler Imaging of Preterm Intracerebral Circulation Using a Microvessel Flow Phantom," *Front Hum Neurosci*, vol. 8, p. 1068, 2014.
- [100] S. L. Collins, G. N. Stevenson, J. A. Noble, *et al.*, "Influence of Power Doppler Gain Setting on Virtual Organ Computer-Aided Analysis Indices in Vivo: Can Use of the Individual Sub-Noise Gain Level Optimize Information?," *Ultrasound Obstet Gynecol*, vol. 40, pp. 75-80, 2012.
- [101] R. Galván, L. Mercé, M. Jurado, *et al.*, "Three-Dimensional Power Doppler Angiography in Endometrial Cancer: Correlation with Tumor Characteristics," *Ultrasound Obstet Gynecol*, vol. 35, pp. 723-729, 2010.
- [102] E. Quaia and SpringerLink (Online service), *Radiological Imaging of the Kidney*. Berlin, Heidelberg: Springer-Verlag Berlin Heidelberg,, 2011.
- [103] D. Kruse, R. Silverman, S. Erickson, *et al.*, "Optimization of Real-Time High Frequency Ultrasound for Blood Flow Imaging in the Microcirculation," in *Ultrasonics Symposium, 2000 IEEE*, pp. 1461-1464 vol.1462, Oct 2000.
- [104] D. F. Ten Cate, J. J. Luime, M. van der Ven, *et al.*, "Very Different Performance of the Power Doppler Modalities of Several Ultrasound Machines Ascertained by a Microvessel Flow Phantom," *Arthritis Res Ther*, vol. 15, p. R162, 2013.
- [105] R. Sakano, T. Kamishima, M. Nishida, *et al.*, "Power Doppler Signal Calibration between Ultrasound Machines by Use of a Capillary-Flow Phantom for Pannus Vascularity in Rheumatoid Finger Joints: A Basic Study," *Radiological Physics and Technology*, vol. 8, pp. 120-124, 2015.
- [106] P. Avramovski, "Value of Ultrasound Machine Settings Optimization for Better Diagnosis of Focal Liver Lesions," *Maced J Med Sci*, vol. 2, pp. 149-152, 2009.

- [107] S. T. Torp-Pedersen and L. Terslev, "Settings and Artefacts Relevant in Colour/Power Doppler Ultrasound in Rheumatology," *Ann Rheum Dis*, vol. 67, pp. 143-149, 2008.
- [108] S. Bjaerum, H. Torp, and K. Kristoffersen, "Clutter Filter Design for Ultrasound Color Flow Imaging," *IEEE transactions on ultrasonics, ferroelectrics, and frequency control*, vol. 49, pp. 204-216, 2002.
- [109] R. B. Peterson, L. E. Atlas, and K. W. Beach, "A Comparison of Iir Initialization Techniques for Improved Color Doppler Wall Filter Performance," in *Ultrasonics Symposium, 1994. Proceedings., 1994 IEEE*, pp. 1705-1708 vol.1703, Oct. 31 1994-Nov. 3 1994.
- [110] L. Thomas and A. Hall, "An Improved Wall Filter for Flow Imaging of Low Velocity Flow," in *Ultrasonics Symposium, 1994. Proceedings., 1994 IEEE*, pp. 1701-1704 vol.1703, Oct. 31 1994-Nov. 3 1994.
- [111] L. A. Ledoux, P. J. Brands, and A. P. Hoeks, "Reduction of the Clutter Component in Doppler Ultrasound Signals Based on Singular Value Decomposition: A Simulation Study," *Ultrason Imaging*, vol. 19, pp. 1-18, 1997.
- [112] S. Bjaerum, H. Torp, and K. Kristoffersen, "Clutter Filters Adapted to Tissue Motion in Ultrasound Color Flow Imaging," *IEEE Trans Ultrason Ferroelectr Freq Control*, vol. 49, pp. 693-704, 2002.
- [113] D. E. Kruse and K. W. Ferrara, "A New High Resolution Color Flow System Using an Eigendecomposition-Based Adaptive Filter for Clutter Rejection," *IEEE Trans Ultrason Ferroelectr Freq Control*, vol. 49, pp. 1739-1754, 2002.
- [114] Y. M. Yoo, R. Managuli, and Y. Kim, "Adaptive Clutter Filtering for Ultrasound Color Flow Imaging," *Ultrasound Med Biol*, vol. 29, pp. 1311-1320, 2003.
- [115] Y. M. Yoo and Y. Kim, "New Adaptive Clutter Rejection for Ultrasound Color Doppler Imaging: In Vivo Study," *Ultrasound Med Biol*, vol. 36, pp. 480-487, 2010.
- [116] A. Yu and L. Lovstakken, "Eigen-Based Clutter Filter Design for Ultrasound Color Flow Imaging: A Review," *IEEE Trans Ultrason Ferroelectr Freq Control*, vol. 57, pp. 1096-1111, 2010.
- [117] S. Z. Pinter and J. C. Lacefield, "Detectability of Small Blood Vessels with High-Frequency Power Doppler and Selection of Wall Filter Cut-Off Velocity for Microvascular Imaging," *Ultrasound in medicine & biology*, vol. 35, pp. 1217-1228, 2009.
- [118] R. J. Zemp and M. F. Insana, "Experimental Validation of a Power Doppler Performance Model," in *Ultrasonics, 2003 IEEE Symposium on*, pp. 861-864 Vol.861, 5-8 Oct. 2003.

- [119] S. Z. Pinter and J. C. Lacefield, "Detectability of Small Blood Vessels with High-Frequency Power Doppler and Selection of Wall Filter Cut-Off Velocity for Microvascular Imaging," *Ultrasound Med Biol*, vol. 35, pp. 1217-1228, 2009.
- [120] S. Z. Pinter and J. C. Lacefield, "Objective Selection of High-Frequency Power Doppler Wall Filter Cutoff Velocity for Regions of Interest Containing Multiple Small Vessels," *IEEE Trans Med Imaging*, vol. 29, pp. 1124-1139, 2010.
- [121] H. Hashimoto, Y. Shen, Y. Takeuchi, *et al.*, "Ultrasound 3-Dimensional Image Processing Using Power Doppler Image," in *Ultrasonics Symposium, 1995. Proceedings., 1995 IEEE*, pp. 1423-1426 vol.1422, 7-10 Nov 1995.
- [122] B. Cigale, S. Šinjur, and D. Zazula, "Automated Quantitative Assessment of Perifollicular Vascularization Using power Doppler Ultrasound Images " *WSEAS Trans Comp*, vol. 9, pp. 194-203, 2010.
- [123] T. Schlosser, C. Pohl, S. Kuntz-Hehner, *et al.*, "Echoscintigraphy: A New Imaging Modality for the Reduction of Color Blooming and Acoustic Shadowing in Contrast Sonography," *Ultrasound Med Biol*, vol. 29, pp. 985-991, 2003.

Chapter 2

Improved objective selection of power Doppler wall-filter cut-off velocity for accurate vascular quantification

The content of this chapter has been adapted from: "Improved objective selection of power Doppler wall-filter cut-off velocity for accurate vascular quantification," published in Ultrasound Med. Biol., vol. 38, p. 1429, 2012, by M. Elfarnawany, S. Z. Pinter, and J. C. Lacefield.

2.1 Introduction

Microvascular imaging is important in the study and development of treatments for cancer and other angiogenesis-dependent diseases such as psoriasis, endometriosis, and atherosclerosis [1, 2]. In angiogenesis studies, the hemodynamic parameters blood volume and blood flow are often quantified using imaging modalities such as dynamic contrast-enhanced magnetic resonance imaging (DCE-MRI), dynamic contrast-enhanced x-ray computed tomography (DCE-CT), and functional positron emission tomography (PET) [3]. In comparison to these modalities, power Doppler ultrasound, which is also sensitive to blood volume, is attractive for longitudinal studies because it does not require repeated injections of contrast media and avoids the exposure to ionizing radiation that accompanies DCE-CT and functional PET.

However, the quantitative accuracy of power Doppler images depends on the skill and experience of the operator in selecting acquisition parameters such as gain, pulse repetition frequency, and wall filter cut-off velocity [4-6]. Doppler power is strongly correlated with the wall-filter cut-off velocity [7] and effective clutter filtering is

particularly difficult when imaging slow-moving blood [8]. When imaging small blood vessels with slow flow velocities, if the selected cut-off is too low, false-positive color pixels will result, whereas selecting a cut-off velocity that is too high leads to false-negative artifacts and a possible loss of vessel continuity [5, 9]. Furthermore, in longitudinal studies that involve serial measurements of vascularity, the Doppler settings are typically chosen in advance and fixed throughout the course of a study. Since angiogenic vasculature experiences changes in structure and function over time [10, 11], the optimal Doppler settings should also vary. However, if the Doppler settings were adjusted based on the operator's judgment, an unacceptable risk of experimenter bias would be introduced. To provide a reliable basis for adapting these parameters, we developed an objective method, the wall filter selection curve (WFSC), to select the wall filter cut-off velocity Pinter [12, 13]. The WFSC method could potentially be applied to tune other acquisition parameters as well. In this chapter, the WFSC method is redesigned to be more automated and to improve the accuracy of vascular quantification using power Doppler.

Much of the recent progress toward automated selection of Doppler acquisition parameters can be found in the patent literature. Mo et al. introduced a method for adaptive wall filtering in spectral Doppler that uses a pre-constructed noise model to predict clutter power and select the most suitable filter cut-off accordingly [14]. They revised this method for color flow imaging as an iterative algorithm that compares the power and the mean frequency of a wall-filtered Doppler signal to predetermined thresholds to assess the suitability of the selected cut-off frequency [15, 16]. Kim et al. proposed another iterative algorithm that defines the cut-off frequency as a function of the Doppler signal's mean frequency [16]. In this method, a set of metrics is computed for the pre- and post-wall-filtered data and those metrics are combined with fixed or user-determined thresholds to evaluate the suitability of the cut-off frequency being tested. The above methods depend on predetermined values or predicted models, which are difficult to compile and standardize for different imaging applications or across different Doppler systems. In contrast, Lee et al. introduced a numerical optimization method for spectral Doppler that depends on information extracted from the measured data rather than predetermined values or relationships [17]. In their method, a feature of the data is

identified, such as the signal-to-noise ratio summed over a 2-D time and velocity window that depends strongly on the acquisition parameter to be tuned. The acquisition parameter is varied to search for the setting at which the data-dependent feature best corresponds to a goal value such as its maximum or average. The difficulty in applying the Lee *et al.* method to power Doppler is that specific image-based quantities and goal values would have to be defined for each parameter to be tuned and no guidance is provided that would enable these quantities and goals to be determined from Doppler image data.

In our original WFSC method [12, 13], the wall-filter selection curve is constructed by plotting the color pixel density (CPD) as a function of the cut-off velocity of the wall filter, where the CPD is equal to the ratio of colored pixels to the total number of pixels in a region of interest (ROI). A mathematical model developed in [13] describes the relationship between power Doppler CPD and the wall filter cut-off velocity as a signal detection problem in which true-positive color pixels can occur within the vessel(s) and false-positive color pixels can occur in the tissue background. This relationship can be described for an ROI enclosing multiple vessels as:

$$CPD(v_c) = \sum_{i=1}^N F_{v(i)} TPF_i(v_c) + (1 - \sum_{i=1}^N F_{v(i)}) FPF(v_c) \quad \text{Eqn. 2-1}$$

where v_c is the wall filter cut-off velocity, $TPF_i(v_c)$ is the true-positive fraction within the i th vessel and $FPF(v_c)$ is the false-positive fraction obtained as the cut-off velocity is varied, and $F_{v(i)}$ is the volume fraction occupied by the i th vessel within the ROI. The mathematical model predicts that the WFSC will possess one or more characteristic plateaus as shown in Figure 2-1. We have shown in microcirculation-mimicking flow phantoms [12, 13] and in power Doppler images of testicles of two mice [12], that experimental selection curves do possess such plateaus. If a plateau satisfies specific criteria for its length and its position along the cut-off velocity axis, the CPD along the plateau yields an accurate estimate of the vascular volume fraction in the ROI.

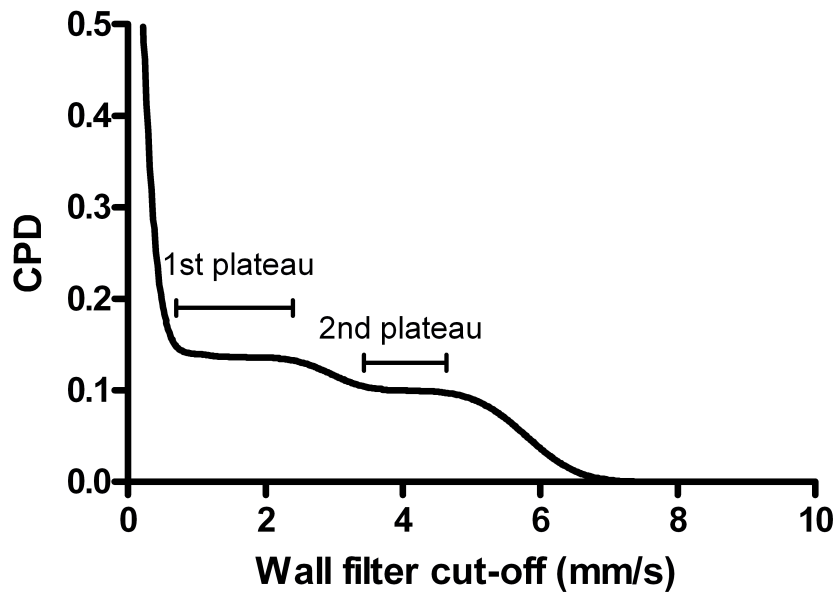


Figure 2-1: Theoretical wall-filter selection curve (Eqn 2-1) for a region of interest containing two vessels. The horizontal bars identify the bounds of the two plateaus. The first plateau corresponds to cut-off velocities at which both vessels are filled with color pixels, whereas the second plateau corresponds to cut-off velocities where color pixels remain in the higher flow rate, more easily detected vessel only.

Our previous studies also identified several opportunities to improve the performance of the WFSC method. First, analogous to the [14], [15, 16] methods, our original method identified plateaus in WFSCs by comparing the relative first difference in CPD to an empirically determined threshold. The value of this threshold differed for the flow-phantom and murine data and therefore was not universally applicable. Second, the detected plateaus were often non-stationary (*i.e.*, non-zero slope), but the original method did not include a means of choosing an operating point along a plateau and instead always treated the right end of the plateau as the best choice of cut-off velocity. Third, in WFSCs for ROIs containing multiple vessels, the original method selected a

cut-off velocity that was most suitable for imaging the dominant vessel in the ROI, which in some cases compromised the display and quantification of the remaining vessels.

In this chapter, we introduce a redesigned WFSC method that addresses these challenges. In the redesigned method, an N -point maximum envelope peak (MEP) search algorithm [18] is applied to detect characteristic intervals on the selection curves without the need to specify a predetermined threshold value. The slopes of the selection curve intervals detected by the redesigned algorithm were occasionally steeper than expected, so we hereafter refer to these features as “characteristic intervals” rather than “plateaus” to avoid the implication that the method relies on the existence of approximately horizontal segments in the WFSC. Since the characteristic intervals can be sloped, it is now even more necessary to identify a specific operating point along the WFSC. We therefore introduce a multiple-step decision algorithm that selects an operating point at either the right end or the center of the characteristic interval. Finally, the redesigned method subdivides the ROI into small subregions, selects an operating point cut-off velocity for each subregion, and reconstructs an image using the potentially different cut-off velocities in each subregion. This approach tunes the cut-off velocity to more effectively depict different vessels, thereby preventing a dominant vessel from skewing the CPD estimate. (The general concept of subdividing the ROI was also suggested independently in a patent by Bakircioglu [19], but few details were provided in that patent about how the subdivision should be implemented.) In the following sections, the redesigned WFSC method is described in more detail and its improved performance is demonstrated by reprocessing four-vessel flow phantom images from [13]. The results are a promising indication of the potential to fully automate the wall filter cut-off velocity setting in a power Doppler system using the WFSC method.

2.2 Materials and Methods

2.2.1 Dividing an ROI into subregions

The original ROI is divided into the smallest possible non-overlapping, rectangular subregions of equal dimensions. In this study, the entire Doppler color box is used as the original ROI, but the method could be applied to any region segmented by the

user. The original ROI is initially divided into a large number of rows and columns, for example 9 rows by 9 columns. The CPD is computed for each subregion using the lowest available cut-off velocity, which was typically 0.3 mm/s in this study. If no subregion yields a $CPD > 0.80$, the original ROI is repartitioned into smaller subregions. Repartitioning into equal numbers of rows and columns ($K \times K$) continues until at least one subregion possesses a $CPD > 0.80$. The final partition will consist of either $(K-1) \times (K-1)$, $K \times (K-1)$, or $(K-1) \times K$ rows and columns. Of these three options, the partition that yields the highest maximum CPD is chosen, subject to the constraint that the CPD must be < 0.80 in all subregions. The value of that threshold, 0.80, was selected empirically by experimentation with the flow phantom data. This approach is designed to ensure that most subregions containing flow have relatively high CPD, which prevents the algorithm from inappropriately interpreting a small number of false-positive color pixels as significant flow in regions with little actual vascularity. Conversely, if subregions containing more than 80% true-positive color pixels were allowed, the CPD would not vary sufficiently smoothly as a function of cut-off velocity to produce meaningful characteristic features in the WFSC for such subregions.

2.2.2 Detection of characteristic intervals in a WFSC

The variation of CPD along a WFSC is evaluated by computing the normalized absolute first difference of the CPD, $|\Delta CPD|_{norm}$:

$$|\Delta CPD|_{norm} = \frac{|CPD_2 - CPD_1|}{\max(CPD)} \quad \text{Eqn. 2-2}$$

where CPD_1 and CPD_2 are the CPD values of two successive data points on the selection curve and $\max(CPD)$ is the maximum value of CPD along the WFSC. For purposes of visualization, $|\Delta CPD|_{norm}$ is plotted as bars overlaying the WFSC, as illustrated in Figure 2-2. Characteristic intervals of a WFSC are bounded at each end by prominent local maxima in $|\Delta CPD|_{norm}$. These prominent local maxima are detected by applying the N -point maximum envelope peak (MEP) search [18].

The MEP search detects local maxima in a low-pass filtered version of the envelope of the input data, which in this case is $|\Delta\text{CPD}|_{\text{norm}}$. In each iteration of the MEP search, an N -point window slides across the $|\Delta\text{CPD}|_{\text{norm}}$ data in one-sample steps. In our implementation, the length of the window, N , is computed by dividing the total number of data points by five and rounding down to the nearest integer. Division by five is used because a WFSC that includes two characteristic intervals consists of five distinct segments, the two characteristic intervals plus the segments before, after, and between them. This approach yielded an initial window length between 3 and 5 points, which provided good performance with the flow-phantom data. At each window position, the relative maximum of $|\Delta\text{CPD}|_{\text{norm}}$, *i.e.*, the maximum value of $|\Delta\text{CPD}|_{\text{norm}}$ within the window, is identified. The result of this operation, which we refer to as the filtered envelope, is a sequence of distinct relative maxima in the $|\Delta\text{CPD}|_{\text{norm}}$ data, such that if one $|\Delta\text{CPD}|_{\text{norm}}$ sample is the relative maximum for multiple window positions, it only appears once in the filtered envelope. In the example shown in Figure 2-2, the filtered envelope produced by the first iteration of the MEP search is represented by the black line in Figure 2(b).

Characteristic intervals are detected whenever three successive points in the filtered envelope form a V shape indicating an interval of high, low, and then high $|\Delta\text{CPD}|_{\text{norm}}$, as highlighted by the two sets of red crosses in Figure 2-2(b). Each V shape corresponds to a candidate characteristic interval whose location along the cut-off velocity axis is saved for further analysis. The filtered envelope obtained from the first iteration of the MEP search is used as input data to the second iteration of the search. In the example of Figure 2-2, the second iteration yields the filtered envelope shown in Figure 2-2(c) that contributes one more candidate characteristic interval. The process is repeated until the filtered envelope contains only three points. At each step of the iteration, the filtered envelope will have fewer samples, so the length of the N -point window is reduced in each step, subject to the constraint that N must be at least two samples.

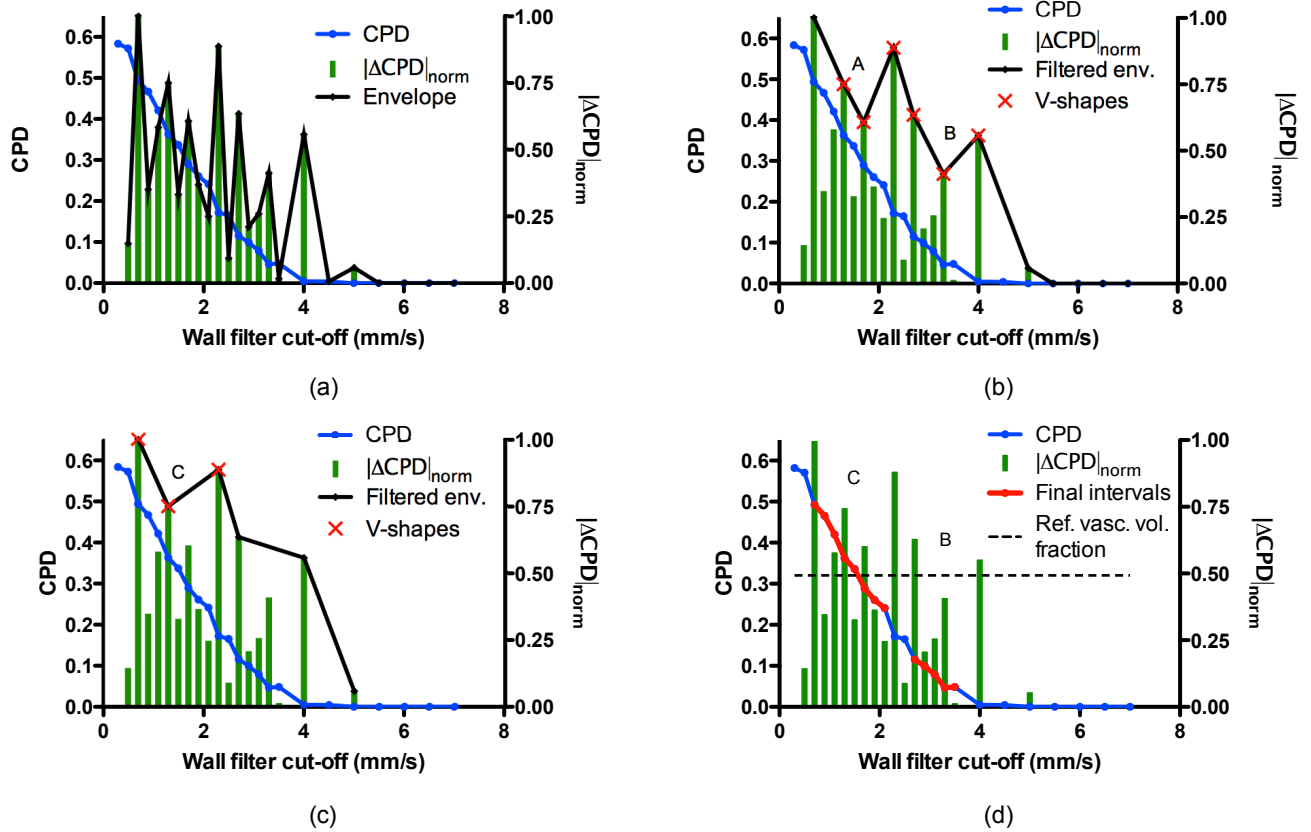


Figure 2-2: Iterative detection of characteristic intervals. (a) A wall filter selection curve (WFSC), color pixel density (CPD) plotted as a function of wall filter cut-off velocity, is shown using the blue line and left-hand y-axis. The normalized absolute first difference of the CPD, $|\Delta\text{CPD}|_{\text{norm}}$ (Eqn 2-2), is plotted using the green bars and the right-hand y-axis. The black curve is the envelope of the $|\Delta\text{CPD}|_{\text{norm}}$ data. **(b)** Results of the first iteration of the N -point maximum envelope peak (MEP) search. The initial filtered envelope is shown in black. Two candidate characteristic intervals, A and B, are identified by the V shapes in the filtered envelope (red crosses). **(c)** Results of the second iteration of the MEP search displayed using the same format as panel (b). **(d)** The final detected characteristic intervals, C and B, are highlighted in red on the WFSC. The reference vascular volume fraction of the subregion is indicated by the horizontal dashed line.

The candidate characteristic intervals identified by each iteration of the MEP search are compared to eliminate duplicate intervals and merge intervals that share a common endpoint. If a longer candidate interval completely overlaps a shorter candidate interval, only the longer interval is retained. Since WFSCs asymptotically converge to zero CPD at high cut-off velocities, the algorithm may inappropriately interpret small fluctuations in CPD as defining a spurious characteristic interval at very low CPD. To prevent such artifacts, any interval whose mean CPD corresponds to a single color pixel is also discarded. The one or more intervals that remain after these rules are applied are the final detected intervals.

In the example shown in Figure 2-2, the first iteration yields an interval labeled A from 1.3 to 2.1 mm/s and an interval B from 2.7 to 3.5 mm/s. The second iteration yields a third candidate interval C from 0.7 to 2.1 mm/s. Since interval C completely overlaps interval A, the latter interval is discarded, so B and C are the final detected intervals (Figure 2-2(d)).

2.2.3 Selection of operating cut-off velocity along a characteristic interval

Since characteristic intervals may be horizontal or sloped, a method is needed to choose an operating point along the interval. A multiple-step decision algorithm, outlined in the flow chart in Figure 2-3, was designed to select an operating point at either the right end or the center of the characteristic interval. This algorithm was developed by experimentation with the flow-phantom data, but, as is explained in the Discussion section, it can also be justified by referring to the mathematical model of the WFSC that was introduced in [13]. The choice of the operating point depends on the slope of the interval in comparison to the slopes of the surrounding segments of the WFSC. If more than one characteristic interval is detected, the middle or the right end of the first interval (*i.e.*, interval C in Figure 2-2) is chosen depending on the rank of its slope, as illustrated in Step 1 of Figure 2-3. If only one interval is detected, the slope of the interval is also compared to the slopes of the characteristic intervals of the other subregions in the ROI (Step 2 of Figure 2-3). Slopes are ranked lowest, middle or highest in comparison to the slopes of the surrounding segments of the selection curve as illustrated schematically in Figure 2-3. The purpose of these comparisons is to guarantee that the center of the

interval is only selected for the most inclined intervals among all the subregions; otherwise, the right end of the interval is the operating point.

2.2.4 ROI reconstruction

The characteristic-interval-detection and operating-point-selection algorithms are applied individually to each subregion in the ROI. Once an operating point is selected for a subregion, eleven power Doppler image frames acquired at that cut-off velocity are averaged. Eleven frames were sufficient for averaging because the frame-to-frame variability of the CPD was small [13]. If no characteristic interval was detected in the WFSC for a particular subregion, that subregion is assumed to contain no flow, and B-mode image frames rather than power Doppler frames are averaged. The averaged subregion images are then tiled together to produce a reconstructed image of the ROI. Vascularity is quantified in the reconstructed image by computing the CPD.

2.2.5 Power Doppler image acquisition

The redesigned WFSC algorithm was implemented in Matlab 7 (The MathWorks Inc., Natick, MA) and applied to previously acquired power Doppler images of a four-vessel flow phantom [13] for evaluation. The outer diameters of the four vessels were 200, 250, 250, and 300 μm . The flow rate of the blood-mimicking fluid was 6000 $\mu\text{l/hr}$, which corresponded to flow velocities of 5.4--9.6 mm/s. Power Doppler images were acquired using a Vevo 770 swept-scan high-frequency ultrasound system (VisualSonics, Toronto, ON, Canada) with a 30-MHz transducer (model RMV707, 12.7 mm focal length, 55 μm axial resolution, 115 μm lateral resolution, 2.2 mm depth of field). Images were acquired in three different transducer orientations to obtain planes showing high, medium, and low levels of vascularity. Images were acquired at incrementally increasing wall filter cut-off velocities until minimal flow was present in the power Doppler images. Eleven frames were recorded at each wall filter cut-off. In each image, the power Doppler color box, which was 2.5 mm (axial) \times 3 mm (lateral), exhibited vertical bands of color pixels at its lateral boundaries due to the change in direction of the mechanically scanned probe. Therefore, 15-pixel (0.27 mm) columns were cropped from both lateral boundaries

of the color box to yield an ROI of 140 pixels (axial) ×138 pixels (lateral) for WFSC processing.

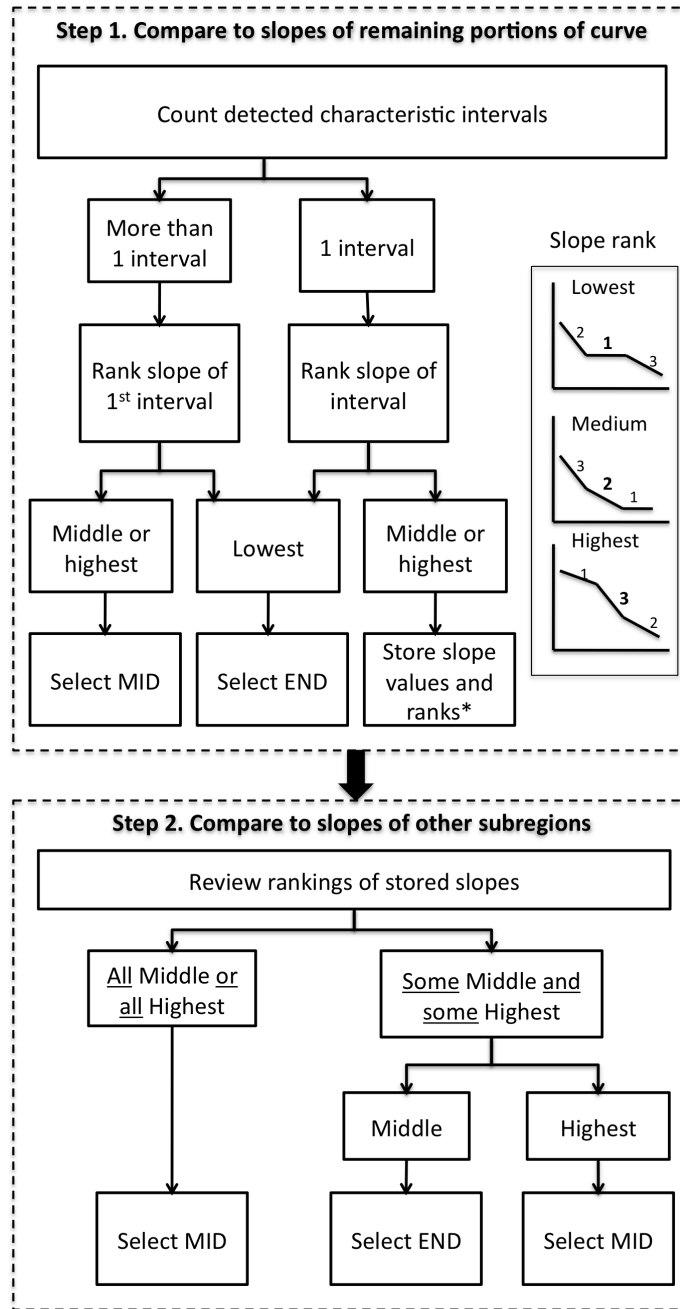


Figure 2-3: Flow chart for selection of an operating point cut-off velocity along a characteristic interval. Two steps are shown; the second step is only applied to the slopes stored in the box indicated with “*”. The concept of ranking slopes as low (1), middle (2), or high (3) is defined schematically next to the flow chart.

For each of the three fields of view, a mask image was generated to estimate the reference vascular volume fraction of that slice through the phantom. Mask images were computed from a set of four B-mode images of the phantom as follows. First, the B-mode gray scale was linearized by inverting the logarithmic compression function specified by the manufacturer [20]. The four images were grouped into two pairs. Each pair of linearized images was subtracted, then each difference image was normalized by its maximum pixel magnitude, and the two normalized images were averaged to produce a single image. Vessels in the averaged image were manually segmented using ImageJ (U.S. National Institutes of Health, Maryland, USA) by free-hand selection of an initial vessel contour that was subsequently smoothed by fitting a cubic spline. Manual vessel segmentation was repeated five times for each field of view and the segmentation that yielded the median estimated vascular volume fraction was used as the reference mask image for that ROI.

2.2.6 Performance analysis of WFSC method

The performance of each step of the redesigned WFSC method was evaluated individually. First, to confirm that the automated algorithm for characteristic interval detection functions as intended, the locations of the detected intervals were visually compared to the locations of prominent local maxima in the $|\Delta\text{CPD}|_{\text{norm}}$ data. The accuracy of characteristic interval detection was also evaluated by comparing the CPD values along the intervals to the reference vascular volume fraction estimated for the corresponding subregion from the mask image.

Second, to demonstrate the value of the method for selecting an operating point along a characteristic interval, the ideal operating point was defined as which of two options (center or right end of the interval) yielded a CPD closer to the reference vascular volume fraction for that subregion. For subregions that included a detected characteristic interval, the frequency at which the ideal operating point fell at each of the center and the right end of the interval was determined. The number of cases in which the automatically selected operating point matched the ideal operating point was determined separately for each ROI and each choice of operating point (*i.e.*, center or right end).

Third, to demonstrate the value of selecting separate operating cut-off velocities for each subregion in an ROI, the variation in the selected cut-off velocity was quantified by computing the mean, standard deviation, and range of the selected cut-off velocities for each ROI.

Finally, the fidelity of each reconstructed image was evaluated by computing its CPD and determining the percent error of the CPD from the reference vascular volume fraction. The reconstructed images were also assessed visually by comparing the sharpness and continuity of the vessels to the mask images and to the vessels depicted in power Doppler images produced using the previous version of the WFSC method [13], which selects a single cut-off velocity for the entire ROI.

2.3 Results

2.3.1 Characteristic interval detection

Characteristic intervals detected by the redesigned algorithm consistently aligned with prominent local maxima in $|\Delta\text{CPD}|_{\text{norm}}$, as illustrated in Figure 2-2. The detected intervals always included the CPD sample closest to the reference vascular volume fraction of the corresponding subregion. In the subregions that intersected the two closely spaced vessels near the middle of the high- and medium-vascularity ROIs (see the mask images in Figure 2-4), two characteristic intervals were always detected, as expected, at all of the subregion dimensions tested by the iterative algorithm. Similarly, single characteristic intervals were consistently detected in subregions containing only one vessel. In all but two cases, no characteristic intervals were detected in subregions that contained no flow according to the mask images. The two exceptions were subregions near the deepest vessel in the high vascularity ROI. Both of those spuriously detected intervals had mean CPD close to 0.001, so they contributed negligible error to the CPD of the reconstructed image.

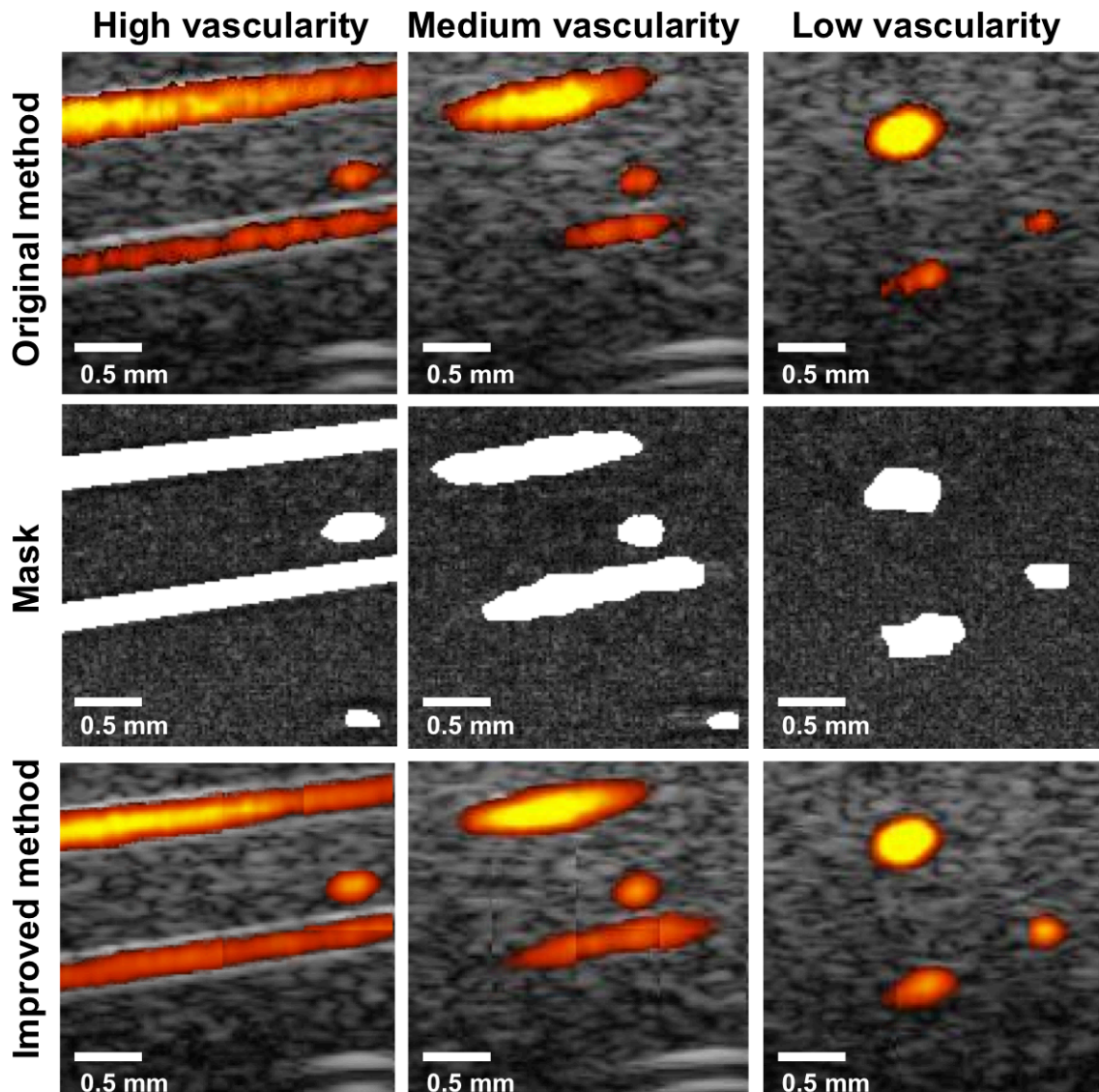


Figure 2-4: Image improvement produced by the redesigned wall filter selection curve (WFSC) method. The top row shows the images acquired using the original method where a single cut-off was selected for each ROI [13]. The middle row shows the mask images of the three ROI of the phantom. The bottom row shows the reconstructed images produced by applying the redesigned WFSC method.

2.3.2 Selection of an operating point cut-off velocity

Comparison of the cut-off velocity at the automatically selected operating point for each subregion to the ideal operating point defined in the Methods indicates that the addition of this step to the WFSC method produces a meaningful change in the results and that the automated algorithm accurately selects the ideal operating point in the majority of cases. Figure 2-5 shows that the ideal operating point corresponded to each of the middle and right end of the characteristic interval in about half of the total subregions with detected flow (e.g., the ideal operating point was at the middle of the interval in 17 out of 31 subregions). The automatically selected operating point matched the ideal operating point in 25 of 31 subregions with detected flow, for an overall accuracy of 80.6%.

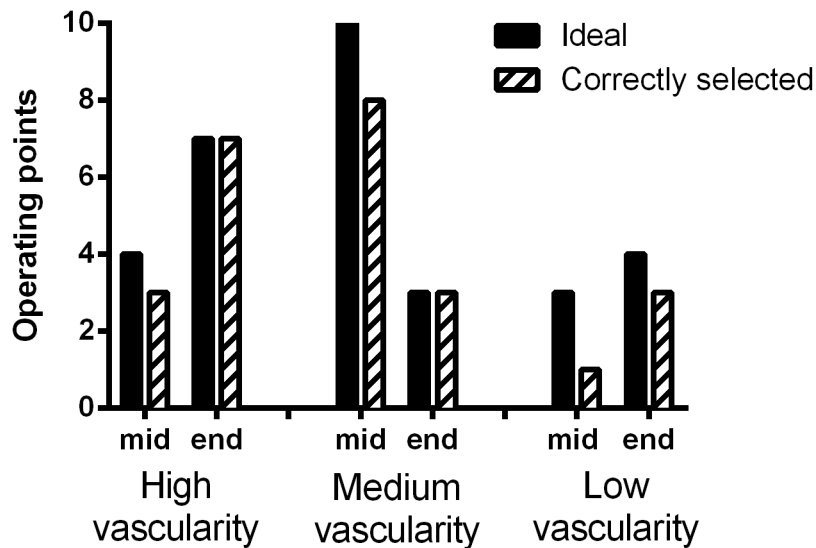


Figure 2-5: Analysis of accuracy of the selection of operating point cut-off velocity. The numbers of ideal operating points located at the middle and the right end of the detected characteristic interval are represented by the black solid bars. The number of correctly selected operating points is shown by the cross-hatched bars

The range of variation in the cut-off velocities at the selected operating points (Table 2-1) demonstrates the appropriateness of allowing the cut-off velocity to vary within the ROI. The coefficient of variation (standard deviation divided by mean) of the

selected cut-off velocities was at least 0.52 in the three ROIs studied. The greatest variation in selected cut-off velocity occurred in the low vascularity ROI.

Table 2-1: Variation of selected cut-off velocities among subregions of high, medium, and low vascularity ROIs

| Vascularity of ROI | Mean (mm/s) | Standard deviation (mm/s) | Range (mm/s) |
|--------------------|-------------|---------------------------|--------------|
| High | 3.3 | 1.75 | 1.5 - 5.0 |
| Medium | 3 | 1.57 | 1.1 - 4.5 |
| Low | 5.8 | 3.96 | 1.9 - 11.0 |

2.3.3 Reconstructed images

The redesigned WFSC method produced both qualitative and quantitative overall improvement of the power Doppler images. The vessels depicted in the reconstructed images more closely matched the mask images and had smoother boundaries compared to the images obtained using the previous version of the WFSC method (Figure 2-4). The improved vessel visualization in the images reconstructed using the redesigned method is attributed in part to the redesigned method's ability to vary the cut-off velocity to be suitable for individual vessels rather than selecting one cut-off velocity for the entire ROI. A minor drawback of varying the cut-off velocity is that a transition between adjacent subregions is occasionally visible in the reconstructed images, particularly for the lower transverse vessel in the medium vascularity ROI.

Table 2-2 summarizes the accuracy of the CPD of the reconstructed images as an estimate of the reference vascular volume fraction of the phantom. Neither the original nor the redesigned WFSC method was able to detect the deepest vessel in the high and medium vascularity ROIs. Therefore, for these images, the percentage error in the CPD of the top three vessels is the fairest measure of the method's ability to improve quantification of vessels that are detectable by the power Doppler system. This error was

less than 3% for all three ROIs. In comparison to the CPD estimates reported in [13] for the original WFSC method, the CPD values obtained for the top three vessels using the redesigned method are closer to the vascular volume fractions estimated from the mask images (see also Table 2-2).

Table 2-2: Relative accuracy of quantification of blood flow for high, medium, and low vascularity ROIs

| | Vascularity of ROI | | |
|-----------------------------------------|--------------------|--------|--------|
| | High | Medium | Low |
| Reference vascular volume fraction | 0.1944 | 0.1283 | 0.0567 |
| Original method CPD | 0.2014 | 0.0859 | 0.0407 |
| Reconstructed CPD (Top 3 vessels) | 0.1961 | 0.1295 | 0.0583 |
| Reconstructed CPD error (Top 3 vessels) | 0.90% | 0.89% | 2.76% |
| Deepest vessel CPD error | -2.35% | -3.03% | -- |
| Total CPD error | -1.45% | -2.14% | 2.76% |

2.4 Discussion

The redesigned WFSC method presented in this chapter generates power Doppler images in which the wall filter cut-off velocity can vary among subregions of the Doppler ROI. These images have minimal artifact, are qualitatively and quantitatively improved compared to images acquired at any single cut-off velocity, and therefore are considered more suitable images for vascular quantification. The redesigned method is more automated than the previous WFSC method [13] and provides better overall performance. The WFSC method was improved by enhancing its two fundamental processes, characteristic interval detection and selection of an operating point cut-off velocity.

Accurate characteristic interval detection is the foundation of the WFSC method. The interval detection algorithm was developed by trying to match the ability of a human observer to visually identify (in bar graphs like Figure 2-2) pairs of local maxima in $|\Delta\text{CPD}|_{\text{norm}}$ that bound candidate characteristic intervals. Therefore, the observation that the automatically detected characteristic intervals consistently aligned with local maxima in $|\Delta\text{CPD}|_{\text{norm}}$ is considered evidence that the algorithm functions as intended. The algorithm consistently detected two characteristic intervals in subregions traversed by two vessels. The automated algorithm produced this result without *a priori* input about the expected number of characteristic intervals and therefore should be capable of detecting more than two intervals if presented with image data for a subregion containing many vessels with different sizes and flow rates.

An important strength of the redesigned algorithm is its ability to detect characteristic intervals that would have been missed by our previous threshold-based detection method. Consider, for example, intervals A and C in Figure 2-2. In the previous version of the method, the WFSC was analyzed by computing $|\Delta\text{CPD}|/\text{CPD} = |\text{CPD}_2 - \text{CPD}_1|/\text{CPD}_1$, *i.e.*, the denominator was different from the $|\Delta\text{CPD}|_{\text{norm}}$ metric defined in Eqn 2-2. Figure 2-6 shows the WFSC from Figure 2-2 with the previous method's $|\Delta\text{CPD}|/\text{CPD}$ metric overlaid as a bar graph. The previous method identified plateaus by searching for sets of consecutive $|\Delta\text{CPD}|/\text{CPD}$ bars that fell below a predetermined threshold (which was 0.14 for flow-phantom data) and were bounded by bars that exceeded the same threshold. Although $|\Delta\text{CPD}|/\text{CPD}$ is less than the threshold along the entire length of interval C, it would not have been considered a plateau because there is no preceding $|\Delta\text{CPD}|/\text{CPD}$ value greater than the threshold. However, as shown in Figure 2-2(d), the CPD values along interval C pass through the reference vascular volume fraction of that subregion, which is evidence that the best choice of cut-off velocity does lie within interval C. The previous method was designed to search for plateaus along a WFSC, but we now consider it a more robust approach to search for distinct intervals that need not be approximately horizontal. The redesigned method is capable of detecting such intervals.

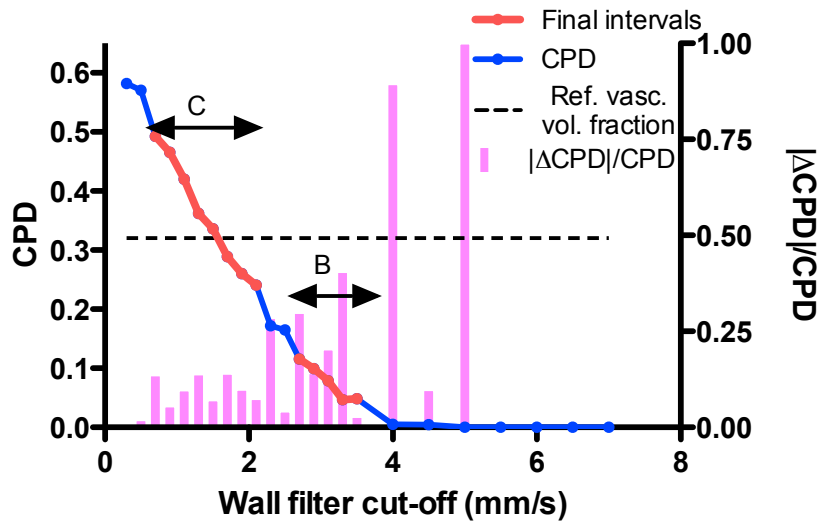


Figure 2-6: Original method for detecting characteristic intervals. The WFSC of Figure 2-2 is plotted using the blue line and left-hand y-axis. The metric used in the original method, $|\Delta\text{CPD}|_{\text{norm}}$, is shown using the violet bars and the right-hand y-axis. The final detected intervals from Figure 2-2, C and B, are highlighted in red on the WFSC. The range of cut-off velocities over which intervals C and B extend is shown using the arrows. The reference vascular volume fraction of the subregion is indicated using the horizontal dashed line. Interval C would not be detected (see discussion in text)

A justification for defining the selection of a cut-off velocity operating point as a binary decision between the velocity at the middle or right end of the characteristic interval can be made using the mathematical model from [13]. If a subregion contains only an easily detected vessel, the probability density functions (PDFs) of the vessel and background velocity estimates are widely separated and the mathematical model predicts that the WFSC will possess a long, horizontal characteristic interval. Selecting the right end of this characteristic interval minimizes false-positive color pixels in the background while retaining almost all of the true-positive color pixels within the vessel. On the other hand, a vessel that is more challenging to detect corresponds to overlapping PDFs for the vessel and background velocity estimates. In this case, selecting an operating point in the range of cut-off velocities where the PDFs overlap will yield the best possible

combination of sensitivity and specificity, *i.e.*, a point near the knee of the receiver operating characteristic for flow detection. The mathematical model predicts that this operating point will correspond to the middle of a relatively short, sloped characteristic interval. Therefore, the model suggests that the operating point should be chosen at the right end of gently sloped intervals and at the middle of more steeply sloped intervals. In the flow phantom data, subregions containing higher velocity flow, which should be readily detected, had flatter characteristic intervals, whereas subregions of slower flow, which should be more difficult to detect, had more steeply sloped intervals.

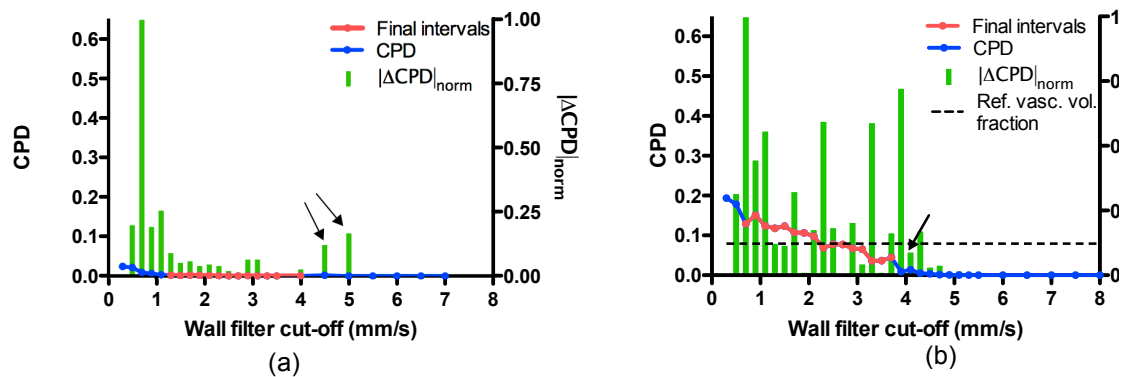


Figure 2-7: Effects of non-uniform and insufficient sampling of the wall filter selection curve (WFSC). (a) Erroneous detection of a characteristic interval in a subregion of no flow. The WFSC is shown using the blue line and left-hand y-axis. The normalized absolute first difference of the CPD, $|\Delta\text{CPD}|_{\text{norm}}$ (Eqn 2-2), is plotted using the green bars and the right-hand y-axis. The detected characteristic interval is highlighted in red. The two arrows show higher values of $|\Delta\text{CPD}|_{\text{norm}}$ caused by gaps in the sampled data, leading to false detection of a characteristic interval. (b) An example of a discrepancy between the ideal and the selected operating point cut-off velocity. The WFSC, $|\Delta\text{CPD}|_{\text{norm}}$ and the detected interval are displayed using the same format as panel (a). Only two samples are available in the portion of the selection curve following the characteristic interval (arrow). This leads to an unreliable estimate of the slope of the last portion of the curve, which causes an incorrect ranking of the slope of the characteristic interval.

The few cases where the redesigned WFSC method yielded unexpected results are attributed to non-uniform or insufficient sampling of the WFSC. In subregions where the mask image indicated that no flow was present, spurious characteristic intervals were occasionally detected at low CPD if large gaps in the sampled cut-off velocities caused large peaks in the $|\Delta\text{CPD}|_{\text{norm}}$ data (e.g., Figure 2-7(a)). Discrepancies between the ideal and automatically selected operating points, particularly in the low vascularity ROI, tended to occur when there were few samples along the WFSC (e.g., Figure 2-7(b)), which increased the uncertainty of the slope estimates for the characteristic interval and/or the other segments of the WFSC that the characteristic interval is compared with to determine its relative steepness. Therefore, the method could be further improved by developing WFSC sampling criteria to ensure images are acquired at a sufficient number of uniformly and closely spaced cut-off velocities.

This study was limited by the fact that only scan-converted image data was available for analysis, so it was not possible to retrospectively reconstruct images at additional cut-off velocities. Therefore, the results in this chapter are based on images acquired at only the highest flow rate (6000 $\mu\text{l/hr}$) used in [13] because the sets of images acquired at the lower flow rates did not include a sufficient number of uniformly spaced samples along the cut-off velocity axis to apply the redesigned method. This problem can be avoided in future studies by recording quadrature demodulated Doppler data rather than scan-converted images, which would enable each subregion to be retrospectively analyzed at any number of cut-off velocities.

Two minor difficulties identified in the reconstructed images were the occasionally visible transitions between adjacent subregions and the inability to detect the deepest vessel in the high and medium vascularity ROIs. The lower transverse vessel in the medium vascularity ROI provided an illustration of a visible transition (Figure 2-4). In this case, the WFSC method correctly selected the ideal operating point for all three subregions traversed by the vessel, but the 2.7 mm/s operating point for the subregion at the center of the vessel was much higher than the 1.4 mm/s average operating point selected at the ends of the vessel. This large difference in cut-off velocity caused the discontinuities in the reconstructed image. This problem may be prevented by

constructing more finely sampled WFSCs. Alternatively, the WFSC method could be modified to analyze overlapping rather than tiled subregions to enable the results obtained from overlapping subregions to be used to smooth the transitions between them.

It is not surprising that the deepest vessel in the high and medium vascularity ROIs was difficult to detect because that vessel contained slow flow due to its small diameter and also yielded low Doppler power due to attenuation. However, analyzing more finely sampled WFSCs may also improve the likelihood of detecting such a vessel. Finer sampling would require the WFSC to be evaluated at additional low values of the cut-off velocity, which could help the method extract a characteristic interval by increasing the number of $|\Delta\text{CPD}|_{\text{norm}}$ data points available at those low cut-off velocities. If the WFSC sampling criteria do prove capable of improving detection of challenging vessels, this capability may also improve the performance of the method for quantification of low vascularity ROIs, where a small number of false-negative color pixels can produce a significant percentage change in the CPD of a reconstructed image.

The strengths of the redesigned WFSC method are that (1) it is an uncomplicated technique that works by analyzing a quantity, CPD, that is directly relevant to vascular quantification, (2) the method is based on receiver operating characteristic statistics for blood-flow detection that make no assumption of ultrasound frequency, so it is expected to be applicable to clinical frequency as well as high-frequency systems [13], and (3) the method minimizes reliance on predetermined thresholds. The threshold of maximum $\text{CPD} < 0.80$ that is used to determine the size of the subregions is the one aspect of the method that does not meet the ideal of being entirely data dependent. The maximum CPD threshold was selected empirically by experimenting with the flow phantom data, so developing an algorithm with a more rigorous foundation to subdivide the ROI is one opportunity to further improve the WFSC method. This problem would best be approached using *in vivo* data. Analysis of *in vivo* data will also provide a more challenging test of the WFSC method due to the presence of background tissue motion, although the flow-phantom data used in this study did include some apparent background motion as a result of the swept-scan data acquisition.

The long-term goal of this research is to apply the WFSC method as a tool for real-time optimization of Doppler acquisition parameters. The algorithm was purposely designed to be uncomplicated and require minimal user input. The current offline implementation produces reconstructed images in 1-2 seconds despite the fact that no effort was invested in minimizing the computation time, so development of a real-time implementation is certainly feasible.

An online implementation of the WFSC method will yield the greatest benefit in scanners that are intended to be operated by non-specialist or time-sensitive users. Portable ultrasound scanners used to improve health-care delivery in remote and low-resource settings [21, 22] exemplify one potential application for the method. Simplified scanner controls have been identified as a critical need for portable ultrasound systems [23]. Preclinical ultrasound systems are also intended to be used by non-specialist operators (biomedical scientists in this case) and so share with portable ultrasound systems a need for simplified controls. As discussed in the Introduction, the WFSC method could be specifically valuable in longitudinal cancer studies. Since tumor vascularity can oscillate rapidly in mouse models [24], more frequent imaging sessions may provide valuable information about the dynamics of tumor angiogenesis and responses to anti-vascular therapies. We envision a synergistic use of power Doppler in preclinical (and possibly clinical) trials in which DCE-CT, DCE-MRI, or PET is used at a few checkpoints and Doppler is used to interpolate tumor vascularity measurements between those checkpoints. For power Doppler to be used for this purpose, acquisition settings such as the wall filter cut-off velocity, and hence the images themselves, must be optimized for accurate vascular quantification at each time point. The WFSC method can provide the means to perform this optimization.

2.5 Conclusion

The wall filter selection curve method is proposed for objectively and automatically selecting a wall filter cut-off velocity in a power Doppler system. This chapter presents a redesigned WFSC method that provides three key improvements. First, the redesigned method automatically detects single or multiple characteristic intervals,

which may be sloped, without using a predetermined threshold. Second, the new method selects an operating point along the detected characteristic interval in a data-dependent fashion. Finally, the cut-off velocity is adapted to local vasculature by independently applying the improved method to subregions within the Doppler ROI. The improved automation and performance of the WFSC method enhances its suitability for online implementation in a power Doppler scanner. Future online implementations of the method are expected to make it possible for non-specialist or time-sensitive operators, such as the users of portable scanners and preclinical scanners, to reproducibly acquire diagnostic-quality, quantitatively accurate Doppler images.

References

- [1] J. Folkman, "Angiogenesis: An Organizing Principle for Drug Discovery?," *Nature Reviews Drug Discovery*, vol. 6, pp. 273-286, 2007.
- [2] B. Turkbey, H. Kobayashi, M. Ogawa, *et al.*, "Imaging of Tumor Angiogenesis: Functional or Targeted?," *AJR Am J Roentgenol*, vol. 193, pp. 304-313, 2009.
- [3] J. C. Miller, H. H. Pien, D. Sahani, *et al.*, "Imaging Angiogenesis: Applications and Potential for Drug Development," *J Natl Cancer Inst*, vol. 97, pp. 172-187, 2005.
- [4] S. Gudmundsson, L. Valentin, J. Pirhonen, *et al.*, "Factors Affecting Color Doppler Energy Ultrasound Recordings in an in-Vitro Model," *Ultrasound Med Biol*, vol. 24, pp. 899-902, 1998.
- [5] N. J. Raine-Fenning, N. M. Nordin, K. V. Ramnarine, *et al.*, "Evaluation of the Effect of Machine Settings on Quantitative Three-Dimensional Power Doppler Angiography an in-Vitro Flow Phantom Experiment.," *Ultrasound Obstet Gynecol*, vol. 32, pp. 551-559, 2008.
- [6] W. P. Martins, N. J. Raine-Fenning, R. A. Ferriani, *et al.*, "Quantitative Three-Dimensional Power Doppler Angiography: A Flow-Free Phantom Experiment to Evaluate the Relationship between Color Gain, Depth and Signal Artifact," *Ultrasound Obstet Gynecol*, vol. 35, pp. 361-368, 2010.
- [7] K. Mizushige, T. Ueda, M. Yuba, *et al.*, "Dependence of Power Doppler Image on a High Pass Filter Instrumented in Ultrasound Machine," *Ultrasound Med Biol*, vol. 25, pp. 1389-1393, 1999.
- [8] C. Kargel, G. Plevnik, B. Trummer, *et al.*, "Doppler Ultrasound Systems Designed for Tumor Blood Flow Imaging," *IEEE Trans Instrum Meas*, vol. 53, pp. 524-536, 2004.
- [9] P. Winkler, K. Helmke, and M. Mahl, "Major Pitfalls in Doppler Investigations," *Pediatr Radiol*, vol. 20, pp. 304-310, 1990.
- [10] F. Yuan, Y. Chen, M. Dellian, *et al.*, "Time-Dependent Vascular Regression and Permeability Changes in Established Human Tumor Xenografts Induced by an Anti-Vascular Endothelial Growth Factor/Vascular Permeability Factor Antibody," *Proc Natl Acad Sci U S A*, vol. 93, pp. 14765-14770, 1996.

- [11] C. J. W. Breward, H. M. Byrne, and C. E. Lewis, "A Multiphase Model Describing Vascular Tumour Growth," *Bull Math Biol*, vol. 65, pp. 609-640, 2003.
- [12] S. Z. Pinter and J. C. Lacefield, "Detectability of Small Blood Vessels with High-Frequency Power Doppler and Selection of Wall Filter Cut-Off Velocity for Microvascular Imaging," *Ultrasound Med Biol*, vol. 35, pp. 1217-1228, 2009.
- [13] S. Z. Pinter and J. C. Lacefield, "Objective Selection of High-Frequency Power Doppler Wall Filter Cutoff Velocity for Regions of Interest Containing Multiple Small Vessels," *IEEE Trans Med Imaging*, vol. 29, pp. 1124-1139, 2010.
- [14] L. Y. L. Mo and R. M. Kulakowski, "Method and Apparatus for Adaptive Wall Filtering in Spectral Doppler Ultrasound Imaging," United States Patent US6296612 B1, 2001.
- [15] L. Y. L. Mo, C.-H. Chou, T.-L. Ji, *et al.*, "System and Method for Adaptive Clutter Filtering in Ultrasound Color Flow Imaging," United States Patent US6733455 B2, 2004.
- [16] T. Y. Kim, "Clutter Signal Filtering in an Ultrasound System," United States Patent US8313435 B2, 2009.
- [17] C.-Y. Lee, D. Freiburger, and M. G. Magrane, "Automatic Optimization in Spectral Doppler Ultrasound Imaging," United States Patent US7578792 B2, 2009.
- [18] M. D. Judd, "A Simple, Low-Computation Peak Detection Algorithm for the Angle-of-Arrival Spectrum for Signal Subspace Methods," *IEEE Trans. Aerosp. and Electron. Syst.*, vol. 28, 1992.
- [19] M. M. Bakircioglu, R. W. Steins, and C. Simopoulos, "Automatic Optimization for Ultrasound Medical Imaging," United States Patent US7846098 B2, 2007.
- [20] VisualSonics, *Visualsonics White Paper- Linearizing Contrast Mode Video Data on the Vevo 770 High-Frequency Ultrasound Imaging System*: Visual Sonics, 2007.
- [21] R. D. Harris and W. M. Marks, "Compact Ultrasound for Improving Maternal and Perinatal Care in Low-Resource Settings: Review of the Potential Benefits, Implementation Challenges, and Public Health Issues," *J Ultrasound Med*, vol. 28, pp. 1067-1076, 2009.
- [22] B. P. Nelson, J. Melnick Er Fau - Li, and J. Li, "Portable Ultrasound for Remote Environments, Part Ii: Current Indications," *J Emerg Med*, vol. 40, pp. 313-321, 2009.

- [23] B. P. Nelson, J. Melnick Er Fau - Li, and J. Li, "Portable Ultrasound for Remote Environments, Part I: Feasibility of Field Deployment," *J Emerg Med*, vol. 40, pp. 190-197, 2009.
- [24] J. W. Xuan, M. Bygrave, H. Jiang, *et al.*, "Functional Neoangiogenesis Imaging of Genetically Engineered Mouse Prostate Cancer Using Three-Dimensional Power Doppler Ultrasound," *Cancer Res*, vol. 67, pp. 2830-2839, 2007.

Chapter 3

A new three-component signal model to objectively select power Doppler wall filter cut-off velocity for quantitative microvascular imaging

The content of this chapter has been adapted from: "A new three-component signal model to objectively select power Doppler wall filter cut-off velocity for quantitative microvascular imaging," published in, Proc. SPIE, vol.8670, article 86750J 2013, by M. Elfarnawany and J. C. Lacefield.

3.1 Introduction

Power Doppler ultrasound is a noninvasive, economical approach to microvascular imaging, but use of Doppler for quantitative applications such as evaluating treatment responses in oncology trials is often discouraged due to the operator dependence of the images [1]. As reviewed in [2], operator dependence is a consequence of the sensitivity of the images to user selected acquisition parameters such as gain, pulse repetition frequency, and wall filter cut-off velocity. The wall filter selection curve (WFSC) method [2-4] has been proposed to address this problem. The WFSC method has been shown to be effective for objective selection of wall filter cut-off velocity in high-frequency (30 MHz) power Doppler images of flow phantoms containing 200-300 μm diameter vessels. In the WFSC method, a set of power Doppler images is acquired over a range of values for the cut-off velocity. The color pixel density (CPD, equal to the fraction of pixels with detected flow) is computed within matching regions of interest (ROI) in each image and plotted as a function of the cut-off velocity. The resulting curve

(e.g., Figure 3-1) possesses a distinct “characteristic interval” that can be used to select an operating point cut-off velocity at which the CPD provides an accurate estimate of the vascular volume fraction in the region of interest.

An uncomplicated mathematical model was proposed in [4] to describe the mathematical basis of the WFSC method. In the original model, power Doppler imaging is treated as a signal detection task in which color pixels are obtained from two sample populations, true-positive pixels within vessels and false-positive pixels in the tissue background. For a region of interest containing a single vessel, the CPD can be expressed as a function of the cut-off velocity:

$$CPD(v_c) = F_v TPF(v_c) + [1 - F_v] FPF(v_c) \quad \text{Eqn. 3-1}$$

where v_c is the wall filter cut-off velocity, $TPF(v_c)$ and $FPF(v_c)$ are the true- and false-positive fractions obtained as the cut-off velocity is varied, and F_v is the vascular volume fraction within the ROI. As detailed in [4], a closed-form version of Eqn. 3-1 can be obtained by assuming the probability density function (PDF) of the Doppler velocity estimates for the extravascular pixels is characterized by a zero-mean Gaussian distribution with a specified variance. The color pixel FPF as a function of cut-off velocity is then given by the area under the extravascular PDF from $-\infty$ to $-v_c$ plus the area under the PDF from v_c to ∞ . The color pixel TPF is obtained similarly, except the PDF of intravascular Doppler velocity estimates is assumed to possess a non-zero mean and a potentially different variance. Evaluation of Eqn. 3-1 over a range of values for the underlying parameters demonstrated that the cut-off velocity selected by the WFSC method can be expected to yield an accurate estimate of the vascular volume fraction only if the characteristic interval is longer than an identifiable minimum length and begins at a cut-off velocity less than an identifiable minimum velocity [4]. These insights from the mathematical model proved valuable to the initial development of the WFSC method.

However, a few shortcomings of the original mathematical model emerged during subsequent development of the WFSC method [2]. The most important of these is that, although the model in [4] predicts that characteristic intervals should usually be horizontal or nearly so, sloped characteristic intervals are frequently observed even in the relatively idealized context of flow-phantom images. A second shortcoming is that the original mathematical model did not always provide an accurate fit to the segment of the WFSC at cut-off velocities beyond the right end of the characteristic interval. This detail is relevant because the shape of the WFSC as the CPD rolls off to zero affects the performance of the current algorithm [2] for detecting a characteristic interval. Therefore, the objective of this chapter is to propose and demonstrate modifications to the mathematical model that address these inaccuracies.

Our primary motivation for improving the mathematical model is to obtain a conceptual tool that will be useful for designing an online implementation of the WFSC method. This application is used to demonstrate the revised model in the following sections. However, the model also presents a more broadly useful perspective for understanding and characterizing the performance of power Doppler imaging. Although power Doppler is commonly used, most studies of factors affecting the performance of power Doppler have involved time-consuming flow-phantom experiments. The most sophisticated theoretical analysis of power Doppler led to an ideal observer model that provides an upper bound on flow-detection performance [5-7]. These papers presented simulations and flow-phantom studies that were analyzed using signal-detection parameters that are difficult to directly relate to the accuracy of vascular quantification and difficult to interpret for the purpose of guiding the operator's selection of image acquisition parameters. Our mathematical model of the WFSC method approaches the same signal detection problem from a more empirical perspective that is intended to be straightforward for other Doppler researchers to adopt and apply to their own image data.

The following sections introduce an improved three-component mathematical model that is obtained by separating the background pixels into a perivascular population and an extravascular population. The inclusion of a perivascular image component is motivated by our observation in flow-phantom images that color pixels just outside the

vessels are the last false-positive pixels to be eliminated as the cut-off velocity is increased [4]. In addition, a cost function is defined that weighs the positive utility of true-positive (intravascular) color pixels against differing penalties for perivascular color pixels, which have a relatively modest impact on vessel visualization, and extravascular color pixels. The cost function incorporates into the analysis the concept that the cut-off velocity that best visualizes the vascular architecture may not be the cut-off velocity that yields a CPD exactly equal to the actual vascular volume fraction. Finally, the usefulness of the three-component model is demonstrated by using the model and cost function to: (1) determine the number of cut-off velocities at which a WFSC should be sampled to ensure the automated algorithm of [2] yields accurate results, (2) evaluate the sensitivity of the WFSC method to frame-to-frame variation in CPD, which is expected to be greater during *in vivo* imaging than in flow-phantom images, and (3) assess the potential value of developing a more complicated algorithm for selecting an operating point cut-off velocity in comparison to the current WFSC method, which is constrained to a binary decision between operating points at the middle and right end of the characteristic interval [2].

3.2 Materials and Methods

3.2.1 Revised Mathematical Model

Two modifications are proposed to our original two-component mathematical model presented in [4]. First, a third, perivascular, Gaussian distributed signal component is added to represent the effect of the Doppler artifacts that cause the appearance of color pixels in the perivascular tissue immediately surrounding a vessel. These artifacts are caused by turbulent flow, reverberations, or too high gain settings [8, 9]. Second, a log-normal distribution is now assumed for the first-order statistics of the intravascular signal component because log-normal statistics more accurately correspond to the distribution of flow velocities in a region of interest containing a network of vessels [10]. The revised model has the form:

$$CPD(v_c) = F_v ICPF(v_c) + wF_v PCPF(v_c) + [1 - (1 + w)F_v] ECPF(v_c) \quad \text{Eqn. 3-2}$$

where v_c is the wall filter cut-off velocity, F_v is the vascular volume fraction of the vessel(s) within the region of interest (ROI), w is a weight parameter used to define the volume fraction of the perivascular compartment, and $ICPF(v_c)$, $PCPF(v_c)$, and $ECPF(v_c)$ are the color pixel fractions in the intravascular, perivascular, and extravascular compartments, respectively, as functions of v_c . The volume fraction of the perivascular compartment is defined as a fraction of the vascular volume fraction, F_v , since it was shown by [8, 9] that the perivascular artifacts are function of the vessel diameter, flow, and orientation.

The $ICPF$, $PCPF$, and $ECPF$ terms in Eqn. 3-2 are evaluated as described in [4] by assuming an analytical form for the probability density function of the Doppler velocity estimates in each compartment and using the corresponding cumulative density function to compute the proportion of velocity estimates in each compartment that are greater than v_c . In the intravascular compartment, where the Doppler velocity estimates are assumed to be log normally distributed, the natural logarithm of the velocity estimates is therefore normally distributed, so $ICPF(v_c)$ can be computed using the standard-normal cumulative density function as described in [11]:

$$ICPF(v_c) = 1 - \phi\left(\frac{\ln(v_c) - \mu_{ln}}{\sigma_{ln}}\right), \quad \text{Eqn. 3-3(a)}$$

$$\mu_{ln} = \ln\left(\frac{\mu_i^2}{\sqrt{\sigma_i^2 + \mu_i^2}}\right), \quad \sigma_{ln} = \sqrt{\ln\left(\frac{\sigma_i^2}{\mu_i^2} + 1\right)}, \quad \text{Eqns. 3-3(b-c)}$$

In Eqns. 3-3, ϕ is the standard-normal cumulative density function, $v_c \geq 0$, μ_{ln} and σ_{ln} are the mean and standard deviation of the natural logarithm of the Doppler velocity estimates, and μ_i and σ_i are the mean and standard deviation of the log-normally distributed velocity estimates for the intravascular pixels.

Mean velocity estimates in the three compartments are chosen such that, as v_c is increased from zero, extravascular color pixels are preferentially eliminated at lower cut-offs than perivascular color pixels, which are in turn preferentially eliminated at lower cut-offs than intravascular color pixels. The velocity estimates in the extravascular pixels

were assumed to be zero mean as in [4], while the mean velocity estimate in the perivascular compartment was set to the average of the intra- and extravascular mean velocity estimates. Therefore, the equations for the color pixel fractions in the perivascular and extravascular compartments are:

$$PCPF(v_c) = 1 + \phi\left(\frac{-v_c - \mu_i/2}{\sigma_p}\right) - \phi\left(\frac{v_c - \mu_i/2}{\sigma_p}\right), \quad \text{Eqn. 3-4}$$

$$ECPF(v_c) = 2\phi\left(\frac{-v_c}{\sigma_e}\right), \quad \text{Eqn. 3-5}$$

where σ_p and σ_e are the standard deviations of velocity estimates for the perivascular and extravascular pixels, respectively.

The three-component mathematical model (Eqn. 3-2) was manually fit to 20 wall-filter selection curves generated from the single-vessel ROIs [4] or selected subregions of ROIs [2] in the flow phantom data by adjusting the parameters μ_i , σ_i , σ_p , and σ_e . For each ROI or subregion, the vascular volume fraction, F_v , was set to the reference value obtained from manually segmented B-mode images of that ROI or subregion in the phantom [2, 4]. An F-test was used to compare the goodness of fit of the three-component model and the original two-component model [4] to each of the 20 experimental WFSCs. Secondly, to validate the assumption of log-normally distributed velocity estimates in the intravascular pixels, a t-test was used to compare the sum-of-squares of the error in fitting the proposed three-component model to the error in fitting an all-Gaussian three component model with identical values for the means and standard deviations of the Doppler velocity estimates.

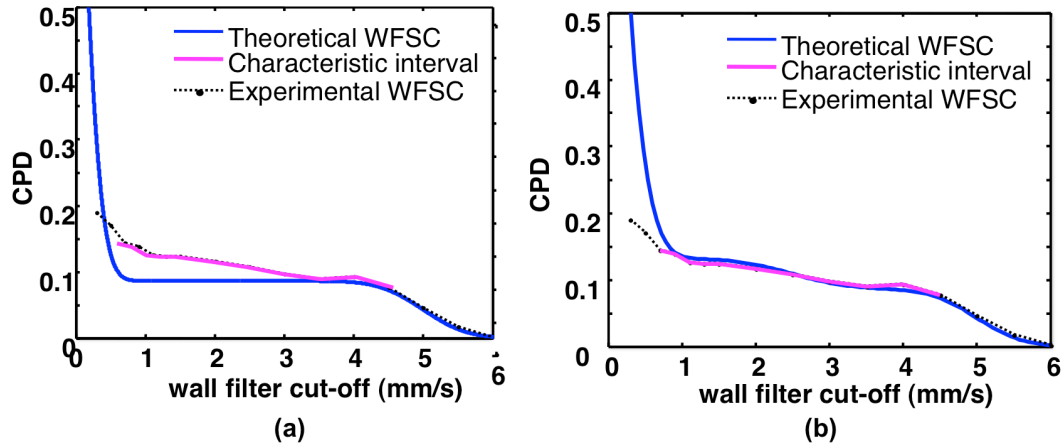


Figure 3-1: Theoretical wall filter selection curves (blue lines) fitted to experimental multiple-vessel flow-phantom data (dotted black lines) using: (a) original 2-component model (Eqn. 3-1) and (b) new 3-component model (Eqn. 3-2). The detected characteristic intervals are highlighted in violet. The 3-component model fits the sloped interval in the flow-phantom WFSC significantly better than the 2-component model.

3.2.2 Cost Function

The cost function used to define the optimum cut-off velocity along a characteristic interval of a synthetic WFSC is given by:

$$Cost(v_c) = F_v U_{IFN} IFNF(v_c) + w F_v U_{PCP} PCPF(v_c) + [1 - (1 + w) F_v] U_{ECP} ECPF(v_c) \quad \text{Eqn. 3-6}$$

where $IFNF(v_c) = 1 - ICPF(v_c)$ is the false-negative fraction in the intravascular compartment, U_{IFN} , U_{PCP} , and U_{ECP} are the utilities of the intravascular false-negative color pixels, perivascular false-positive color pixels, and extravascular false-positive color pixels, respectively. In the following simulations, the utilities U_{IFN} , U_{PCP} , and U_{ECP} are set to 2, 1, and 2, respectively, to model our assumption that false-positive color pixels in the perivascular compartment are less detrimental to image interpretation than false-negative color pixels in the intravascular compartment or false-positive color pixels in the extravascular compartment. The cost function is evaluated for v_c within the

characteristic interval of the corresponding WFSC only and the optimum cut-off velocity is defined as the v_c yielding the minimum cost along the characteristic interval. A sample cost function is shown in Figure 3-2.

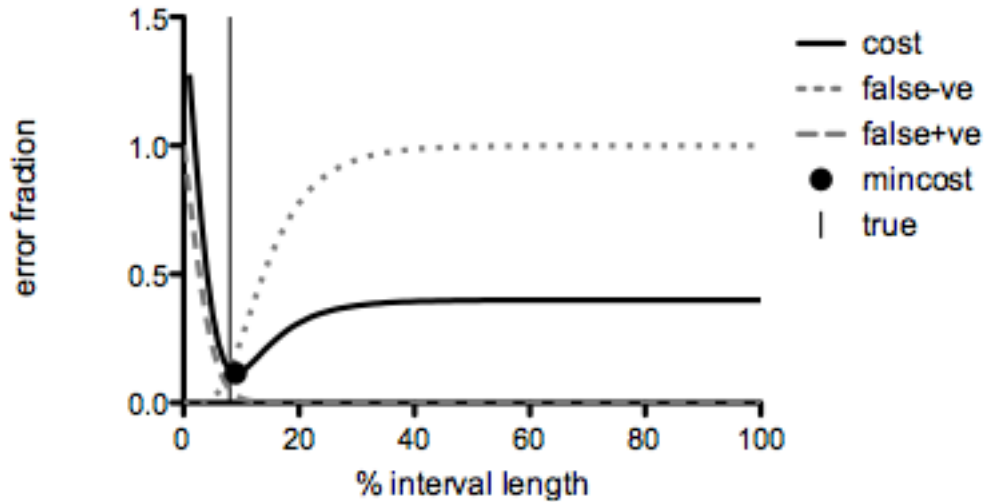


Figure 3-2: A sample cost function (solid line) is produced from a weighted combination of false-positive (dashed line) and false-negative (dotted line) error fraction along a detected interval. The relative position along the interval was represented as a percentage of the interval length, where 0% corresponded to the left end of the interval and 100% corresponded to the right end. In this example, the point of minimum cost (solid circle) matches the point corresponding to the true cut-off velocity (vertical line) along the interval.

3.2.3 Generation of Simulated WFSCs and Cost Functions

Theoretical wall-filter selection curves and their corresponding cost functions were generated in Matlab 7 (The MathWorks, Natick, MA) by evaluating Eqns. (3-2) and (3-6) for $v_c = 0$ to 18 mm/s for many different combinations of μ_i , σ_i , σ_p , σ_e , F_v , and w as specified in Table 3-1. The ranges of variation for σ_i , σ_p , and σ_e , were chosen to match the ranges of values needed to fit the three-component model to WFSCs of single vessel ROIs and subregions of ROIs as explained in Sec. 3.2.1, thereby approximating the characteristics of the curves obtained from flow-phantom data. The range of F_v included the high vascular volume fractions observed within small subregions of the Doppler ROI

[2]. The lower bound on the value of μ_i , 2.8 mm/s, was chosen to be within the 2-10 mm/s blood flow velocity range expected in tumor arterioles of 20-120 μm diameter. The 2-10 mm/s velocity range was estimated based on an experimental study showing that blood flow velocities in normal tissue arterioles of 20-120 μm diameter range between 20 and 100 mm/s [12] and the observation that blood velocities in tumor microvessels are typically an order of magnitude less than in normal vessels[13].

For each simulation, trials were excluded from further processing if $PCPF$ was greater than or equal to 20 times $ICPF$ at a low cut-off velocity of $\mu_i/4$. In these cases, the number of perivascular color pixels ($w F_v PCPF$) is greater than or equal to the number of intravascular color pixels ($F_v ICPF$) at the minimum value of $w = 5\%$. This condition was assumed to represent an unrealistically high number of perivascular color pixel artifacts. Upon applying this condition, each simulation included approximately 2080 trials testing different combinations of the model parameters.

Table 3-1: Ranges of variation of vascular parameters for the numerical analysis

| Parameter | Range simulated |
|------------|------------------|
| μ_i | 2.80 – 8.00 mm/s |
| σ_i | 0.15 – 4.00 mm/s |
| σ_p | 0.15 – 2.00 mm/s |
| σ_e | 0.15 – 1.00 mm/s |
| F_v | 0.20 – 0.80 |
| w | 0.05 – 0.20 |

3.2.4 Performance Analysis of the WFSC Method

3.2.4.1 Sensitivity to number of cut-off velocity samples

To investigate the effect of the number of cut-off velocity samples on the performance of the WFSC method, synthetic WFSC data were produced by sampling the theoretical WFSC curve (Eqn. 3-2) at equal intervals from 10 to 200 samples in

increments of 10 samples for $v_c = 0$ to 18 mm/s. Highly oversampled curves containing 1000 samples were also produced. Each sampled curve was processed using the automatic WFSC algorithm [2] to determine the locations along the v_c axis of the beginning and end of the characteristic interval. For each of the sampled curves, two characteristic interval detection errors were defined as the differences between the cut-off velocities at the start and end of the detected intervals and their corresponding cut-off velocities for curves of 1000 samples. The mean interval detection error over the 2080 curves times 2 errors/curve was plotted as a function of the number of samples. The minimum sufficient number of samples was identified as the first point at which the mean error curve changes its slope from negative to positive, at which point the curve has approximately converged to a steady error value.

3.2.4.2 Sensitivity to frame-to-frame variability of color pixel density

To investigate the sensitivity of the WFSC method to variability in CPD, we define the color pixel signal-to-noise ratio ($cpSNR$) as the ratio of the mean CPD at a point along a WFSC to the standard deviation of the CPD when a sequence of frames are acquired with all conditions held constant. In the following simulations, we used the error in fitting Eqn. 3-2 to the 20 experimental flow-phantom WFSCs from [2, 4] to compute a reference $cpSNR$. The mean value of $cpSNR$ for the 20 experimental WFSCs was designated $(cpSNR)_{phantom}$.

Synthetic WFSCs were produced using the minimum sufficient number of samples identified in the previous simulations. Synthetic color pixel noise was added to each sample as a zero-mean Gaussian random variable with $\sigma = m (CPD(v_c) / (cpSNR)_{phantom})$ for integer $m \geq 1$. For each value of m , the relative vascular quantification error was computed as the mean difference between the CPD at the cut-off velocity selected by our automated WFSC method [2] and the CPD at the optimum cut-off velocity defined by the cost function divided by the CPD at the optimum cut-off. Simulations were repeated for increasing m to search for the threshold in $cpSNR = (cpSNR)_{phantom} / m$ at which the mean vascular quantification error exceeds 5%. The 5% error goal was chosen to maintain the performance of the automated WFSC method [2] within no worse than half of the 10% error achieved by the original WFSC method [4].

3.2.4.3 Comparison of methods for selecting the operating cut-off velocity

We computed and compared the relative vascular quantification errors achieved when using four different methods for selecting the operating cut-off velocity. The first method, referred to as *closest*, selects the sampled cut-off velocity closest to the optimum cut-off velocity defined by the cost function. The second selection method, which represents an idealized version of our automated WFSC method [2], was a *perfect binary* decision (*i.e.*, whichever of the middle or end points of the characteristic interval is closest to the optimum cut-off). The vascular quantification errors using these two methods were compared using the two one-sided test (TOST) procedure presented by Schuirmann [14]. The TOST is the most basic form of equivalence testing used to establish that the means of two data sets differ by less than a user selected tolerance. In a TOST, two one-sided t-tests are applied on user-defined lower (negative) and upper (positive) bounds on the difference in means. The two tests yield two p-values of which the greatest is taken as the p-value of the equivalence test. In this chapter, the user-defined “equivalence interval” [14] was set to $[-2.5, 2.5]$ to allow for a variation equal to the 5% error goal.

In some simulated cases, we observed that the optimum cut-off velocity was located towards the beginning (*i.e.*, the left end) of the characteristic interval. Therefore, the third selection method considered was a *perfect ternary* decision that chooses whichever of the beginning, middle, or end points of the characteristic interval is closest to the optimum cut-off velocity. The vascular quantification error of a perfect ternary decision was compared to the vascular quantification error of a perfect binary decision using the TOST procedure.

The vascular quantification error using the fourth selection method, our previously published *automatic algorithm* [2], was computed and compared to the error using the perfect binary decision method using a TOST procedure. In addition, the correspondence between cut-off velocities selected using the automatic and perfect binary methods was evaluated by determining the number of cases in which both methods selected the middle of the characteristic interval, the number of cases in which both

methods selected the end of characteristic interval, and the number of cases in which the two methods selected different operating points. Finally, to evaluate the accuracy of the automatic algorithm at different vascular volume fractions, the vascular quantification error was plotted as a function of the CPD value at the optimum cut-off velocity.

3.2.4.4 Properties of reliable characteristic intervals

The previous WFSC simulations reported in [4] showed that the characteristic interval length and the minimum cut-off velocity along the interval are correlated with the accuracy of the CPD as an estimate of the vascular volume fraction. It was concluded in [4] that selection curves with intervals shorter than 2.0 mm/s or with intervals that begin at high cut-off velocities (> 2.0 mm/s) provide unreliable estimates of vascular volume fractions. Therefore, the original WFSC method was not recommended to be used if these conditions are not satisfied. To revisit these recommendations for the improved WFSC method presented in [2], a similar analysis was performed in which the vascular quantification error for all 2080 simulated WFSCs was plotted as a function of the interval length and interval minimum cut-off velocity. The vascular quantification error was computed as the difference between the CPD at the optimum cut-off velocity and the automatically selected cut-off velocity. Using these curves, we defined the minimum detectable interval length, the minimum interval length for reliable quantification (the interval length at which the quantification error is below the 5% target error), and the threshold for the starting cut-off velocity of an interval. The analysis was performed for theoretical WFSCs with no color pixel noise and synthetic WFSCs with the minimum acceptable $cpSNR$ determined in Section. 3.2.4.2.

3.3 Results

3.3.1 Revised Mathematical Model

The introduction of the perivascular signal component visually improved the ability of the model to fit flow-phantom WFSC data with sloped characteristic intervals, as shown in Figure 3-1. The F test indicated that the three-component model fits the flow-phantom WFSC data significantly better than our previous two-component model ($p < 0.005$). Similarly, using a log-normal distribution for the Doppler velocity estimates in

the intravascular compartment provided a better fit to the roll-off portion of the WFSC, as shown in Figure 3-1, compared to the all-Gaussian three-component model. The t-test showed that the means of the sum-of-squares errors using the proposed three-component model and the all-Gaussian three-component model were not significantly different ($p > 0.05$).

3.3.2 Performance Analysis of the WFSC Method

3.3.2.1 Sensitivity to number of cut-off velocity samples

The mean interval detection error continuously decreased as the number of samples used to generate the WFSC increased (Figure 3-3). The error started to stabilize between 90 and 100 samples; therefore, wall-filter selection curves should be sampled using at least 100 cut-off velocities to ensure robust performance of the WFSC method.

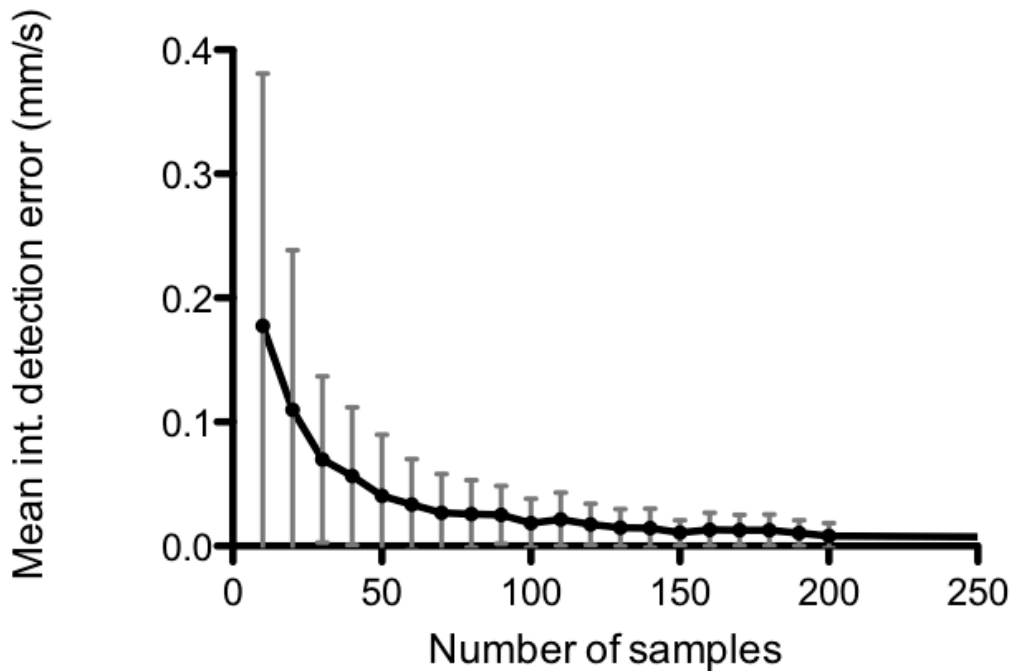


Figure 3-3: The mean interval detection error (solid line) plotted as a function of the number of samples. Standard deviation of the error is represented by the bars. The minimum sufficient number of samples was identified as the first point at which the mean error curve changes its slope from negative to positive.

3.3.2.2 Sensitivity to frame-to-frame variability of color pixel density

The value of $cpSNR_{\text{phantom}}$ computed from the flow-phantom image data was 74. The relative vascular quantification error was $3.00 \pm 5.13\%$, $4.59 \pm 7.52\%$ and $6.22 \pm 11.69\%$ for $m = 0$, $m = 1$, and $m = 2$, respectively, where increasing m corresponded to increasing CPD variability. The vascular quantification error exceeded the target 5% for $m \geq 2$, making the minimum acceptable $cpSNR$ equal to approximately 37.

3.3.2.3 Comparison of methods for selecting the operating cut-off velocity

The vascular quantification errors using the closest ($1.28 \pm 2.85\%$) and the perfect binary ($1.54 \pm 2.96\%$) selection methods were equivalent ($p < 0.0001$) according to the TOST procedure. The vascular quantification errors of the perfect binary and perfect ternary ($1.649 \pm 3.078\%$) methods were also equivalent ($p < 0.0001$). These results indicate that limiting the cut-off velocity selection to a binary choice between the middle and right end of the characteristic interval is sufficient for accurate vascular quantification. The vascular quantification errors using the automatic algorithm ($3.00 \pm 5.13\%$) and the perfect binary selection method were also statistically equivalent ($p < 0.0001$), so investment of additional effort toward development of the automated algorithm is not expected to improve the vascular quantification accuracy of the WFSC method.

The pie chart shown in Figure 3-4 summarizes the correspondence between operating cut-off velocities selected using the automatic algorithm and to the perfect binary selection method. Among the 1458 cases in which the ideal (perfect binary) selection was at the right end of the characteristic interval, the automatic algorithm selected the correct operating point with 73.8% accuracy (1076 of 1458 cases). Similarly, the automatic algorithm selected the correct operating point for 87.2% of the 627 cases in which the perfect binary method selected the middle of the characteristic interval. Therefore, the automatic algorithm selected in the correct operating point in 77.8% of the

overall cases. Note also that the perfect binary method selected the right end of the characteristic interval in almost 70% of the simulated cases.

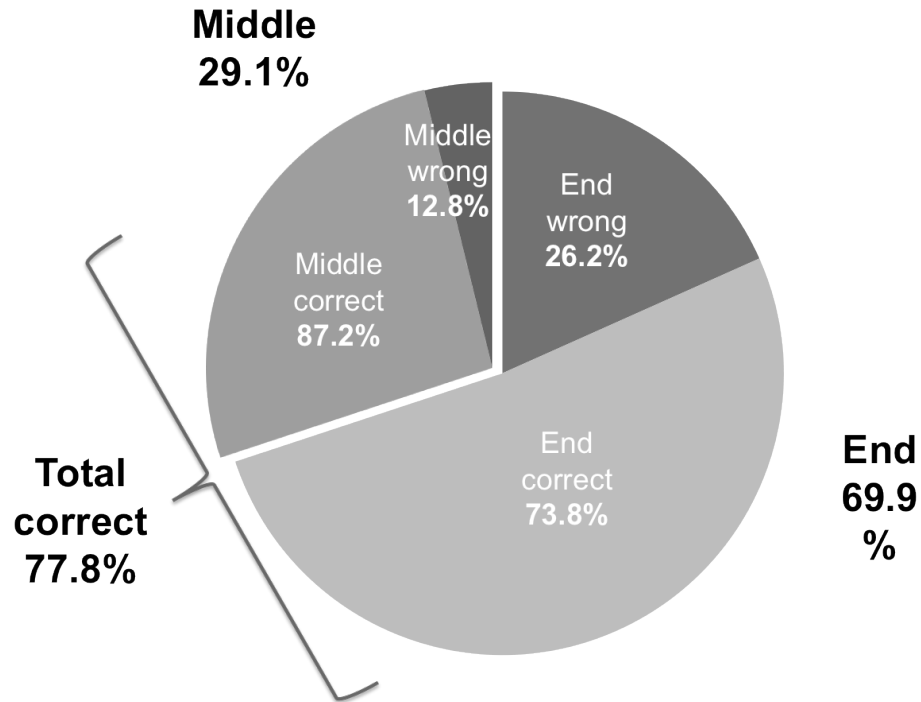


Figure 3-4: The correspondence between operating cut-off velocity selections using the automatic algorithm and the perfect binary selection method. Light gray regions show matching selections while dark region correspond to different selections. Combined correct selections represent 78% of analyzed cases.

The relative vascular quantification error using the automatic algorithm decreases as the CPD increases (Figure 3-5). In addition, the CPD at the minimum of the cost function clusters around the true vascular volume fraction, F_v , which supports using the cost function to define the optimum cut-off velocity in these simulations. However, note that the variance of the CPD at the optimum cut-off velocity from the true F_v value increases as F_v increases, as shown by the spread of the points along the x-axis in Figure 3-5.

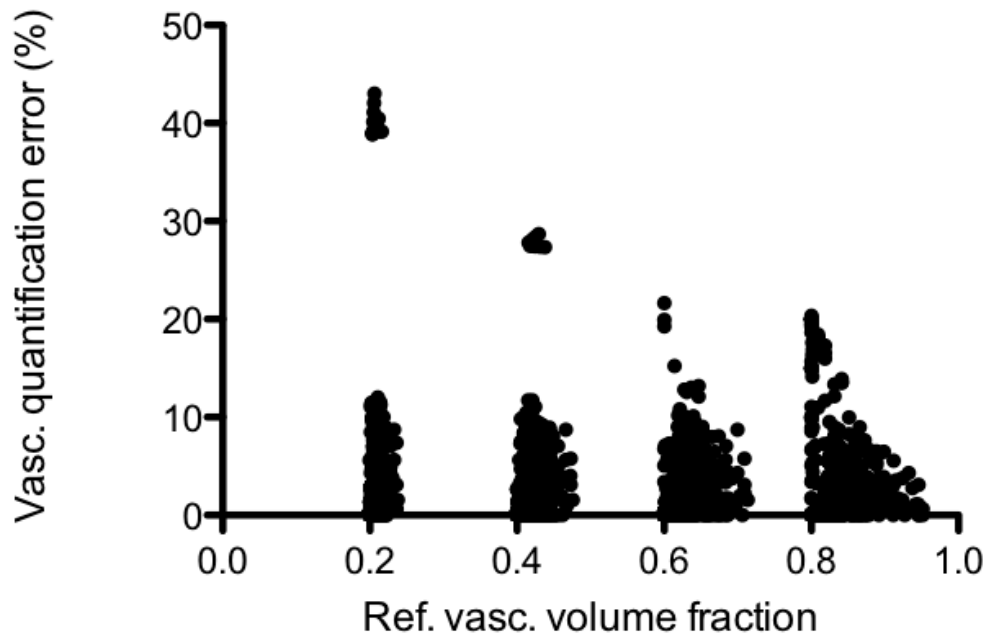


Figure 3-5: The relative vascular quantification error using the automatic algorithm as a function of the CPD value at the optimum cut-off velocity. The minimum of the cost function clusters around the reference vascular volume fraction, F_v . The spread of the points along the x-axis show that the variance of the CPD at the optimum cut-off velocity from the true F_v value increases as F_v increases.

3.3.2.4 Properties of reliable characteristic intervals

The relationship between the quantification error and characteristic interval length is shown in Figure 3-6. For both noise-free and noise-added (at $m=1$) simulations, the quantification error decreases with increasing interval length. With the limited resolution provided by the 100 samples used to construct the simulated selection curves, the minimum detectable interval length for both cases is 1.069 mm/s. However, there were few cases of longer characteristic intervals (7.485 mm/s) in the noise-added simulation compared to the maximum interval length in the noise-free simulation of 7.307 mm/s. The minimum interval length for reliable quantification was 4.10 mm/s for noise-free simulation while an interval of 6.06 mm/s in length is required to satisfy the condition of reliable quantification in a noise-added signal.

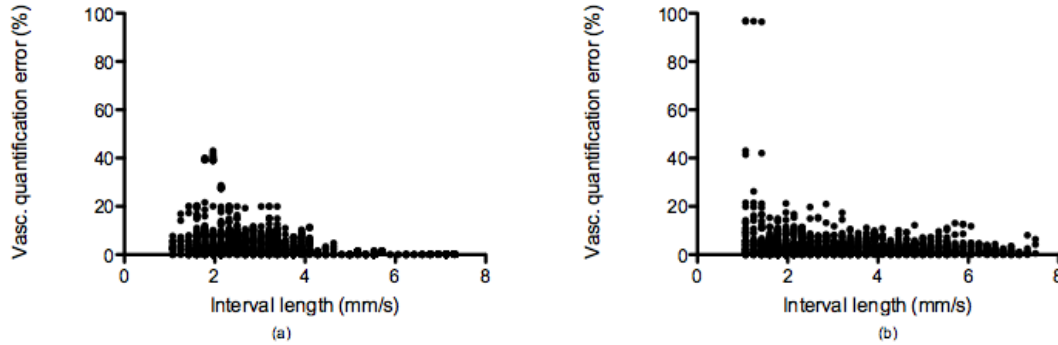


Figure 3-6: Theoretical distribution of the vascular quantification error as a function of the interval length for: (a) noise-free and (b) noise-added simulations obtained from simulations of 2080 different combinations of the parameters listed in Table 3-1. The outcome of each simulation is shown as a separate data point.

Figure 3-7 illustrates the sensitivity of the quantification error to the location of detected interval's minimum cut-off velocity and to noise. Unlike results from previous analysis in [4], the quantification error appeared to be independent of the starting cut-off velocity of a detected interval in the noise-free simulation (Figure 3-7(a)). However, adding noise to the simulations resulted in a clearer relationship between the quantification error and the minimum cut-off velocity in detected intervals. The error decreases as characteristic intervals started at higher cut-off velocities up to a certain point (3 mm/s), as shown in Figure 3-7(b), after which the error was inconsistently very high or very low. It was also noted that noise-free simulations did not exhibit any intervals starting at cut-off velocities higher than 2.86 mm/s while intervals started at up to approximately 7 mm/s upon adding the noise-signal. Therefore, the threshold for the starting cut-off velocity of an interval is set to 3 mm/s for the more realistic case of existing noise.

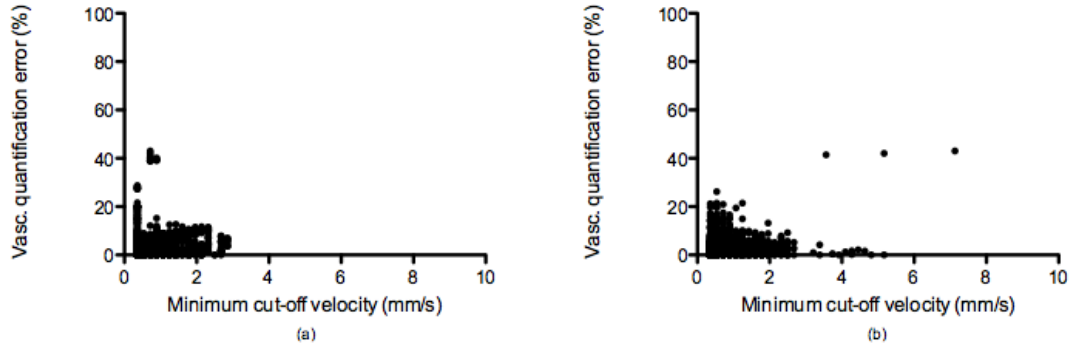


Figure 3-7: Theoretical distribution of the vascular quantification error as a function of the minimum cut-off velocity for: (a) noise-free and (b) noise-added simulations obtained from simulations of 2080 different combinations of the parameters listed in Table 3-1. The outcome of each simulation is shown as a separate data point.

3.4 Discussion

The purpose of this work is to improve our WFSC model to produce more realistic synthetic data that will be used to guide the design of an online implementation. An online implementation of the WFSC method that is sufficiently robust for application to *in vivo* imaging, will yield the greatest benefit in scanners that are intended to be operated by non-specialist or time-sensitive users. In this chapter, we combined simulations using the revised mathematical model and the reference cut-off velocity provided by the cost function to elucidate relationships between flow detection performance and a set of different parameters (such as: number of samples in a selection curve, signal-to-noise ratio, operating cut-off selection method, and interval length and location). Understanding these relationships helped define the conditions necessary to ensure effective performance of an online implementation of the WFSC method.

The key finding of this study is that addition of a third, perivascular image component to the mathematical model of the WFSC significantly improves the ability of the model to fit sloped characteristic intervals (Figure 3-1). The assumption of a log-normal distribution for the intravascular Doppler velocity estimates also contributes to

the improved ability of the model to fit WFSC data obtained from flow-phantom images. However, similar to the original model fits in [4], the revised model was not able to accurately reproduce the first portion of the selection curves at which the model generally started at a higher CPD value and was of a higher slope than the corresponding portion in experimental curves. We believe that this discrepancy is caused by some additional processing steps that are applied by the imaging system at very low cut-off velocities (such as the priority processing for image display). Since this portion of the selection curve is not part of the characteristic interval, it was not included in the revised model for simplification. Therefore, the three-component model maintains the conceptual simplicity of our original two-component model, i.e., that color flow imaging can be understood as the task of discriminating between pixels from a limited number of populations.

The number of cut-off-velocity samples in selection curves represents the fundamental condition for adapting the WFSC method to online processing. Analysis of the WFSC method using the three-component model indicates that the WFSC should be sampled at 100 cut-off velocities (Figure 3-3) to ensure accurate detection of the characteristic interval using the automated algorithm detailed in [2]. This result may pose a challenge to the goal of eventual real-time implementation of the WFSC method; however, in view of the short ensemble lengths employed during color flow imaging, a modest parallelization of the algorithm (e.g., evaluation of 4 or 8 cut-off frequencies in parallel) may be sufficient to enable real-time performance.

The three-component model also indicates that the tolerance of the WFSC method to frame-to-frame variations of CPD is relatively modest: any CPD variability greater than twice the variability observed in the flow phantom experiments [4] is predicted to increase the vascular quantification error to greater than the 5% target. With the expectation that *in vivo* images exhibit more inter-frame variations than phantom images, we are hoping to implement the *cpSNR* parameter as an initial condition for applying the online WFSC methods to acquired *in vivo* data in the future. In addition, CPD variability can be reduced by frame averaging if necessary to enable the WFSC method to be applied to *in vivo* imaging. Therefore, the sensitivity of the algorithm to CPD variability may prove to be the greatest barrier to real-time implementation of the WFSC method.

Furthermore, the three-component model also indicates that the performance of the current automated WFSC algorithm is comparable to the performance expected from idealized implementations of the method (*i.e.*, the perfect binary and closest methods considered in Section 3.2.4.3). Moreover, the percentages of correct selection whether in the middle or at the right-end of the detected interval (Figure 3-4) further support the selection-efficiency of the automatic algorithm. The conclusion that a binary choice between operating points at the middle and right end of a WFSC is sufficient, is consistent with the signal detection perspective upon which the model is based. When there is minimal to modest overlap of the three PDFs for the Doppler velocity estimates (representing an easily detected vessel), selecting an operating point cut-off velocity at the right end of the characteristic interval eliminates as many extra- and perivascular color pixels as possible while retaining most of the intravascular color pixels. On the other hand, when there is significant overlap among the three PDFs, the characteristic interval is predicted to be more steeply sloped. In this case, selecting an operating point at the middle of the characteristic interval maximizes discrimination between extra- and intravascular pixels with the compromise of retaining a substantial number of color pixels in the perivascular region.

When comparing quantization accuracy using the different selection methods, we chose to use the TOST procedure to test for equivalence instead of the typically used two-sample t-test. TOST procedure overcomes the challenges of using the two-sample t-test to test for equivalence. First, with the traditional two-sample t-test, the absence of substantial evidence to conclude that the mean values are different, the analyst can mistakenly default to the hypothesis that they are equal. Another problem associated with the use of the two-sample t-test is that it may lead the analyst to conclude that a statistically significant difference exists between the mean values when the magnitude of the difference is of no practical importance [15].

Simulation results (Figures 3-6 and 3-7) demonstrate that the interval length and minimum cut-off velocity are related to the accuracy of CPD as an estimate of the vascular volume fraction. As the quantification error decreases with increasing interval length (Figure 3-6), the minimum interval length for reliable quantification is defined as

the interval length at which the quantification error becomes lower than 5%. The reason for the reduced error beyond this point is that longer intervals become more horizontal than shorter intervals and therefore, are less affected by the accuracy of selection of the operating cut-off velocity being in the middle or right-end of the interval. By comparing Figure 3-6(a) and (b), we notice some cases present in Figure 3-6(b) only, in which the quantification error is almost 100% (at interval length < 3 mm/s), these cases correspond to an error in characteristic interval detection due to the added noise. However, they do not affect the overall accuracy of quantification as they are at intervals lengths below the reliable quantification threshold. In regards to defining the threshold for the starting cut-off velocity of a detected interval, the results of the analysis shown in Figure 3-7 did not provide a firm understanding of the relationship between quantification error and minimum cut-off velocity due to the lack of consistency between results using noise-free and noise-added signals. However, the inconsistent results shown in noise-added signal (Figure 3-7(b)) at higher cut-off velocities (> 3 mm/s) provide an understanding to the behavior of the interval detection algorithm [2] as the CPD variability increases. In this portion of Figure 3-7(b), the points corresponding to a very low quantification error (0%) are believed to exist as the characteristic intervals are detected starting at a higher cut-off velocity due to noise fluctuations in CPD value along the selection curve. On the other hand, the points within the same range of minimum cut-off velocity corresponding to a much higher quantification error (40%) could be caused by falsely detected intervals along the roll-off portion of the selection curves also due to noise fluctuations in CPD.

Therefore, with the assumption that any *in vivo* data acquired in future experiments will be considered relatively noise-added signals, we can conclude from results in Figures 3-6 and 3-7 that selection curves with short intervals (< 6 mm/s) or with intervals that begin at high cut-off velocity (> 3 mm/s) provide unreliable estimates of vascular volume fraction. Although, these conditions appear to be stricter than the conditions reported in our previous simulation study [4], it would be unreasonable to compare results from both studies for a number of reasons. First, with selection curves limited to 100 samples in the current study (vs. 10000 samples in [4]), each additional point along the curve corresponded to an increment of 0.178 mm/s, which resulted in a more discrete x-axis in Figures 3-6 and 3-7 and limited the results to multiples of 0.178

mm/s. In addition, the current analysis explored the relationship between interval length, minimum cut-off velocity and error in quantification for all simulated reference vascular volume fractions (F_v in Table 3-1) rather than analyzing it for a single color pixel density as in [4]. Finally, the large discrepancy between threshold values maybe attributed to the adjustments to both the interval detection and operating point cut-off selection algorithms in the improved WFSC method [2]. With these reasons in mind, we believe that the current conditions are more reasonable to implement in an online version of WFSC method as they correspond to using a practically feasible number of samples to construct the selection curves.

The above conclusions depend in part on the weights assigned to the cost function because the cost function defines the optimum cut-off velocity in this study. The weights were not formally validated, so the cost function is best understood as a means of making explicit the assumptions embedded in the WFSC method about the relative tolerability of false-positive color pixels in the extra- and perivascular regions. As stated in the Introduction (Section 3.1), the cost function was included to enable the above analyses to be performed without requiring time-consuming simulations to generate realistic power Doppler images. During the process of developing the cost function, synthetic images were produced using a Monte Carlo approach. These images, which were not included in this chapter in the interest of brevity, confirmed that the selected weights, as intended, define “optimum” cut-off velocities at which the majority of false-positive color pixels are confined to the perivascular region.

This conceptual model of color flow imaging can be applied to tasks other than analyzing the selection of wall filter cut-off velocity. The model can readily be modified to describe the sensitivity of CPD to other Doppler acquisition parameters such as gain and pulse repetition frequency, with the caveat that the Gaussian PDFs assumed in the current model may prove less applicable to other acquisition parameters. The model also implies that the shape of the WFSC carries information about blood flow in the ROI, e.g., changes in the complexity of the vascular network can be expected to shift and perhaps broaden the distribution of intravascular (and possibly also the perivascular) velocity estimates. The success in this study of the introduction of a log-normal distribution for

the intravascular velocity estimates provides a hint of this possibility, particularly in view of the fact that, as stated in Section 3.2.1, a hemodynamic justification exists for the choice of a log-normal distribution.

3.5 Conclusion

The proposed three-component mathematical model describes the relationship between wall filter cut-off velocity and power Doppler CPD more accurately than our original two-component model. The utility of the three-component model was demonstrated by applying it to analyze factors affecting the performance of our automated WFSC method for selecting a wall filter cut-off velocity. Development of an online implementation of the WFSC method will be guided by insights gained from the three-component model. Online implementation of the WFSC method is expected to be valuable for systems such as preclinical scanners and portable, point-of-care scanners that are typically operated by inexperienced or time-sensitive users. The WFSC method is also expected to improve the accuracy and reproducibility of power Doppler for quantitative microvascular imaging by enabling the wall filter cut-off velocity to be adapted to spatial and temporal (i.e., longitudinal) variations in blood flow conditions.

References

- [1] B. Morgan, "Opportunities and Pitfalls of Cancer Imaging in Clinical Trials," *Nat Rev Clin Oncol*, vol. 8, pp. 517-527, 2011.
- [2] M. Elfarnawany, S. Z. Pinter, and J. C. Lacefield, "Improved Objective Selection of Power Doppler Wall-Filter Cut-Off Velocity for Accurate Vascular Quantification," *Ultrasound Med Biol*, vol. 38, pp. 1429-1439, 2012.
- [3] S. Z. Pinter and J. C. Lacefield, "Detectability of Small Blood Vessels with High-Frequency Power Doppler and Selection of Wall Filter Cut-Off Velocity for Microvascular Imaging," *Ultrasound Med Biol*, vol. 35, pp. 1217-1228, 2009.
- [4] S. Z. Pinter and J. C. Lacefield, "Objective Selection of High-Frequency Power Doppler Wall Filter Cutoff Velocity for Regions of Interest Containing Multiple Small Vessels," *IEEE Trans Med Imaging*, vol. 29, pp. 1124-1139, 2010.
- [5] R. J. Zemp and M. F. Insana, "Experimental Validation of a Power Doppler Performance Model," in *Ultrasonics, 2003 IEEE Symposium on*, pp. 861-864 Vol.861, 5-8 Oct. 2003.
- [6] R. Zemp, C. Abbey, and M. Insana, "Ideal Observer Model for Detection of Blood Perfusion and Flow Using Ultrasound," in *Information Processing in Medical Imaging*. vol. 2732, C. Taylor and J. A. Noble, Eds., ed: Springer Berlin Heidelberg, 2003, pp. 318-329.
- [7] C. Kargel, G. Plevnik, B. Trummer, *et al.*, "Doppler Ultrasound Systems Designed for Tumor Blood Flow Imaging," *IEEE Trans Instrum Meas*, vol. 53, pp. 524-536, 2004.
- [8] C.-Y. Wu, M.-T. Lo, J. Tsao, *et al.*, "Factor Analysis in Both Spatial and Temporal Domains of Color Blooming Artifacts in Ultrasound Investigations Utilizing Contrast Agents," *Computerized medical imaging and graphics*, vol. 28, p. 129, 2004.
- [9] A. Nilsson, "Artefacts in Sonography and Doppler," *Eur Radiol*, vol. 11, pp. 1308-1315, 2001.
- [10] J. M. Hudson, R. Karshafian, and P. N. Burns, "Quantification of Flow Using Ultrasound and Microbubbles: A Disruption Replenishment Model Based on Physical Principles," *Ultrasound Med Biol*, vol. 35, pp. 2007-2020, 2009.
- [11] A. M. Mood, F. A. Graybill, and D. C. Boes, *Introduction to the Theory of Statistics*. New York: McGraw-Hill, 1973.

- [12] B. K. Al-Khazraji, N. M. Novielli, D. Goldman, *et al.*, "A Simple "Streak Length Method" for Quantifying and Characterizing Red Blood Cell Velocity Profiles and Blood Flow in Rat Skeletal Muscle Arterioles," *Microcirculation*, vol. 19, pp. 327-335, 2012.
- [13] R. K. Jain, "Delivery of Molecular and Cellular Medicine to Solid Tumors," *Adv Drug Deliv Rev*, vol. 26, pp. 71-90, 1997.
- [14] D. J. Schuirmann, "A Comparison of the Two One-Sided Tests Procedure and the Power Approach for Assessing the Equivalence of Average Bioavailability," *J Pharmacokinet Biopharm* vol. 15, pp. 657-680, 1987.
- [15] G. B. Limentani, M. C. Ringo, F. Ye, *et al.*, "Beyond the T-Test: Statistical Equivalence Testing," *Anal Chem*, vol. 77, pp. 221A-226 A, 2005.

Chapter 4

A two-stage process to improve quantitative three-dimensional power Doppler angiography of tumor microvasculature

The contents of this chapter are in preparation to be submitted to: Ultrasound in Medicine and Biology, as: “A two-stage process to improve quantitative three-dimensional power Doppler angiography of tumor microvasculature,” by M. Elfarnawany, M. R. Lowerison, M. N. Hague, A. F. Chambers and J.C. Lacefield.

4.1 Introduction

Studying tumor vasculature is fundamental in cancer studies due to the important role of blood vessels in promoting cancer growth and metastasis. Accurately depicting and quantifying these vascular networks is important to observe temporal changes to the networks during tumor development and to monitor responses of a tumor to anti-angiogenic and anti-vascular agents [1]. Power Doppler ultrasonography is a noninvasive imaging modality, characterized by high spatial resolution and sensitivity to blood flow in small vessels, which make it particularly useful for quantitative analysis of tumor vasculature [2-4]. A number of three-dimensional (3-D) power Doppler quantification metrics were developed by Carson et al. [5, 6] to quantify breast cancer vasculature. In 1999, Pairleitner et al., presented these metrics in their current standardized nomenclature: vascularity index (VI), flow index (FI), and vascularity-flow index (VFI), and assessed their usability and reproducibility using 3-D power Doppler images of human adnexal masses [7]. Thereafter, many cancer studies have used this method, often

termed 3-D power Doppler angiography, to visualize and quantify vasculature in tumor sites such as ovarian [8, 9], endometrial [10, 11] and breast cancers [12, 13].

Despite this abundance of literature on the application of quantitative 3-D power Doppler ultrasound to tumor vascular imaging, there exists some hesitation in defining the role of these power Doppler indices in clinical practice [14]. This hesitation stems from uncertainty about the interpretation of these indices due to the sensitivity of power Doppler signals to multiple factors such as operator-dependent machine settings and the irregularity and complexity of the vessel networks. The two-stage process introduced in this chapter is intended to analyze and standardize two of these factors to strengthen the role of 3-D power Doppler angiography in practice. The first processing stage is a clutter filter tuning method to improve the quality and accuracy of the reconstructed images. The second stage is a post-processing method to reduce artifacts in power Doppler images resulting from imaging complex and dense vascular networks.

One of the concerns with quantification of power Doppler images is its susceptibility to inaccuracies caused by any factor that alters the raw power Doppler signal, such as attenuation and operator-dependent machine settings [15]. Previous studies [16-18] made a significant contribution to understanding how machine settings such as gain, pulse repetition frequency, and wall filter cut-off frequency affect power Doppler quantification indices. These studies recommended choosing and maintaining fixed Doppler acquisition settings to provide reliable quantitative comparisons among subjects. Nevertheless, maintaining fixed acquisition settings may fail to achieve optimal performance as tumor vasculature changes with time in a longitudinal cancer study [19, 20], which can limit the reliability of comparisons between Doppler vascular indices computed in the course of the study. Therefore, having an objective method to select and adjust Doppler acquisition settings can be valuable for quantitative studies of changing or unpredictable vasculature such as tumor vascular networks.

Therefore, the first processing stage is the wall-filter selection curve (WFSC) method [21, 22], an operator-independent method to select the clutter filter cut-off frequency. A WFSC is constructed by plotting the color pixel density (CPD, equal to the

proportion of color pixels within a region of interest) as a function of the wall filter cut-off frequency. Selection curves are assumed to have one or more characteristic intervals depending on the number of vessels in the region of interest (ROI). One of these intervals is hypothesized to enclose the cut-off frequency at which the resulting image most accurately depicts the true vascular volume fraction of the imaged vessels. The method provides spatial tuning of the cut-off frequency by possibly selecting different cut-off frequencies in different subregions of a single ROI, depending on local variations in flow velocity and vessel size. The WFSC method was evaluated using multiple-vessel flow phantoms [22, 23] and isolated testicular vessels in mice [24] and provided more accurate vascular quantification in comparison to images processed using a single cut-off frequency throughout the entire ROI.

Another challenge for quantitative power Doppler imaging of tumor vessels is the inherent overestimation of moving blood volume in 3-D power Doppler images [17, 25]. This overestimation is usually displayed as a diffuse “blush” in regions of dense, complex vascular structures [26] such as the branching and tortuous vessels in a tumor vascular network. To reduce this overestimation and more accurately depict the vascular network morphology, Huang et al. [27] adopted a 3-D thinning algorithm to transform color pixel features in power Doppler images into sets of interconnected single-voxel-diameter vascular skeletons. These skeletons were used to extract vascular tree structures from the 3-D power Doppler images. The second stage of the proposed process is an adapted version of the method developed in [27] that is applied as a post-processing step during 3-D power Doppler image reconstruction.

In this chapter, we evaluate the effect of the two-stage process on 3-D power Doppler angiography using a murine tumor model. The chapter reports results from the first in vivo evaluation of the fully automated WFSC method [22] and establishes that the method is applicable to power Doppler signals acquired from tumor vascular networks. The results demonstrate that the WFSC-selected cut-off frequency varies as a function of position within a 3-D ROI and the histogram of cut-off frequencies from a tumor volume varies as the tumor progresses, so objective tuning of the cut-off frequency using the WFSC method has the potential to meaningfully improve power Doppler images of

tumor vessels. The results also show that the proposed two-stage processing approach produces a small increase in the correlation of power Doppler and contrast-enhanced ultrasound metrics of tumor vascularity. This increase in correlation is greater using the two-stage method than using either stage alone, so the two processing steps (the WFSC method and vascular skeletonization) combine in a complementary manner.

4.2 Materials and Methods

4.2.1 Experimental Image Acquisition

Three-dimensional power Doppler images were acquired using a 40 MHz linear array transducer (MS550D, FUJIFILM VisualSonics Inc., Toronto, Canada) and Vevo 2100 high-frequency imaging system (FUJIFILM VisualSonics) equipped with digital RF mode. The same power Doppler settings were used throughout the study (frequency, 32 MHz; power, 100%; B-mode gain, 22 dB; power Doppler gain, 30 dB; dynamic range, 65 dB; and pulse repetition frequency, 4 kHz). In addition, 3-D nonlinear (subharmonic) contrast-enhanced ultrasound (CEUS) images were acquired using an MS250 linear array transducer transmitting with a center frequency of 18 MHz following a bolus (50 μ L) tail vein injection of Vevo MicroMarkerTM (FUJIFILM VisualSonics) microbubble solution (2×10^9 microbubbles/mL). Baseline images were acquired before the injection of microbubbles and the enhanced images were acquired after full perfusion of the tumor was maintained. Images were acquired from a xenograft model (detailed in [28]) of a human breast cancer cell line (MDA-MB-231-D3H2-LNluc cells (Caliper LifeSciences, Alameda, CA)), 3 days post-implantation into the mammary fat pad of 8-week old female nude mice (NU/NU, Charles River Laboratories, Saint Constant, QC). During the course of a six-week study using 8 mice, power Doppler data were acquired three times per week, while nonlinear CEUS data were acquired once per week. All procedures complied with Canadian Council on Animal Care guidelines and were approved by the Animal Use Subcommittee of Western University.

4.2.2 The WFSC method

The WFSC method in [22] was extended to process 3-D quadrature demodulated (IQ) data instead of the scan-converted images analyzed in our previous work. Use of unfiltered IQ data enables retrospective application of any number of wall filter cut-off frequencies to construct the selection curves. Power Doppler processing software was developed in MATLAB R2013a (The MathWorks, Inc., Natick, MA, USA). For each image plane of a 3-D volume, Doppler IQ data were filtered using a third-order Type I Chebychev IIR wall filter at 100 increments of cut-off frequency from 0.005 to 0.5 times the pulse repetition frequency (PRF), which was set to 4 kHz. A third-order Chebychev filter was selected based on the analysis in [29, 30]. Each image plane was divided into adjacent, non-overlapping rectangular subregions of equal dimensions using an automated method detailed in [22]. The smallest rectangular window that maintains CPD < 0.80 in all subregions is used, so the number and size of the subregions varies among ROIs. Color pixel densities were computed after filtering at each cut-off frequency to construct WFSCs for each subregion. Characteristic intervals within these WFSCs were automatically identified as ranges of cut-off frequency that are bounded by local maxima in the normalized absolute first difference of the CPD, $|\Delta\text{CPD}|_{\text{norm}}$, using the algorithm detailed in [22]. One modification was made to the method in [22] for identifying the functional characteristic interval (*i.e.*, the interval used to select the operating cut-off frequency). Instead of simply using the leftmost interval as in the flow-phantom WFSCs, the functional characteristic interval in a tumor-based WFSC is defined as the interval enclosing the highest value of $|\Delta\text{CPD}|_{\text{norm}}$ among all detected intervals. This modification was necessary to deal with the higher number of detected intervals (versus two intervals in phantom WFSCs) resulting from the complexity of the imaged tumor vasculature. A rule-based decision algorithm [22] was then applied to choose either the middle or the end of the functional characteristic interval as the operating cut-off frequency, thereby yielding potentially different cut-off frequencies for each subregion. The 2-D frames were reconstructed by tiling the images of each subregion processed using its selected cut-off frequency and then the frames were stacked to form 3-D power Doppler regions of interest.

4.2.3 Vascular network skeletonization and reconstruction

A sequence of post-processing steps was employed to improve visualization of 3-D vascular networks. First, a 3-D power Doppler image was converted into a 3-D binary image, which was subsequently processed using a sequence of morphological operations proposed by [27] to suppress noise and fill cavities within vessels. Using a $3 \times 3 \times 3$ cubic structuring element, a sequence of two dilations, two erosions, and an opening operation were applied to the binary image. A vessel centerline skeleton was extracted from the processed binary image by applying the 3-D thinning algorithm proposed by Palagyi and Kuba [31]. A 3-D vessel tree was then reconstructed from the centerline skeleton by computing the vessel radius at each voxel along the centerlines. As proposed by [27], vessel radii were computed by reapplying the thinning algorithm to the 3-D power data and recording the maximum number of iterations required to reach the vessel centerline. The units for vessel radii were scaled to microns to compensate for the different voxel sizes in the axial, lateral and elevation directions. The power Doppler image was then masked using the 3-D vessel tree to generate an image with interconnected vascular structures and reduced color pixel clutter.

To isolate vessels within a tumor, a 3-D mask of the tumor surface was produced by manual segmentation of B-mode images and applied to the processed 3-D power Doppler image. The segmented tumor surface also used to compute the volume of the tumor by multiplying the total number of the voxels in the mask by the volume of one voxel.

4.2.4 Applicability of WFSC method to tumor vascular imaging

As an initial test of the effectiveness of the WFSC method for tumor imaging, selection curves and the resulting reconstructed images were visually inspected to confirm that application of the method to tumor images yields selection curves with characteristic intervals that can be detected using the rule-based algorithm from [22] and that the detected intervals have physically reasonable correspondence to the most prominent vascular structures in the images.

To assess the variability of the WFSC-selected cut-off frequency among subregions of a 3-D image, histograms of non-zero WFSC-selected cut-off frequencies were plotted. Our pilot study [32] indicated that two peaks (*i.e.*, distinguishable distributions) should be expected in these histograms. Therefore, the number of peaks, the cut-off frequency at each peak, and the area under each distribution were analyzed for each histogram. To study the correspondence of these histogram characteristics to the vascular properties in a 3-D power Doppler image, segmented versions of each 3-D image were produced that exclusively display subregions belonging to a particular distribution (e.g., a low or high cut-off frequency range) in the histogram. Moreover, longitudinal series of cut off histograms for each tumor were examined for trends that could be indicative of longitudinal vascular progression. Changes in the number and amplitude of the histogram peaks were compared to changes in tumor volume over time for each animal.

Further analysis of the histograms was performed to identify the vascular features common to all subregions in a segmented version of the 3-D image (low or high cut-off frequency image) that determine whether selected cut-off frequencies within that image are likely to belong to the low- or high-frequency distribution in the histogram. The candidate vascular features tested using the segmented (low and high cut-off) images were: 1) the total number of colored voxels representing the vascular volume in each segmented image, 2) the mean depth of vascular structures, 3) the mean radius of the vascular structures, and 4) the vascular length per unit volume in each segmented image, which was computed by dividing the total number of voxels forming the centerline skeleton by the total number of colored voxels in the corresponding 3-D vascular tree. These features were computed separately from the low- and high-cut-off versions of each vascular network and plotted as functions of time over the course of the longitudinal study. Where appropriate, the mean difference between a feature in the low- and high-cut-off segmented images was computed and normalized with respect to the maximum value of the feature, computed over the course of the longitudinal study. The normalized mean difference was tested for significance (compared to a null hypothesis of zero difference) using a Student's t-test in GraphPad Prism version 6.04 (GraphPad Software, La Jolla, CA, USA).

Finally, overall variations in the WFSC-selected cut-off frequencies were analyzed by performing a two-way analysis of variance (ANOVA) using GraphPad Prism to test for statistically significant differences in the mean cut-off frequency both longitudinally for each animal and across different mice.

4.2.5 Effect of WFSC method and skeletonization on vascular network visualization

The effect of the two-stage method on vascular visualization was evaluated qualitatively by visually comparing its reconstructed images to images processed using each stage in isolation and images constructed using conventional power Doppler processing. Four sets of images were produced for each animal at each time point. The first and second sets of images were produced using the WFSC method with and without skeletonization and vascular network reconstruction, while the third and fourth sets of images were generated using a fixed cut-off frequency with and without skeletonization. The fixed cut-off frequency was equal to the mean of the non-zero WFSC-selected cut-offs for that image volume. For longitudinal comparisons, the fixed cut-off assigned on the first scanning session of the study was applied to all subsequent time points to emulate conventional experimental procedures. The fixed-cut-off images generated without applying the skeletonization algorithm represent conventional power Doppler system processing.

4.2.6 Effect of WFSC method and skeletonization on vascular quantification

The effect of using the WFSC method and/or the skeletonization-based vascular reconstruction algorithm was quantitatively analyzed by computing the standard 3-D power Doppler indices VI, FI, and VFI:

$$\text{Vascularization index} = \frac{\text{color voxels}}{\text{total voxels in ROI}}, \quad \text{Eqn. 4-1a}$$

$$\text{Flow index} = \frac{\text{sum of powers of colored voxels}}{\text{volume of colored voxels (mm}^3\text{)}}, \quad \text{Eqn. 4-1b}$$

$$\text{Vascularization flow index} = \frac{\text{sum of powers of colored voxels}}{\text{volume of total voxels in ROI (mm}^3\text{)}}, \quad \text{Eqn. 4-1c}$$

The denominators of the FI and VFI metrics were modified from their original definition in [7] by replacing the number of voxels by the total volume occupied by these voxels in mm³ to compensate for longitudinal variations in the voxel size when using differently sized Doppler ROIs at different time points throughout the study.

From each of the four versions of the reconstructed images listed above (WFSC or fixed cut-off, with or without skeletonization), the VI, FI, and VFI metrics were computed twice, once to analyze the full vascular network in the Doppler color box and again for the intra-tumor vessels only. These repeated measures were performed to separately evaluate the sensitivity of each method to variations in overall vasculature as well as to intra-tumor vascular development. We assessed both the overall and intra-tumor performance since the tumors used in this study are characterized by a peripheral vascularization pattern in which blood vessels are mainly confined to the tumor periphery [19] with expanding regions of central necrosis as the tumor grows [33-35].

Variations in vascular quantification due to the different combinations of processing algorithms were analyzed by performing paired comparisons of a power Doppler metric (VI, FI, or VFI) for images acquired from the same mouse over the study period (16 to 18 time points). Comparisons were performed for the four pairs of image versions that differed in only one processing stage. Separate comparisons were performed for intra-tumor and overall vascular quantification using each Doppler metric. Paired Student t-tests were used with a Bonferroni correction to compute multiplicity-adjusted p values. From each set of comparisons, the maximum significant or minimum non-significant p-values over all mice (n=8) were reported.

Finally, the power Doppler VFI metric was compared to a contrast-enhanced ultrasound derived metric, which we called total enhancement:

$$Total\ enhancement = \frac{\sum Intensities\ from\ CEUS\ image - \sum Intensities\ from\ baseline\ image}{volume\ of\ total\ voxels\ in\ ROI(mm^3)}$$

Eqn. 4-2

The total enhancement (TE) metric is the mean background-subtracted intensity of the CEUS signal in an ROI and represents the fractional blood volume at peak enhancement. The mean background-subtracted intensity is typically evaluated using 2-D images [36, 37] but was adapted to be evaluated using 3-D contrast enhanced ultrasound images for direct comparison to the 3-D power Doppler images. Total enhancement was computed twice from each data set, once for the signal within the entire 3-D CEUS ROI and again from the signal within the tumor boundaries only to compare to the overall and intra-tumor power Doppler vascular metrics. The intra-tumor CEUS images were produced by applying a 3-D mask of tumor boundaries generated by manual segmentation of B-mode images to the 3-D contrast enhanced images. Since the contrast data were acquired once per week, a matching subset of the power Doppler VFI metrics for the same days were used in the comparisons. The VFI values from the four variations of processing techniques and the CEUS-derived TE metric, from all 8 mice, were compiled and tested for normality using the D'Agostino and Pearson omnibus normality test and then, depending on the normality test outcome, Pearson or non-parametric Spearman correlation coefficients were computed to compare the VFI in each type of power Doppler image to the TE. All statistical analysis was performed using GraphPad Prism version 6.04 (GraphPad Software, La Jolla, CA, USA). A p-value less than 0.05 corresponded to a significant difference.

4.3 Results

4.3.1 Characteristics of WFSCs for tumor images

Consistent with our flow-phantom data (Figure 4-1(a)) [22], selection curves for tumor images (Figure 4-1(b)) expressed a smoothly decreasing curve that exhibited one or more characteristic intervals corresponding to the number of distinct distributions of Doppler signal power. The characteristic intervals, though not easily distinguishable by visually studying the selection curve, were consistently bounded between two relatively high values of $|\Delta\text{CPD}|_{\text{norm}}$ (crosses marking the bars in Figure 4-1). Due to the complexity of the imaged tumor vasculature, the number of detected intervals (marked in red in Figure 4-1) in a selection curve for a tumor was typically greater than in the curves obtained from phantoms. Using the modified criteria for identifying the functional characteristic interval was valuable in tumor-derived WFSCs in which the highest value of $|\Delta\text{CPD}|_{\text{norm}}$ was frequently observed within intervals at higher cut-off frequency ranges and not within the left most interval typically used in phantom-constructed WFSCs. Other than that modification, the algorithm to select the operating cut-off frequency (blue circles in Figure 4-1) that was developed using flow-phantom data in [22] was applicable to WFSCs from tumors and yielded visually acceptable images.

4.3.2 Histograms of WFSC-selected cut-off frequency

For all 8 mice and all 16 time points, histograms of the cut-off frequencies selected for individual image volumes showed two distinct groups of subregions with lower and higher cut-off frequencies (Figure 4-2(a)). The mean cut-off frequency, which always lies between the two histogram peaks, was used to segment each 3-D image into versions showing subregions with low (less than the mean) cut-off (Figure 4-2(b)) and subregions with high (greater than the mean) cut-off (Figure 4-2(c)). Although it is difficult to visually differentiate the high- and low cut-off versions in a printed image, it was noted by examining the 3-D images from different orientations that, in comparison to the low-cut-off subregions, the high cut-off subregions generally represented longer vascular structures located along the borders of the tumors.

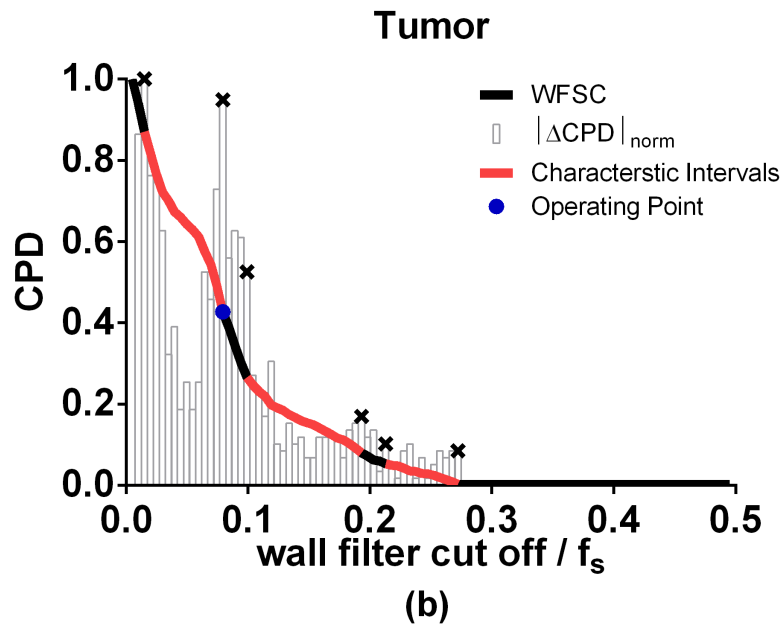
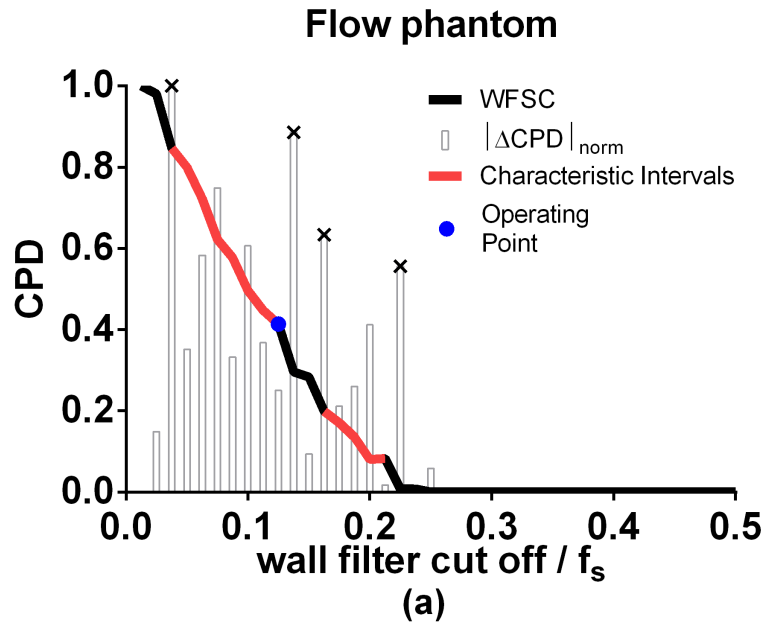
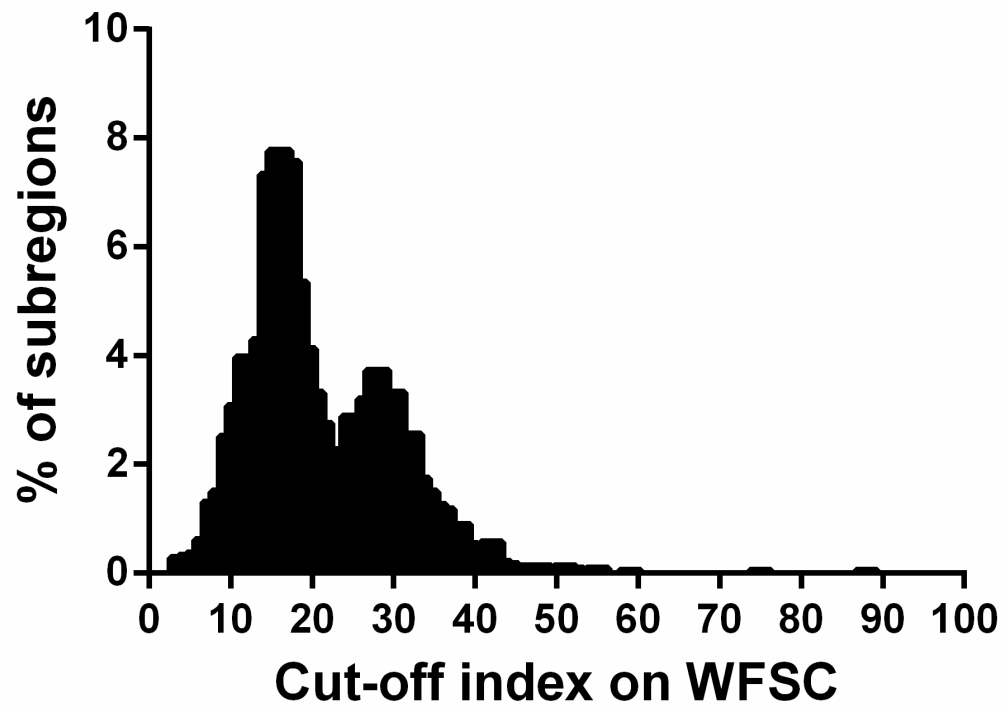


Figure 4-1: Sample WFSC curves constructed from (a) a multiple-vessel flow phantom and (b) an *in vivo* murine tumor model. The red intervals on the curves are the detected characteristic intervals bound by the peak values (marked by the 'x's) in the normalized first difference of CPD ($|\Delta\text{CPD}|_{\text{norm}}$, bars). The operating cut-off frequencies for these two curves are marked by the blue circles at the right ends of the first characteristic interval.



(a)

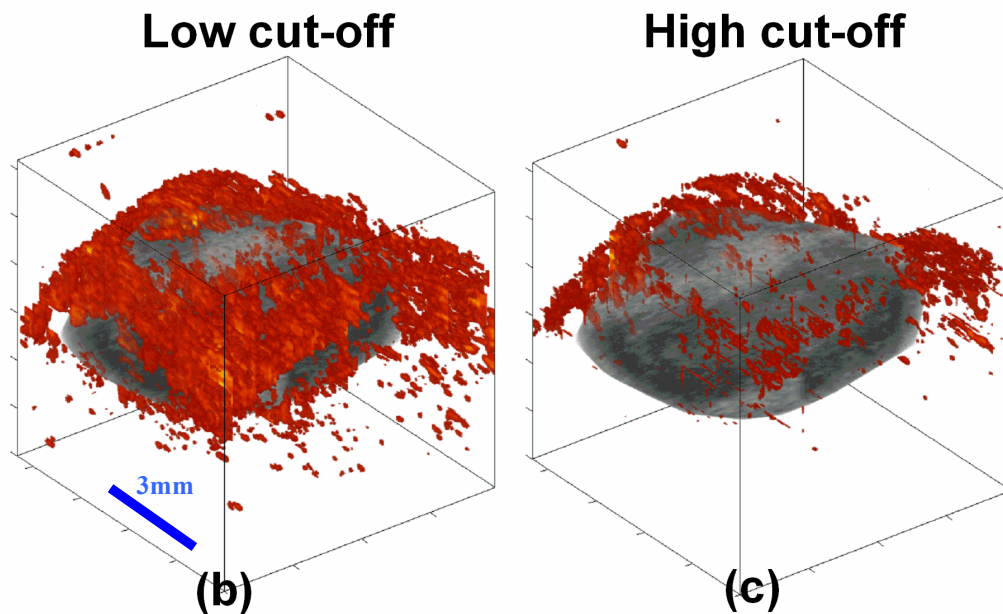


Figure 4-2: Variability of WFSC-selected cut-off frequency in 3-D images. (a) Histogram of cut-off frequencies in a representative 3-D volume. Masked versions of the same 3-D image showing subregions consisting of (b) low WFSC-selected cut-off frequencies and (c) high WFSC-selected cut-off frequencies.

4.3.3 Longitudinal variability of WFSC-selected cut-off frequency

Comparing cut-off-frequency histograms from the same animal at different time points in the study reveals a trend of changes in the two peaks of the histogram (Figure 4-3 (a-c)). As the tumors grew larger, more subregions exhibited lower cut-off frequencies, which caused the first peak to be consistently higher than the second peak. Figure 4-3(d) shows a sample trend of the changes in the total number of subregions with low and high cut-off frequencies (area under the low and high cut-off distributions in a histogram). In comparison to tumor growth. At the earlier time points, prior to the sudden increase in tumor volume (e.g., the first 5 data points in Figure 4-3 (d)), the image contains approximately equal numbers of low-and high-cut-off subregions. Starting from day 15 (5th point on Figure 4-3 (d)) and until the end of the study (day 43), the number of the low-cut-off subregions consistently exceeded the number of high cut-off subregions by more than 20%. The same trend was observed in 7 out of 8 mice with the number of low cut-off subregions starting to exceed the number of high cut-off subregions by more than 20% between day 12 and day 15 of the study.

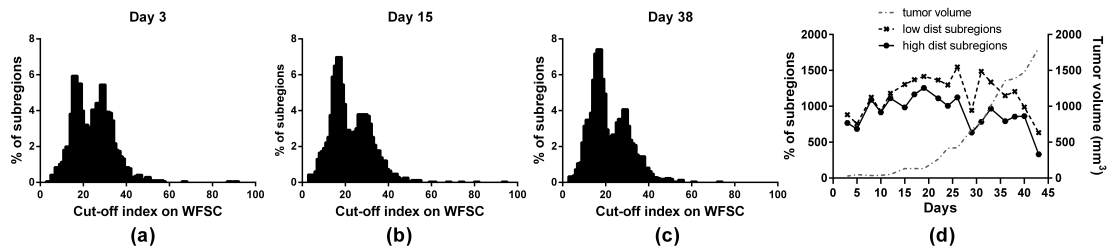


Figure 4-3: Longitudinal variations in cut-off frequency histograms as tumors grow: (a) Day 3 after tumor inoculation, both distributions with similar peaks. (b) Day 22, low cut-off distribution peak higher than high cut-off peak, (c) Day 40, difference between peak heights decreased. (d) Trends in number of low and high cut-off subregions to volume of tumor in mm³. The number of low and high cut-off subregions diverge at approximately day 15 coinciding with the large increase in tumor volume.

Overall, the mean WFSC-selected cut-off frequency showed significant variation among images acquired at different time points from each animal as well as variation among different mice (7 mice \times 15 time points, two-way ANOVA, $p < 0.0001$). There was also a significant interaction between the animal and time point ($p < 0.0001$). These results demonstrate the potential impact of adaptively tuning the cut-off frequency during a longitudinal cancer study in which different animals show different vascular progression kinetics.

4.3.4 Vascular features corresponding to WFSC-selected cut-off frequency

Longitudinal trends in several vascular features were inspected to identify the vascular characteristic that best describes the difference between the low- and high-cut-off frequency subregions. A sample longitudinal trend of the total number of colored voxels in the low- and high-cut-off subregions is shown in Figure 4-4 (a). In 7 of the 8 animals, the number of colored voxels in the low cut-off subregions exceeded the number of colored voxels in the high-cut-off subregions during the middle time points of the study (typically between days 19 and 36), but there were similar numbers of low- and high-cut-off voxels at earlier and later time points of the study. Since this parameter did not consistently differ between the low- and high-cut-off subregions, therefore, it cannot possibly be the basis for an automated method and thus, was excluded from further analysis. The mean depths of colored voxels in the low- and high-cut-off subregions (Figure 4-4 (b)) were not significantly different ($p = 0.5094$, average normalized mean difference = 0.86%) at any time point. The mean vessel radius did significantly differ ($p = 0.0010$) between the low- and high-cut-off subregions, albeit with a relatively small average normalized mean difference of 2.3%. The vascular feature that showed the highest, most consistent significant difference between high- and low-cut-off subregion was the vascular length per unit volume ($p < 0.0001$, average normalized mean difference = 42.1%). The high-cut-off subregions had a higher vascular length per unit volume than the low-cut-off subregions in all mice at all time points, as illustrated by the example in Figure 4-4 (d). A high vascular length per unit volume corresponds to longer, more-connected vascular structures, so the parameter reflects the morphology of the imaged 3-D vascular network in both groups of subregions.

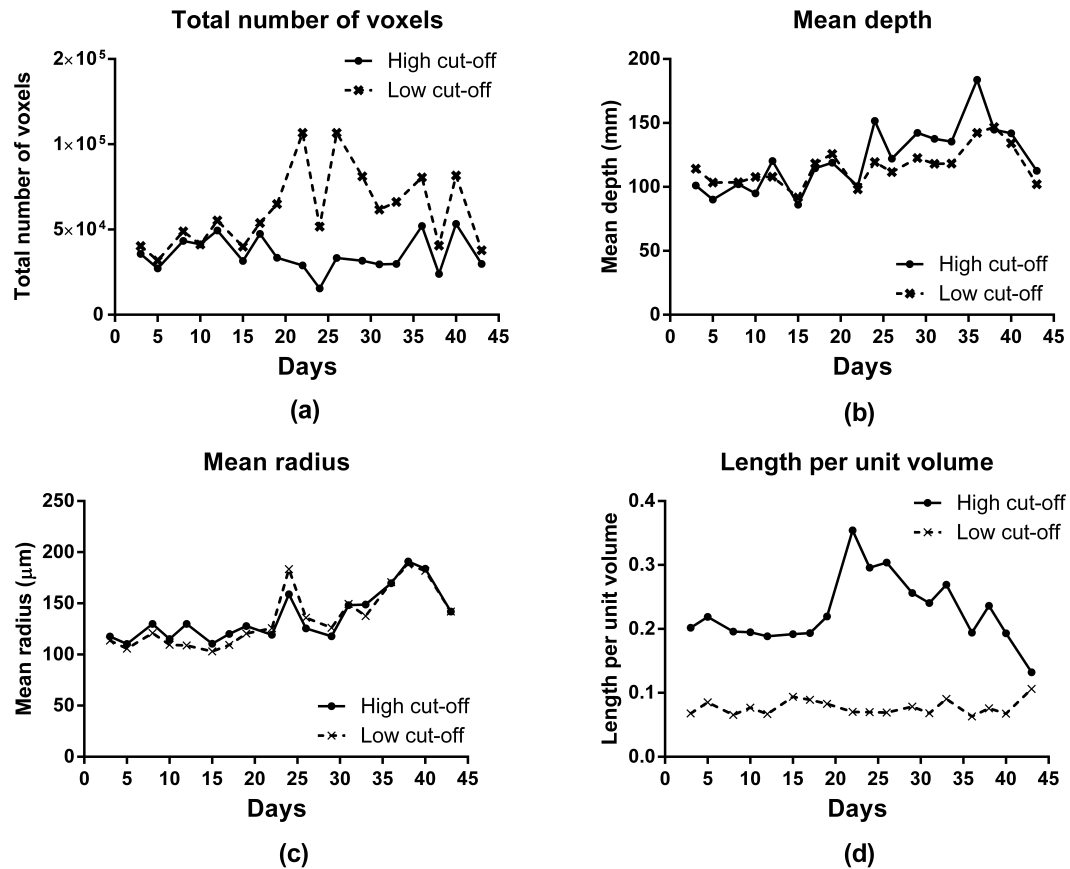


Figure 4-4: Longitudinal comparison of vascular features in the low and high-cut-off frequency portions of the 3-D vascular network identified using the WFSC method. (a) The total number of colored voxels in low- and high-cut-off subregions. (b) The mean depth of colored voxels in low- and high-cut-off subregions. (c) The mean vessel radius in low- and high-cut-off subregions. (d) The length per unit volume of vascular structures in low- and high-cut-off subregions.

4.3.5 Effect of WFSC method and skeletonization on vascular network visualization

The effect of the skeletonization algorithm on vascular network visualization can be appreciated by comparing the with- and without-skeletonization images in Figure 4-5. The tree-like structures of the vascular network were emphasized in the images processed with skeletonization (Figure 4-5 (b, c, f and g)), whereas the other images (Figure 4-5 (a, d, e and h)) displayed blurred regions of power Doppler signal. Similarly, images

processed using the WFSC method depicted additional vascular structures compared to volumes processed using a fixed cut-off frequency. The additional vascular structures detected using the WFSC method typically existed within tumor boundaries (Figure 4-5 (b versus c)). In other instances, the fixed-cut-off images overestimated the vascularity in the periphery of the tumor (Figure 4-5 (g versus f)). Therefore, combining the WFSC and skeletonization algorithms (e.g., Figure 4-5 (b and f)) provided the most improved depiction of the vascular network inside and in the periphery of the tumor.

4.3.6 Effect of WFSC method and skeletonization on vascular quantification

A summary of the results from individual comparisons of the vascular quantification metrics computed using the four different combinations of processing algorithms is shown in Table 4-1. The table reports each hypothesis test result in one of three formats. In cases where comparisons for all 8 mice showed significant differences in a vascular metric, the maximum p-value is reported (e.g., the results in the first two rows comparing images produced without and with skeletonization). When the majority, but not all, of mice produced significant differences in a vascular metric, the maximum significant *p*-value is reported along with the fraction, *m* of 8 mice, that exhibited significant differences in that metric. For example, in the third row of the table, comparing images processed using the WFSC method without skeletonization to images processed using a fixed cut-off frequency without skeletonization, a significant difference in VI for overall vasculature was observed in 6 of 8 mice. The third format is used when a majority of animals produced non-significant differences in a vascular metric, in which case, the minimum non-significant p-value is reported along with the fraction of mice that exhibited non-significant differences. For example, in the fourth row, comparing images processed using the WFSC method with skeletonization to images processed using a fixed cut-off frequency with skeletonization, a non-significant difference in VI for intra-tumor vasculature was observed in 6 of 8 mice.

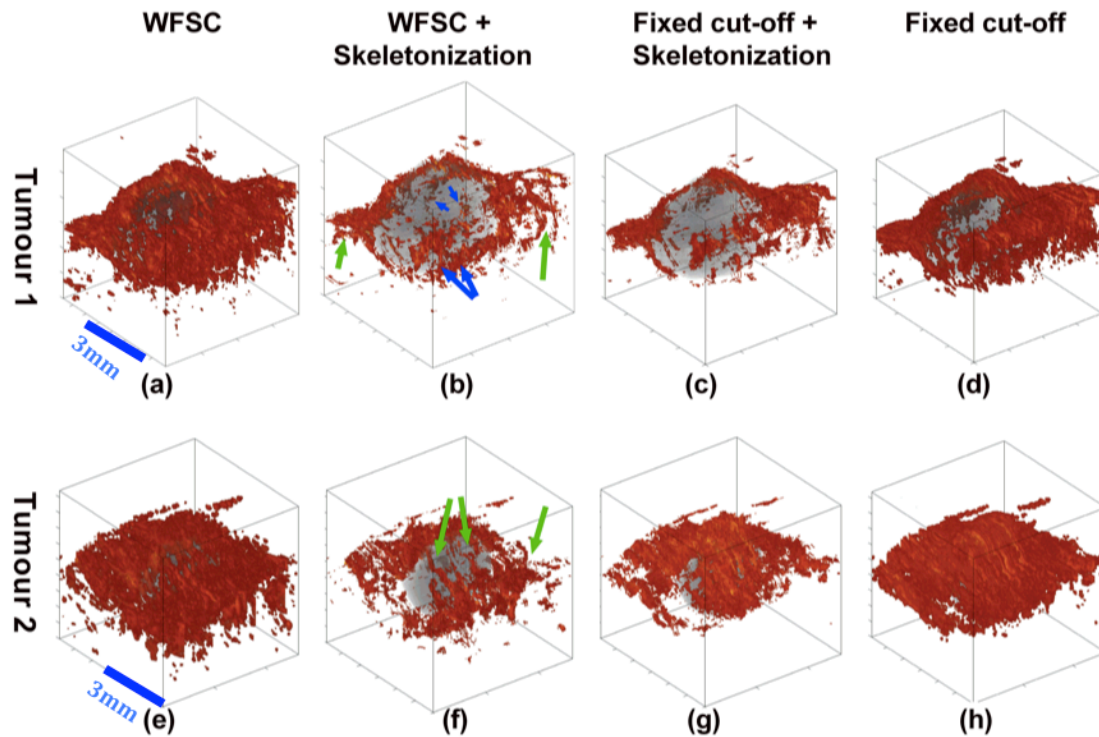


Figure 4-5: Effect of WFSC method and skeletonization algorithm on tumor vasculature visualization for representative tumors 1 (first row) and 2 (second row). Non-skeletonized images (a), (d), (e) and (h) show an undistinguishable pool of power Doppler signal whereas skeletonized images present a connected vascular network (b), (c), (f) and (g). 3-D image of tumor 1 (b) processed using WFSC method depicts additional vascular structures inside or on the border of the tumor (blue arrows) as well as better isolated vessels (green arrows) compared to image (c) processed using a fixed wall filter cut-off. 3-D image of tumor 2 (f) processed using the WFSC method provided better isolation of vessels (green arrows) compared to image (g) processed using a fixed wall filter cut-off.

The first two rows of Table 4-1 show that the choice to include or omit the skeletonization stage produced significant differences in all three indices (VI, VFI, and FI) for both intra-tumor and overall vasculature. The effect of skeletonization on intra-tumor VI and both intra-tumor and overall VFI was more consistently significant (*i.e.*, lower maximum *p*-values) when the WFSC method was also used.

The third and fourth rows of Table 4-1 show that the choice to use the WFSC method or a fixed cut-off frequency significantly changed the value of FI for both overall and intra-tumor vasculature, whereas the clutter filtering strategy significantly affected VI and VFI for overall vasculature only. The effect of the WFSC method on overall VI and VFI was more consistent (*i.e.*, more mice exhibited a significant difference and a lower maximum significant p value) when skeletonization was also used.

Table 4-1: Effect of WFSC and skeletonization algorithms on power Doppler quantification metrics, VI, FI and VFI for overall and intra-tumor vasculature.

| | | Overall Vasculature | | | | | | Intra-tumor Vasculature | | | | | |
|-----------------------------------|--------------------------|---------------------|-------------------|------|---------|------|-------------------|-------------------------|-------------------|------|-------------------|-----|-------------------|
| | | VI | | FI | | VFI | | VI | | FI | | VFI | |
| without vs. with Skeleton. | fixed cut-off | **** | <0.0001 | **** | <0.0001 | *** | <0.0024 | ** | <0.0068 | **** | <0.0001 | ** | <0.0336 |
| | WFSC | **** | <0.0001 | **** | <0.0001 | **** | <0.0001 | *** | <0.0008 | **** | <0.0001 | ** | <0.0064 |
| WFSC vs. fixed cut-off | without skeleton. | ** | 6 of 8 <0.0292 | ** | <0.0188 | ** | 7 of 8 <0.0312 | ns | 7 of 8 >0.1080 | ** | <0.0264 | ns | 6 of 8 >0.1244 |
| | with skeleton. | ** | <0.0148 | * | <0.0476 | ** | <0.0172 | ns | 6 of 8 >0.0596 | ** | 6 of 8 <0.0220 | ns | 6 of 8 >0.0940 |

Power Doppler VFI data for all four combinations of processing algorithms and the CEUS total enhancement data did not pass the D'Agostino and Pearson omnibus normality test ($p < 0.0084$ in all cases). Therefore, non-parametric Spearman correlation coefficients (Table 4-2) were computed. Correlation between the power Doppler VFI and CEUS TE was higher for intra-tumor vasculature than for overall vasculature. The four combinations of processing methods yielded similar correlation coefficients for intra-tumor vasculature. For overall vasculature, the correlation coefficients were statistically significant only when the WFSC method was used to select the cut-off frequency. A slightly higher correlation was achieved by applying skeletonization to the WFSC-processed images.

Table 4-2: Correlation between power Doppler and CEUS quantification for overall and intra-tumor vasculature.

| | Overall Vasculature | | Intra-tumor Vasculature | |
|--------------------------------|------------------------------|------------------------------|------------------------------|------------------------------|
| | WFSC | Fixed cut-off | WFSC | Fixed cut-off |
| Without Skeletonization | $r=0.3096$ ($p=0.0385$) | $r=0.2785$ ($p=0.0639$) | $r=0.7344$ ($p<0.0001$) | $r=0.6957$ ($p<0.0001$) |
| With Skeletonization | $r=0.3186$ ($p=0.0329$) | $r=0.2688$ ($p=0.0742$) | $r=0.7219$ ($p<0.0001$) | $r=0.6709$ ($p<0.0001$) |

4.4 Discussion

The two processing algorithms (the WFSC method and vessel skeletonization) presented in this chapter were designed to improve visualization and quantification of vascular networks using 3-D power Doppler imaging. Evaluation of the two-stage processing approach using an *in vivo* murine tumor model revealed significant variations in selected cut-off frequency within a 3-D ROI at one time point and over the study duration. Applying the two stages also improved the visualization of the tumor vasculature and produced a small increase in the correlation of power Doppler and contrast enhanced ultrasound quantification metrics of the imaged vasculature.

The first stage, the WFSC method, will have a tangible effect on vessel detection compared to conventional power Doppler imaging when the selected cut-off frequencies show significant variability within ROIs or over time. In this study, the overall significant variation of the mean WFSC-selected cut-off frequencies expressed by the two-way ANOVA ($p < 0.0001$) indicated that significant longitudinal and inter-subject differences in flow conditions exist in this tumor model and that the WFSC method is capable of adapting to those differences. In addition, the significant level of interaction between subjects and time point denoted the need for tailoring the temporal adjustment of the cut-

off frequency to the nature of the imaged vasculature, which makes the proposal of developing application-dependent standardized clutter filter setting [14, 18] more difficult to achieve.

Histograms were used to assess the variability of the selected cut-off frequencies among subregions in a 3-D image. The bi-modal nature of these histograms (Figure 4-2) in all animals and time points signified the importance of having different (at least two) cut-off frequencies for different portions of the imaged vasculature. The presence of two distributions denoted that selecting a single cut-off frequency for the whole region of interest may result in over- or underestimation of portions of the vascular network that belong to the other distribution. There was a clear visual distinction between images of the low and high cut-off subregions (Figure 4-2 (b and c)), which we hypothesize was based on certain anatomical or physiological features of the vasculature. However, due to the complexity of the tumor vascular network, it was difficult to visually identify these vascular features by studying images from a single time point. Hence, we analyzed longitudinal variations in the histogram and compared them to the vascular progression as tumors grew.

The curves in Figure 4-3 (d) summarize the longitudinal changes observed in the two histogram peaks and distributions (Figure 4-3 (a-c)) in a quantifiable form and present an interesting trend that we hypothesize follows the vascular development of our tumor model. The approximately equal numbers of low-and high-cut-off subregions in the earlier time points followed by the consistently higher numbers of low cut-off subregions (starting at day 15 in Figure 4-3 (d)), may correspond to the presence of tumor-induced vessels, which are fragile and tortuous [38, 39] and thus, would fall within the low-cut-off frequency range. Furthermore, the point of noticeable increase in tumor volume, which typically occurs due to an increased vascular supply to the tumor, matches the point at which the numbers of subregions with low and high cut-off frequencies diverge.

In addition, the correspondence between changes in the WFSC-selected cut-off histograms and longitudinal changes in the imaged vasculature, was confirmed using

quantifiable vascular features. With the WFSC method being fully automated, and assuming its performance depends on specific features of the vascular structures in the ROI, the pertinent vascular feature is expected to show a consistent, time-independent relationship that is distinguishable for the low and high cut-off images. The time-independence is an important property of the vascular feature to support the assumption that the longitudinal changes in the cut-off frequency histograms result from changes in the vasculature rather than changes in the performance of the WFSC method. To a lower extent, the significant mean of differences (2.3%, $p=0.001$) between the low and high cut-off images using the mean radius (Figure 4-4 (c)) indicate that the size of vascular structures can help define the suitable cut-off frequency for an ROI. Whereas, the highest, most significant mean of differences (42.1%, $p<0.0001$) between the longitudinal trends of the vascular length per unit volume feature (Figure 4-4 (d)), qualifies it to be the key vascular feature in differentiating the cut-off frequencies for different subregions using the WFSC method. The approximately constant values of this feature throughout the study duration suggest that the low cut-off subregions consistently enclosed relatively shorter or more discontinuous vascular structures in comparison to high cut-off subregions. This discriminating factor was insensitive to observed variations in the total number of colored voxels (Figure 4-4 (a)) or to the number of subregions in each category (Figure 4-3 (d)). The significant differences in this analysis indicated that the low and high cut-off subregions of the vasculature were distinguishable based on the morphology of the vascular network primarily by the length of the vessels and to a much less extent by the mean radii of the analyzed vasculature.

The ratio between the total vascular length and the total number of colored voxels is a modified version of the branching index (BI) proposed in [13]. Chen et al. defined the BI for 2-D power Doppler images as the ratio between the “perimeter” (i.e. total length) and the area of blood vessels. The BI reflects the morphology of vasculature by quantitatively describing its branching pattern. In our 3-D modified version, it was difficult to correlate the computed value to the branching pattern due to the complexity of the tumor 3-D vascular network. However, computing this metric provided the ability to relatively differentiate vascular network portions formed of longer, more connected vascular structures (larger value) from shorter, more scattered vascular components of the

vascular network. Accordingly, we can deduce that the length per unit volume estimate is one vascular feature that dictates the relationship between the color pixel density and the cut-off frequency in a region of interest.

The role of the skeletonization algorithm is to extract interconnected tree-like structures from the pool of power Doppler signal. Although 2-D and 3-D power Doppler are readily used to visualize and quantify vasculature, it was reported by Park et al. [25] that power Doppler tends to overestimate the blood flow signal. This observation is in agreement with Bude et al.'s [26] statements that power Doppler images display a diffuse "blush" when imaging small, densely arranged vessels, which are not resolved as discrete vessels. These descriptions matched our non-skeletonized images (Figure 4-5 (a, d, e and h)), which display a diffuse power signal all around the tumor with very few detectable vessels. This improved depiction of the vascular network helped to visually identify differences in the vascular network as we applied the different clutter filtering methods. Without skeletonization (Figure 4-5 (a, d, e and h)), it was difficult to visually identify these differences due to the diffused power Doppler signal. This contribution of the skeletonization algorithm to clarify differences between images processed using the different clutter filtering methods was quantitatively emphasized by the difference in significance between the third and the fourth rows of Table 4-1.

Therefore, by studying the images processed with skeletonization, we can recognize the additional vascular structures in WFSC-processed images (shown by the blue arrows in Fig. 4-5 (b) in comparison to Fig. 4-5(c)). In subregions where the WFSC method selected a lower cut-off frequency than the fixed cut-off filter, the additional vascular structures revealed by WFSC processing produced power Doppler signals that were attenuated or eliminated by the fixed cut-off frequency filter (*i.e.*, detection of these vessels required a cut-off frequency lower than that of the fixed clutter filter). These low cut-off structures were relatively short, scattered, and frequently located within tumor boundaries, which is consistent with the expected vascular characteristics of these tumors because MDA-MB-231-derived xenograft tumors are characterized by development of a necrotic core [33-35] and leaky, fragile neovasculature [38, 39] as described earlier. On the other hand, in subregions where the WFSC method selected a higher cut-off

frequency than the fixed cut-off, the WFSC method helped resolve regions of blurred and blended Doppler signal (green arrows in Figs. 4-5b and 4-5f in comparison to Figs. 4-5c and 4-5g, respectively) into more structured vessels or vessel branches. These structures were more accurately depicted using a higher cut-off frequency selected by the WFSC method, which reduced blooming artifacts around individual vessels. Therefore, images processed by combining both algorithms (e.g., Figs. 4-5b and 4-5f) provided the most comprehensive and realistic representation of the tumor vasculature.

Figure 4-5 illustrates that both components of the two-stage method contribute to improving the visual appearance of 3-D power Doppler images. The subsequent analyses of the effects of the method on vascular quantification were performed to evaluate whether those visual improvements yield significant changes in the outcome of quantitative imaging studies using power Doppler. The tests of VI, FI, and VFI in Table 4-1 were intended to assess the extent to which each processing stage, used alone and in combination, changes power Doppler estimates of tumor vascularity. The comparisons between VFI and CEUS total enhancement were intended to assess whether the changes to the images produced by the two-stage method improve the accuracy of tumor vascular quantification.

Analysis of the individual and combined effects of the WFSC method and skeletonization algorithms on the three standardized quantification metrics is shown in Table 4-1. Skeletonization had a more significant effect on all three metrics than did the WFSC method (*i.e.*, lower p -values in rows 1 and 2 versus rows 3 and 4 in Table 4-1). This result was expected due to the large impact of skeletonization on the 3-D power Doppler images as shown in Figure 4-5. The skeletonization algorithm reduced much of the “blush” in the power Doppler images producing very different representations of the vascular networks, which yielded statistically significant variations in VI, FI, and VFI. The cases in which skeletonization had a more significant effect on the WFSC-processed images in comparison to the fixed cut-off frequency images (row 2 versus row 1 for overall and intra-tumor VFI and intra-tumor VI in Table 4-1) may be attributed to the ability of the WFSC method to retain power signal from the small, slow-flow vessels that

are eliminated by a fixed cut-off frequency and thus increase the impact of the skeletonization algorithm.

Table 4-1 also shows that the clutter filtering method (WFSC vs. fixed cut-off) most significantly affected FI. Since FI is the mean Doppler power in voxels containing moving blood, which is independent of the number of color voxels, the selected cut-off frequency affects primarily the power value of the detected vasculature rather than the detectability of vascular structures themselves. This further emphasizes the importance of accurately selecting the cut-off frequency that reflects the true power intensity distribution within a vessel which corresponds to a realistic representation of the distribution of red blood cell concentrations within the vessel at the time of acquisition. In contrast, VI and VFI are affected by the accuracy of flow detection because they depend on the number of colored voxels. Therefore, the weaker signals from intra-tumor vascular structures and the nature of the imaged tumor vasculature caused intra-tumor VI and VFI to often be insensitive to the choice of clutter filtering method.

Contrast-enhanced ultrasound imaging was used to provide the gold standard *in vivo* vascularity measures to avoid the need to perform inter-modality image registration and correct for differences in spatial resolution and field of view. The CEUS total enhancement metric represents the change in mean intensity of the contrast signal from the baseline image to the image acquired at peak enhancement and is proportional to the mean microbubble density, which represents the fractional blood volume [36, 37]. The CEUS total enhancement metric was compared to the most similar Doppler metric, the VFI, which is the average Doppler power over all voxels in the ROI and can be regarded as an estimate of perfusion.

Similar to comparisons reported in other studies [40], correlations between the CEUS and power Doppler quantification for the overall vasculature (Table 4-2) were expectedly not strong (significant correlations are ranked as weak according to the Dancey and Reidy's correlation categorization [41]). A possible explanation is the increased sensitivity of contrast-enhanced ultrasound over power Doppler in detecting microvasculature including blood capillaries, which are not in the detectable range of

power Doppler [40]. It can be marked from the differences between the curves in Figure 4-6(a) that the CEUS total enhancement appeared more sensitive to the vascular progression of tumor-induced vasculature at week 4. Similar trends were observed in all mice.

On the other hand, the strong correlation (according to [41]) between the two metrics when analyzing intra-tumor vasculature (Table 4-2) is understandable, since their longitudinal trends (Figure 4-6 (b)) continuously decreased in similar fashions after week 2. This decrease in vasculature is consistent with the development of a necrotic core as the tumor grew. Necrotic cores should result in limited intra-tumor vascularity, which should reduce the gap between vascular detection with power Doppler and the reference contrast-enhanced ultrasound. A disadvantage of having limited intra-tumor vascularity in this tumor model is that it restricts the effect different processing combinations when comparing the power Doppler and CEUS quantification, which is reflected by the small variations in the correlation coefficients.

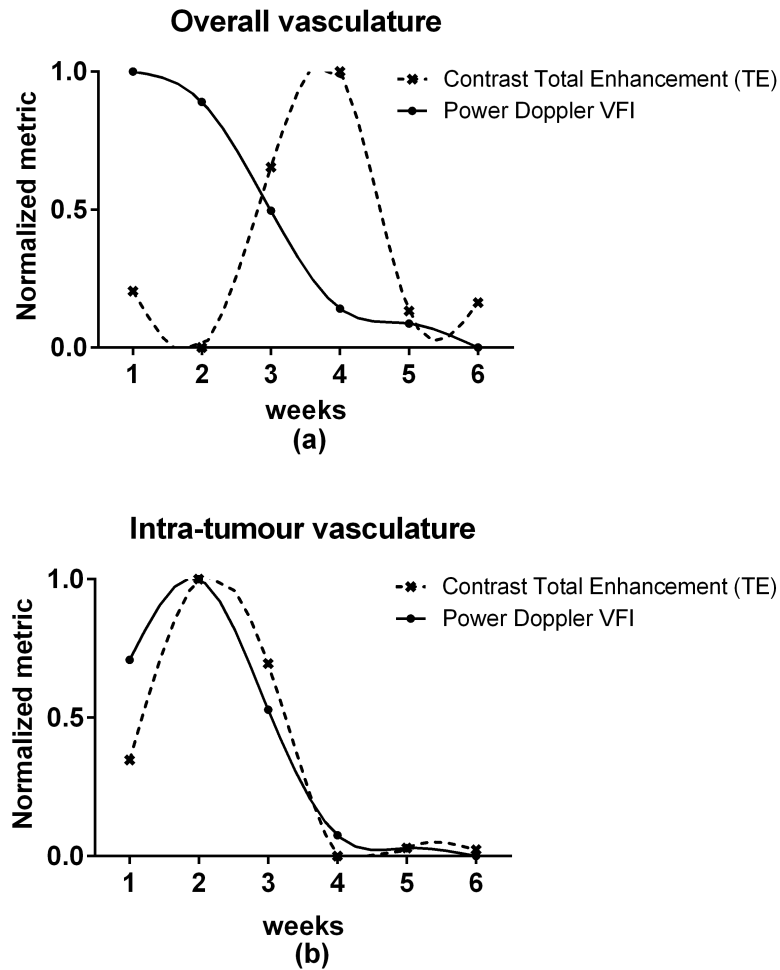


Figure 4-6: Longitudinal trends of power Doppler quantification metric: VFI using our two-stage process and contrast enhanced ultrasound metric: TE for (a) overall and (b) intra-tumour vasculature. The two metrics show weak significant correlation ($r=0.3186$, $p=0.0329$) for (a) overall vasculature due to rise in TE at week 4. Curves for intra-tumour vasculature quantification (b) are very similar with high significant correlation ($r=0.7219$, $p<0.0001$) of the power Doppler VFI metric to contrast enhanced ultrasound quantification.

Our study had some limitations. First, it was not possible to visually validate the 3-D images produced by the different combinations of algorithms due to the absence of a visual reference for the 3-D tumor vascular network. Although CEUS images were suitable for validation of the Doppler VFI, these images were not ideal for visual

validation due to the incompatible microvessel detection compared to 3-D power Doppler images. Second, the characteristics of the tumor model complicated the analysis of the subtle effects of the algorithms, especially at time points where a necrotic core was present. Future studies involving a simpler model would help analyze specific effects of the algorithms on the accuracy of depicting the imaged vasculature. Finally, the lower number of CEUS data sets in comparison to the power Doppler images from the same animal may have affected the statistical power of the correlation assessment of the vascular quantification. This can be avoided in the future by selecting an injection-free validation method that can be acquired as frequently as the power Doppler data.

4.5 Conclusions

This study evaluated a two-stage process to improve 3-D power Doppler angiography using a breast cancer xenograft model in mice. The first stage, the WFSC method, is effective for automated tuning of the clutter filter cut-off frequency in response to both differently perfused subregions within a 3-D image and to longitudinal vascular progression in tumors. The vascular feature that most strongly corresponds to the cut-off frequency selected by the WFSC method is the length per unit volume of the detected vessels, which is a measure of the continuity of the displayed vessels. The post-processing stage, a 3-D vascular skeletonization method, extracts vessel trees from the typically overestimated blood volume depicted in a power Doppler image. Skeletonization reduces color pixel blush from closely spaced, unresolved microvessels. The WFSC method improves detection of slow-flow vessels in subregions where a low cut-off frequency is desirable and reduces perivascular bleeding artifacts in subregions where a high cut-off frequency is appropriate. Combining the two stages improves visualization and quantification of 3-D power Doppler images of tumor vascular networks in comparison to conventional Doppler processing (i.e., a fixed cut-off frequency and no skeletonization). The two-stage process has the potential to improve the accuracy and reproducibility of qualitative and quantitative studies of complex, dense vasculature using 3-D power Doppler angiography.

References

- [1] M. de Jong, J. Essers, and W. M. van Weerden, "Imaging Preclinical Tumour Models: Improving Translational Power," *Nat Rev Cancer*, vol. 14, pp. 481-493, 2014.
- [2] J. M. Rubin, R. O. Bude, P. L. Carson, *et al.*, "Power Doppler Us - a Potentially Useful Alternative to Mean Frequency-Based Color Doppler Us," *Radiology*, vol. 190, pp. 853-856, 1994.
- [3] K. W. Ferrara, C. R. Merritt, P. N. Burns, *et al.*, "Evaluation of Tumor Angiogenesis with Us: Imaging, Doppler, and Contrast Agents," *Acad Radiol*, vol. 7, pp. 824-839, 2000.
- [4] F. S. Foster, C. J. Pavlin, K. A. Harasiewicz, *et al.*, "Advances in Ultrasound Biomicroscopy," *Ultrasound Med Biol*, vol. 26, pp. 1-27, 2000.
- [5] P. L. Carson, L. Xu, J. Pallister, *et al.*, "Approximate Quantification of Detected Fractional Blood Volume and Perfusion from 3-D Color Flow and Doppler Power Signal Imaging," in *Ultrasonics Symposium, 1993. Proceedings., IEEE 1993*, pp. 1023-1026 vol.1022, 31 Oct-3 Nov 1993.
- [6] P. L. Carson, J. B. Fowlkes, M. A. Roubidoux, *et al.*, "3-D Color Doppler Image Quantification of Breast Masses," *Ultrasound Med Biol*, vol. 24, pp. 945-952, 1998.
- [7] H. Pairleitner, H. Steiner, G. Hasenoehrl, *et al.*, "Three-Dimensional Power Doppler Sonography: Imaging and Quantifying Blood Flow and Vascularization," *Ultrasound Obstet Gynecol*, vol. 14, pp. 139-143, 1999.
- [8] J. L. Alcazar, L. T. Merce, and M. Garcia Manero, "Three-Dimensional Power Doppler Vascular Sampling: A New Method for Predicting Ovarian Cancer in Vascularized Complex Adnexal Masses," *J Ultrasound Med*, vol. 24, pp. 689-696, 2005.
- [9] M. J. Kudla, I. E. Timor-Tritsch, J. M. Hope, *et al.*, "Spherical Tissue Sampling in 3-Dimensional Power Doppler Angiography: A New Approach for Evaluation of Ovarian Tumors," *J Ultrasound Med*, vol. 27, pp. 425-433, 2008.
- [10] L. T. Merce, J. L. Alcazar, C. Lopez, *et al.*, "Clinical Usefulness of 3-Dimensional Sonography and Power Doppler Angiography for Diagnosis of Endometrial Carcinoma," *J Ultrasound Med*, vol. 26, pp. 1279-1287, 2007.
- [11] R. Galván, L. Mercé, M. Jurado, *et al.*, "Three-Dimensional Power Doppler Angiography in Endometrial Cancer: Correlation with Tumor Characteristics," *Ultrasound Obstet Gynecol*, vol. 35, pp. 723-729, 2010.

- [12] S. J. Kuo, Y. H. Hsiao, Y. L. Huang, *et al.*, "Classification of Benign and Malignant Breast Tumors Using Neural Networks and Three-Dimensional Power Doppler Ultrasound," *Ultrasound Obstet Gynecol*, vol. 32, pp. 97-102, 2008.
- [13] J. J. Chen, S. Y. Fu, C. S. Chiang, *et al.*, "A Preclinical Study to Explore Vasculature Differences between Primary and Recurrent Tumors Using Ultrasound Doppler Imaging," *Ultrasound Med Biol*, vol. 39, pp. 860-869, 2013.
- [14] J. L. Alcázar, "Three-Dimensional Power Doppler Derived Vascular Indices What Are We Measuring and How Are We Doing It?," *Ultrasound Obstet Gynecol*, vol. 32, pp. 485-487, 2008.
- [15] A. Welsh, "Quantification of Power Doppler and the Index 'Fractional Moving Blood Volume' (Fmbv)," *Ultrasound Obstet Gynecol*, vol. 23, pp. 323-326, 2004.
- [16] N. J. Raine-Fenning, N. M. Nordin, K. V. Ramnarine, *et al.*, "Evaluation of the Effect of Machine Settings on Quantitative Three-Dimensional Power Doppler Angiography: An in-Vitro Flow Phantom Experiment," *Ultrasound Obstet Gynecol*, vol. 32, pp. 551-559, 2008.
- [17] M. J. Schulten-Wijman, P. C. Struijk, C. Brezinka, *et al.*, "Evaluation of Volume Vascularization Index and Flow Index: A Phantom Study," *Ultrasound Obstet Gynecol*, vol. 32, pp. 560-564, 2008.
- [18] W. P. Martins, N. J. Raine-Fenning, R. A. Ferriani, *et al.*, "Quantitative Three-Dimensional Power Doppler Angiography: A Flow-Free Phantom Experiment to Evaluate the Relationship between Color Gain, Depth and Signal Artifact," *Ultrasound Obstet Gynecol*, vol. 35, pp. 361-368, 2010.
- [19] C. C. Zhang, Z. Yan, A. Giddabasappa, *et al.*, "Comparison of Dynamic Contrast-Enhanced Mr, Ultrasound and Optical Imaging Modalities to Evaluate the Antiangiogenic Effect of Pf-03084014 and Sunitinib," *Cancer Med*, vol. 3, pp. 462-471, 2014.
- [20] K. S. Ho, P. C. Poon, S. C. Owen, *et al.*, "Blood Vessel Hyperpermeability and Pathophysiology in Human Tumour Xenograft Models of Breast Cancer: A Comparison of Ectopic and Orthotopic Tumours," *BMC Cancer*, vol. 12, p. 579, 2012.
- [21] S. Z. Pinter and J. C. Lacefield, "Detectability of Small Blood Vessels with High-Frequency Power Doppler and Selection of Wall Filter Cut-Off Velocity for Microvascular Imaging," *Ultrasound Med Biol*, vol. 35, pp. 1217-1228, 2009.
- [22] M. Elfarnawany, S. Z. Pinter, and J. C. Lacefield, "Improved Objective Selection of Power Doppler Wall-Filter Cut-Off Velocity for Accurate Vascular Quantification," *Ultrasound Med Biol*, vol. 38, pp. 1429-1439, 2012.

- [23] S. Z. Pinter and J. C. Lacefield, "Objective Selection of High-Frequency Power Doppler Wall Filter Cutoff Velocity for Regions of Interest Containing Multiple Small Vessels," *IEEE Trans Med Imaging*, vol. 29, pp. 1124-1139, 2010.
- [24] S. Z. Pinter, D.-R. Kim, M. N. Hague, *et al.*, "A Method to Validate Quantitative High-Frequency Power Doppler Ultrasound with Fluorescence in Vivo Video Microscopy," *Ultrasound Med Biol*, vol. 40, pp. 1908-1917, 2014.
- [25] K. S. Park, B. I. Choi, H. J. Won, *et al.*, "Intratumoral Vascularity of Experimentally Induced Vx2 Carcinoma: Comparison of Color Doppler Sonography, Power Doppler Sonography, and Microangiography," *Invest Radiol*, vol. 33, pp. 39-44, 1998.
- [26] R. O. Bude, J. M. Rubin, and R. S. Adler, "Power Versus Conventional Color Doppler Sonography: Comparison in the Depiction of Normal Intrarenal Vasculature," *Radiology*, vol. 192, pp. 777-780, 1994.
- [27] S. F. Huang, R. F. Chang, W. K. Moon, *et al.*, "Analysis of Tumor Vascularity Using Three-Dimensional Power Doppler Ultrasound Images," *IEEE Trans Med Imaging*, vol. 27, pp. 320-330, 2008.
- [28] M. R. Lowerison, M. N. Hague, A. F. Chambers, *et al.*, "A Compound Speckle Model for Vascular Complexity Quantification in Nonlinear Contrast-Enhanced Ultrasonography," in *Ultrasonics Symposium (IUS), 2014 IEEE International*, pp. 2249-2252, 3-6 Sept. 2014.
- [29] S. Bjaerum, H. Torp, and K. Kristoffersen, "Clutter Filter Design for Ultrasound Color Flow Imaging," *IEEE Trans Ultrason Ferroelectr Freq Control*, vol. 49, pp. 204-216, 2002.
- [30] D. Kruse, R. Silverman, S. Erickson, *et al.*, "Optimization of Real-Time High Frequency Ultrasound for Blood Flow Imaging in the Microcirculation," in *Ultrasonics Symposium, 2000 IEEE*, pp. 1461-1464, Oct 2000.
- [31] K. Palàgyi and A. Kuba, "A 3d 6-Subiteration Thinning Algorithm for Extracting Medial Lines," *Pattern Recognit Lett*, vol. 19, pp. 613-627, 1998.
- [32] M. Elfarnawany, M. R. Lowerison, M. N. Hague, *et al.*, "In Vivo Evaluation of an Objective Method to Select Power Doppler Wall Filter Cut-Off Frequency for Microvascular Quantification," in *Ultrasonics Symposium (IUS), 2014 IEEE International*, pp. 436-439, 3-6 Sept. 2014.
- [33] J. T. Nofiele and H. L. Cheng, "Establishment of a Lung Metastatic Breast Tumor Xenograft Model in Nude Rats," *PLoS One*, vol. 9, p. e97950, 2014.
- [34] Y. Mao, R. Xia, L. Wang, *et al.*, "Multimodality Imaging Assessments of Response to Metformin Therapy for Breast Cancer in Nude Mice," *Chin Med J (Engl)*, vol. 126, pp. 3717-3722, 2013.

- [35] P. P. Adisheshaiah, N. L. Patel, L. V. Ileva, *et al.*, "Longitudinal Imaging of Cancer Cell Metastases in Two Preclinical Models: A Correlation of Noninvasive Imaging to Histopathology," *Int J Mol Imaging*, vol. 2014, p. 102702, 2014.
- [36] K. Wei, E. Le, J. P. Bin, *et al.*, "Quantification of Renal Blood Flow with Contrast-Enhanced Ultrasound," *J Am Coll Cardiol*, vol. 37, pp. 1135-1140, 2001.
- [37] E. Quaia, A. Nocentini, and L. Torelli, "Assessment of a New Mathematical Model for the Computation of Numerical Parameters Related to Renal Cortical Blood Flow and Fractional Blood Volume by Contrast-Enhanced Ultrasound," *Ultrasound Med Biol*, vol. 35, pp. 616-627, 2009.
- [38] C. J. W. Breward, H. M. Byrne, and C. E. Lewis, "A Multiphase Model Describing Vascular Tumour Growth," *Bull Math Biol*, vol. 65, pp. 609-640, 2003.
- [39] Z. M. Bhujwala, D. Artemov, and J. Glockner, "Tumor Angiogenesis, Vascularization, and Contrast-Enhanced Magnetic Resonance Imaging," *Top Magn Reson Imaging*, vol. 10, pp. 92-103, 1999.
- [40] M. E. Loveless, X. Li, J. Huamani, *et al.*, "A Method for Assessing the Microvasculature in a Murine Tumor Model Using Contrast-Enhanced Ultrasonography," *J Ultrasound Med*, vol. 27, pp. 1699-1709, 2008.
- [41] C. P. Dancey and J. Reidy, *Statistics without Maths for Psychology : Using Spss for Windows*, 4th ed. Harlow, England ; New York: Pearson/Prentice Hall, 2007.

Chapter 5

Improving microvascular depiction in three-dimensional power Doppler ultrasound using a two-stage processing method

The contents of this chapter are in preparation to be submitted to: IEEE Transactions on Medical Imaging as: “Improving microvascular depiction in three-dimensional power Doppler ultrasound using a two-stage processing method,” by M. Elfarnawany, N. Govindaraju, S. Pardhan, A. Makela, P. Foster, H. S. Leong, J. C. Lacefield.

5.1 Introduction

Power Doppler ultrasound is a valuable imaging tool used for the evaluation and quantification of vascularity in a variety of applications. One category of these applications is flow depiction, which depends on the improved vessel detection ability of power Doppler in comparison to other Doppler ultrasound-based blood flow imaging modalities [1]. Examples of flow depiction applications of power Doppler imaging are studying transcranial vessel morphology [2, 3], diagnosis of carotid artery stenosis [4, 5] and evaluating inflammation in musculoskeletal tissue [6, 7].

Despite this wide range of applications, users of power Doppler image experience some challenges and limitations when acquiring or analyzing images of blood flow. These challenges include the sensitivity of the acquired signal to operator-dependent instrument settings and the presence of Doppler artifacts that can hinder the visualization or quantification of imaged vasculature [8]. The wall filter cut-off frequency is one of the Doppler instrument settings used to eliminate signal reflected from moving tissue or

vessel wall and has received a lot interest in analyzing its effect on flow information displayed in images. Different settings of the wall filter cut-off frequency were shown to affect signal intensity of flow in power Doppler images [9] and to cause severe signal losses that could negatively affect the assessment of vascular stenosis [10]. Likewise, there are a number of Doppler artifacts that may risk the accuracy of vascular depiction in power Doppler images such as the blooming and jail-bar artifacts. The blooming artifact is a bleed of color, representing detected flow, outside of the vessel boundaries and may cause overestimation of the vessel size [8]. The jail-bar artifact is a set of periodic colored vertical lines displayed across the full region-of-interest (ROI) that can obscure or reduce signal from some flow sources within the ROI [11]. In an attempt to overcome some of these challenges, we propose an original power Doppler signal processing method that comprises an initial stage in which the wall filter cut-off setting is automated and an image post-processing stage aimed at reducing some of the artifacts in the reconstructed power Doppler images.

There are a few notable attempts to overcome these challenges by developing and improving Doppler signal processing methods. With regards to the wall filter cut-off setting, some investigators proposed new filter initialization techniques to existing filter designs [12, 13], while others developed more advanced adaptive wall filters [14, 15]. In 2009, we proposed a different approach of tuning the wall filter cut-off setting called the *wall filter selection curve* (WFSC), which uses the relationship between the fraction of colored pixels in the ROI (*i.e.*, the color pixel density, CPD) and the cut-off frequency to identify the optimum cut-off frequency for that ROI [16, 17]. This method was further developed into a fully automated, spatially tuned cut-off selection method for 3-D power Doppler images [18], which now represents stage 1 of the method presented in this chapter.

In terms of artifact reduction and improved vascular depiction, a novel image-processing algorithm presented in [19] helped reduce the blooming artifact in power Doppler images. Another example is the work presented by Lai et al. who developed a post-processing algorithm for three-dimensional power Doppler images to extract interconnected vascular networks that can potentially be used in diagnosis of breast

cancer [20]. Stage 2 of our proposed method is based on the work by Lai et al., but involves further development of the vascular network reconstruction technique. Yet, to our knowledge, there are no similar Doppler processing methods in literature that operate on both the unfiltered Doppler signal and the reconstructed power Doppler images to improve depiction and quantification of vasculature.

Our proposed two-stage method has passed through a number of development and evaluation cycles including flow-phantom experiments [17, 18, 21] evaluation using isolated testicular vessels in mice [22], and using a murine breast cancer tumor vasculature model [23]. Due to the complexity of the tumor vasculature involved in our most recent *in vivo* evaluation of the method [23], there was a need for a simpler, easier-to-validate model to specifically analyze the performance of method for vascular depiction applications. Therefore, the simple, regularly distributed vascular network of the chorioallantoic membrane (CAM) of *ex ovo* chick embryos was our model of choice for this study.

In this chapter, we evaluate the potential benefit of using our two-stage power Doppler processing in flow depiction applications. Using the simple chicken embryo CAM model, and by comparing 3-D power Doppler images processed using the two-stage method and images produced by a commercial ultrasound scanner set up by a licensed sonographer, we present the improved detection of smaller vessels or vessels of slower flow. We also show the ability of the two-stage method to reduce image artifacts and improve visualization of the vascular network. Finally, we show that vessel diameters measured using our two-stage processed images were more accurate than measurements made using images exported from the commercial scanner.

5.2 Material and Methods

5.2.1 Materials

Fertilized White Leghorn chicken eggs were obtained from (McKinley Hatchery, St Mary's, ON, Canada). Eggs were incubated for four days at 38 °C and 60% relative humidity in a hatcher with rotation (Sportsman hatcher, Berry Hill, cat. no. 1550HA). On

day 4, the eggs were removed from the incubator and transferred into an *ex ovo* culture system by placing the embryos in plastic weigh boats (VWR, cat. no. 89106-768) to expose the CAM and make it accessible for imaging. The *ex ovo* culture method was performed according to the protocol described in [24]. The shell-less chick embryos were returned to the incubator (38 °C, ~60% humidity) and were taken out to image the CAM vasculature on day 18. This embryonic age was chosen to carry out the experiments because the vascular system attains its final arrangement on day 18 [25].

5.2.2 Experimental protocol

To maintain temperature during the experiment, the embryos were placed over a warming pad of a water pump (T/Pump TP500, Gaymar Industries, Inc., Orchard Park, NY) set to 40 °C. A standard red light heating lamp was used to heat the air above the embryos. A total of 9 animals were used in this study. Each animal was photographed and imaged using power Doppler ultrasound. The embryos were allowed 2-5 minutes to stabilize prior to image acquisition. All procedures complied with Canadian Council on Animal Care guidelines.

5.2.3 Image acquisition

Photographs (2448 x 2448 pixels) of the full CAM surface were captured using an iPhone 5s camera (8 MP, Apple Inc, Cupertino, CA, USA). A sample photograph of a CAM surface is shown in Figure 1(a). The phone was placed on a custom made stage designed to keep the phone parallel to and at a fixed height from the CAM surface. To avoid light reflections on the transparent CAM surface, photographs were captured in a dark biosafety cabinet and a flexible USB-powered LED reading light lamp (HK126, XZT, Guangdong, China) was used to light the CAM surface.

Three-dimensional (3-D) power Doppler images of the CAM vasculature were acquired using a 40 MHz linear array transducer (MS550D, FUJIFILM VisualSonics, Inc., Toronto, Canada) and Vevo 2100 high-frequency imaging system (FUJIFILM VisualSonics, Inc) setup to the digital RF mode. Power Doppler acquisition settings were

adjusted by a licensed professional sonographer (A.M.) and were fixed throughout the study (frequency, 40 MHz; power, 100%; B-mode gain, 22 dB; power Doppler gain, 12 dB; dynamic range, 65 dB; pulse repetition frequency, 1 kHz; wall-filter, low). Warmed Aquasonic 100 ultrasound transducer gel (Parker Laboratories, Inc., NJ, USA) was applied to the transducer face and used for coupling between the transducer and the CAM surface. Drops of warmed saline were applied to the CAM surface at the CAM-transducer contact area as a lubricant to prevent sticking of the CAM surface to the transducer gel. Imaged regions of interest (ROI) were set to (lateral x axial x elevation= 13.88 x 10.00 x 14.10 mm with an elevational spacing between B-mode planes of 0.0762 mm) and were selected to include clear arterial and venular branching patterns far enough from the embryo body to reduce reflection and motion artifacts. The 3-D power Doppler images were exported in the quadrature demodulated (IQ) and in the raw (*i.e.* processed using scanner software) data formats.

5.2.4 Image processing

Areas in the photographs of the CAM matching the power Doppler ROIs were identified by visual inspection and marked using a rectangular selection tool in ImageJ (U.S. National Institutes of Health, Maryland, USA). The rectangle dimensions matched the lateral and elevational dimensions of the power Doppler ROI. Vessels within this ROI were identified and classified using the centripetal ordering method of microvascular mapping [26]. In this method, the smallest vessels that are in contact with the capillary network are defined as first-order vessels, which join together into second-order vessels that continue to successively join into vessels of increasing orders as illustrated in Figure 5-1(b). The type of vessels (arterial or venular) was determined by color since arterial CAM vessels are characterized by having a dark, deep color in comparison to venular vessels.

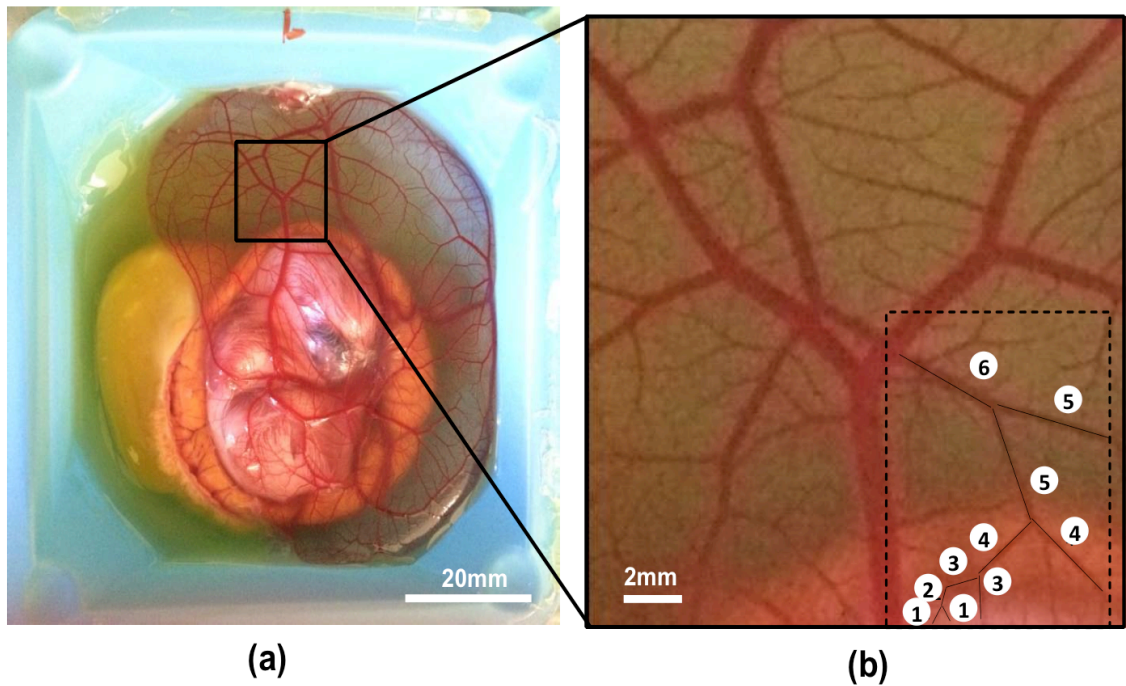


Figure 5-1: A sample optical photograph showing (a) the full vascular network of the chick embryo chorioallantoic membrane (CAM) and (b) a zoomed in version illustrating how first to sixth order vessels are determined using the centripetal ordering method of microvascular mapping. The smallest vessels, in contact with the capillary network, are defined as first order vessel.

5.2.4.1 Optical image processing

All image processing of the CAM photographs, summarized in the flow chart shown in Figure 5-2, was performed using ImageJ. Using the full view of the CAM surface, the scale was calibrated using the reference dimensions of the plastic weigh boats holding the embryos (8.9 cm x 8.9 cm). Images were then cropped keeping only the region within the rectangular ROI boundaries (Figure 5-2(b)). The following three processing steps were adapted from the image-processing algorithm presented in [27] to detect small vessels in a CAM optical image. Each image was split into its RGB channels

and only the green channel, in which the vessels had the highest contrast and were most continuous, was used. In order to enhance the image contrast, histogram equalization of the green intensities was applied (Figure 5-2(c)). Vessels edges were enhanced by applying a Laplacian of a Gaussian (LoG) filter [28], which improved the detection of smaller vessels in comparison to the original unfiltered image (Figure 5-2(d)). The Laplacian of a Gaussian filter is useful for detecting edges that appear at various image scales and degrees of image focus. Images were filtered using a LoG filter ImageJ macro developed by Dimiter Prodamov [29] by setting the kernel size to 10.

Additional processing to the steps proposed in [27] were required to reach the final images used for further analysis. Filtered images were binarized using Shanbhag thresholding method [30]. Gaps or holes in the vessels were filled by applying the “Remove Outliers” embedded function in ImageJ to dark pixels using a radius of 5 and a threshold of 50. The same function was used to remove background noise by applying it to bright pixels and setting the parameters to radius = 3 and threshold = 0. The “despeckle” embedded function was then applied to reduce the noise caused by very small vessels and capillaries and improve vessel-boundary depiction. A sample of the final binary images after hole filling and noise-reduction is shown in Figure 5-2(e).

5.2.4.2 Power Doppler processing

Power Doppler quadrature demodulated (IQ) data were processed using software implemented in MATLAB R2013a (The MathWorks, Inc., MA, USA) to apply the two-stage method presented in [23]. The first stage, the wall filter selection curve (WFSC) method, is an automatic, spatially tuned wall filter cut-off frequency selection algorithm. Each image plane of a 3-D volume is divided into adjacent, non-overlapping rectangular subregions of equal dimensions using an automated method detailed in [18].

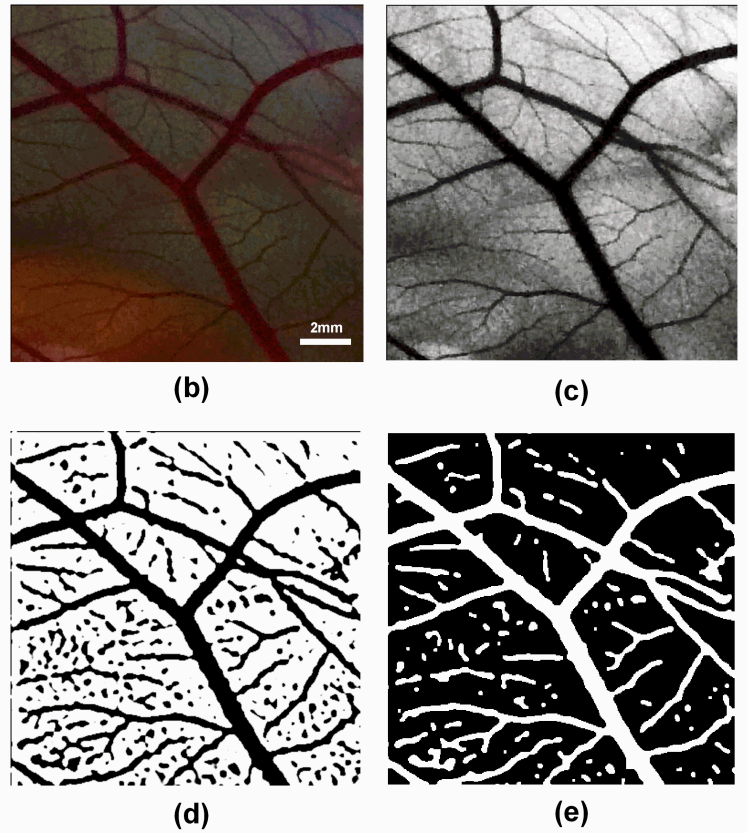
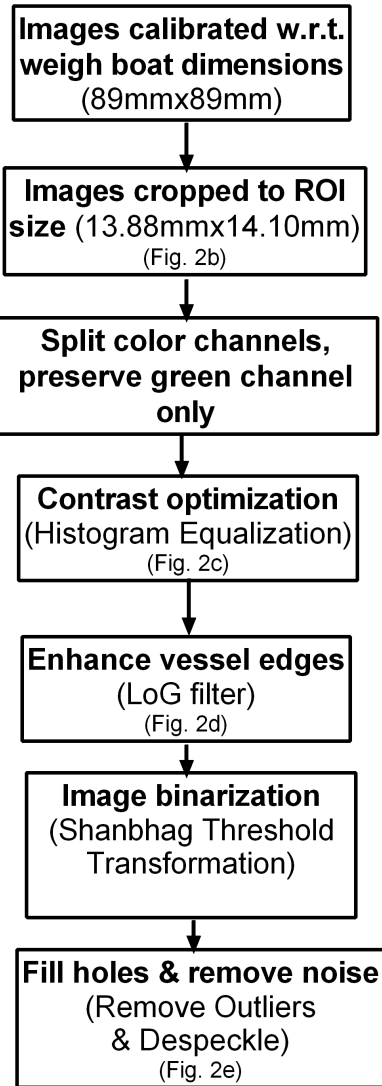


Figure 5-2: CAM optical image processing method with samples of results obtained at different stages of processing starting from (b) the unprocessed RGB image then showing the improved contrast image (c) after applying contrast enhancement to the green channel and (d) detected vessels using the Laplacian of Gaussian (LoG) filter and the final binary image (e) after filling holes and removing noise.

The number of subregions per ROI depends on the vascular density in the ROI because the algorithm uses the smallest subregion that contains no more than 80% colored pixels everywhere in the ROI. The WFSCs for these subregions are constructed by plotting the color pixel densities computed using 100 high-pass filtered version of the frame; each at an increment of cut-off frequency between 0.005 to 0.5 times the pulse

repetition frequency (PRF), which was set to 1 kHz. A third-order Chebychev high-pass filter was used based on the analysis in [13, 31]. Characteristic intervals within these WFSCs are automatically identified as ranges of cut-off frequency that are bounded by local maxima in the normalized absolute first difference of the CPD, $|\Delta\text{CPD}|_{\text{norm}}$, using the algorithm detailed in [18]. In cases where multiple characteristic intervals are detected, the interval closest to the location of the maximum $|\Delta\text{CPD}|_{\text{norm}}$ is used to select the operating cut-off frequency for each subregion. The frames are reconstructed by tiling the images of each subregion processed using its selected cut-off frequency. Stacking the reconstructed and spatially tuned versions of the frames then forms power Doppler three-dimensional volumes of regions of interest.

Stage 2 is an image post-processing algorithm used to extract interconnected tree-like structures from the pool of power Doppler signal. Extracting only connected vascular structures helps reduce common motion and flash artifacts in power Doppler images as well as the diffuse power Doppler signal “blush” resulting from imaging small, numerous vessels that are not depicted as discrete vessels. The “blush” in power Doppler images has been reported in many studies [32, 33] to cause an overestimation of the blood flow signal. Extracting the interconnected vessels is accomplished by applying the 3-D six-sub iteration thinning algorithm proposed by Palagyi and Kuba [34] to construct centerline skeletons of the vascular structures in the ROI. Using the generated centerline skeletons as a reference, we were able to capture the structural information (e.g. vessel radii, branches) of the connected blood vessels by reapplying the thinning algorithm to the 3-D power data and recording the number of iterations required to reach each voxel of the skeleton from all six directions. The computed number of iterations are then used to determine the number of voxels adjacent to each voxel of the centerline skeleton, in each of the six directions, to be filled with color and thus, reconstruct a full 3-D vascular network from the skeletons. Finally, the power Doppler image is masked using the 3-D vessel tree to generate power-weighted 3-D vessel structures with reduced color voxel artifacts.

5.2.4.3 Maximum intensity projection images

Maximum intensity projection (MIP) images of the 3-D Doppler images, in the lateral-elevation (*i.e.*, C-mode) plane, were produced to provide a comparable depiction of the vessel network to that in the optical photographs. Two sets of power Doppler MIPs were produced from each dataset, one using the exported raw (processed using the scanner software) 3-D images and the other using images processed using our two-stage method. The MIPs present a satisfactory depiction of the vascular network captured in the optical images due to the two-dimensional monolayer characteristic of the CAM vessel network [35]. The power Doppler MIPs were scaled for measurements using the known ROI dimensions (13.88×14.10 mm).

5.2.5 Data analysis

5.2.5.1 Vessel detection

Improvement in visualization of vascular structures was assessed by comparing 2-D and 3-D images of the vascular networks processed using our two-stage method to exported raw images processed using the Vevo 2100 scanner software. The numbers, types and orders of vessels depicted in our processed images only and not in the raw images were recorded for further analysis.

5.2.5.2 Level of striping artifact

The main artifact displayed in our 3-D images was a consistent stripe-like artifact parallel to the elevation direction. This type of striping artifact in the 3-D view can result from jail-bar artifacts in individual 2-D frames, which result from misinterpolation of Doppler signal in the presence of a strong reflector [11]. The strong reflector in this case is the floor of the weigh boat holding the chick embryo and its surrounding fluid. The amount of artifact in the images was quantified by computing the average number of colored voxels in each elevation line. A large value indicates the presence of more stripes in the 3-D image. These values were compared between 3-D images produced using our proposed method and the scanner's processing method.

5.2.5.3 Accuracy of diameter measurement

The number and size of pixels in the optical and Doppler images were matched using resize option in ImageJ. Diameters of the previously identified and labeled vessels were measured in millimeters using the line segment selection tool. Three diameter measurements were made at different points along each vessel segment to estimate the mean vessel diameter. Vessel diameters for 83 vessels of different types and sizes were computed from Doppler MIPs (raw and two-stage-method processed) and were compared using corresponding measurements from the optical photographs as a reference. The reference measurements from optical photographs were compared to similar estimates from the literature of diameter ranges for the studied vessel orders in the chick CAM.

5.2.6 Statistical analysis

The level of striping artifact in the produced 3-D images was compared using multiple Student's t-tests corrected using the Sidak-Bonferroni method. The overall change in the level of artifact between the two processing methods was expressed by the mean and standard deviation (over the nine CAMs) of the percentage difference of the amount of artifact by the two methods in each animal.

The linear dependence between diameter measurements from images processed using either Doppler processing software and measurements from the reference optical photographs were expressed by computing Pearson correlation coefficients. The Steiger's Z-test for "correlated correlations" within a population was used to test the correlation coefficient difference [36]. The accuracy of diameter measurements was evaluated by computing the percent error in measurements using the reference optical photographs. Since these errors were not part of a normal distribution (D'Agostino and Pearson omnibus normality test, $p < 0.0001$), an overall estimate of accuracy for each processing method was computed as the median absolute percentage error (MAPE) over all vessel measurements. In addition, pairs of percent errors resulting from the two processing techniques were compared using a Wilcoxon matched-pairs signed rank test for statistical significance. Finally, the histogram of all percent errors by each processing method was plotted to analyze the range and frequency of obtained errors.

The same analysis steps: computing the MAPE, testing for statistical significance using the Wilcoxon matched-pair signed rank test and plotting the histogram of percent errors, were repeated after dividing the set of vessel measurements based on the vessel type (arteries or veins). This analysis was performed to get more insight on the relationship between vessel type and the performance of the two processing methods and their role in reducing or exaggerating diameter estimation errors.

A more in-depth evaluation of the diameter measurement accuracy was performed by categorizing the evaluated vessels based on type and vessel order and comparing the ranges of percentage errors (minimum to maximum) for each category between the two processing techniques. All statistical analysis was performed using GraphPad Prism version 6.04 (GraphPad Software, La Jolla, CA, USA) except for the Steiger's Z-test, which was performed using computer software by Lee and Preacher [37]. P values less than 0.05 were considered statistically significant.

5.3 Results

5.3.1 Vessel detection and visualization

Processing power Doppler data using our proposed two-stage method often improved detection of vessels within individual 2-D frames. For example, two small vessels (marked with white arrows in Figure 5-3(b) were depicted with moderate power in the frame processed using the two-stage method and were not depicted in the corresponding frame (within the white oval boundaries) exported from the commercial Vevo 2100 scanner Figure 5-3(a).

Another observed improvement in the visualization of vessels processed using our two-stage method is strengthening the power Doppler signal intensity of vessels that were depicted in the commercial scanner processed frame with a weak, single color hue display (vessels marked with white arrows in Figure 5-3 (c and d). These vessels appear

with a stronger, gradual change in power with the highest power at the centre of the vessels and decreasing towards the vessel wall, which matches the power profile depicted in the larger vessels within the frame.

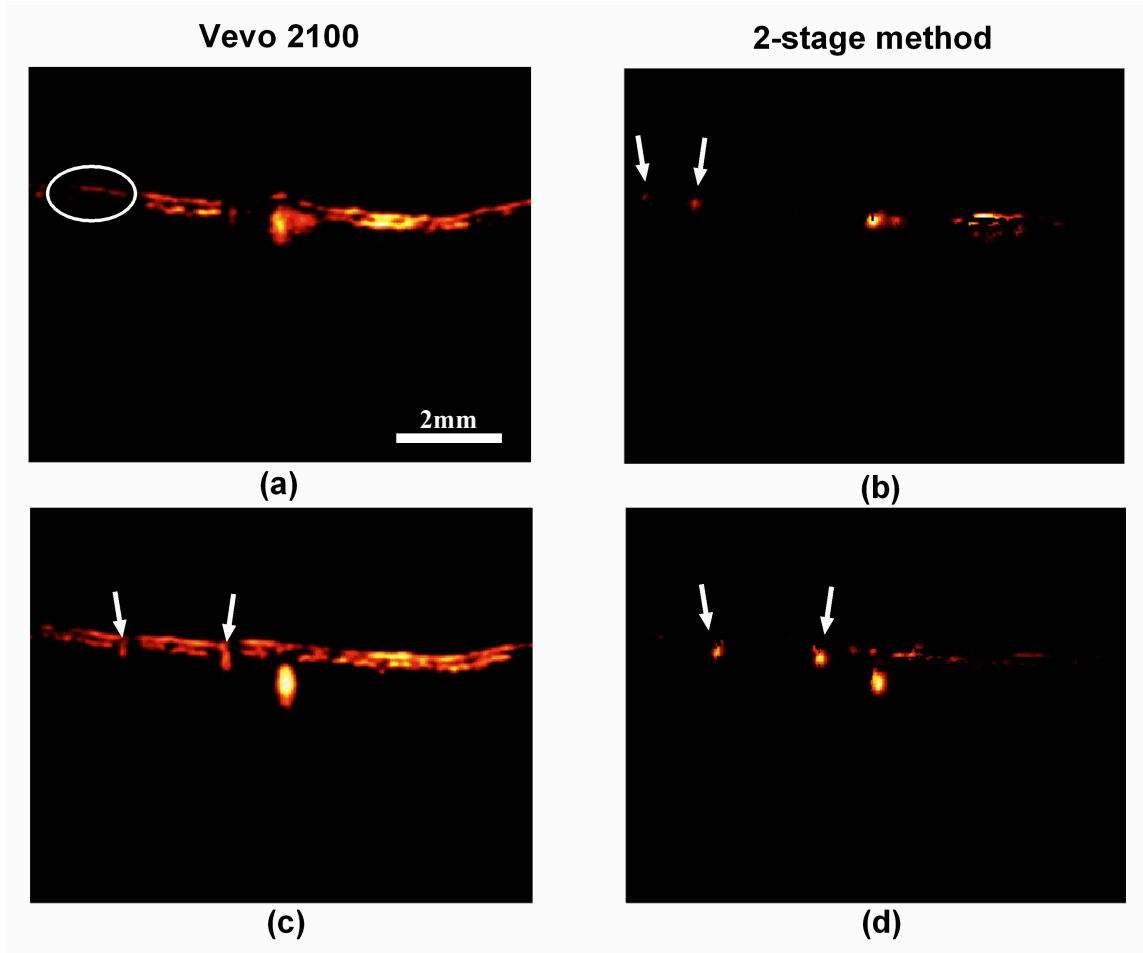


Figure 5-3: Improved vessel detection and visualization in images processed using our two-stage method versus commercial scanner (Vevo 2100) processed images. Sample comparisons show extra vessels (marked by white arrows) in (b) not detected in (a) and vessels (marked by white arrows) in (d) displaying improved signal intensity distribution within vessels versus being depicted as a single intensity (c). Color scale of all images has a dynamic range of 65dB.

The combination of the WFSC and skeletonization methods allowed the detection of some vessels that were not detected in the scanner-exported images, which are summarized according to their number, type and order in Table 5-1. The smallest detected vessels were fourth-order veins which were the only fourth-order vessels detected in all images. The majority of the vessels (a total of 8) detected only after applying the two-stage processing were of fifth order, which is the vessel size for which only one venular vessel was commonly detected in the Vevo2100 and the two-stage processed images. Conversely, there were no vessels detected in the Vevo2100 exported images and not in the two-stage processed images. The number of vessels of each vessel order detected by both processing methods (two-stage method and Vevo 2100 processing) is reported later in Table 5-2.

Table 5-1: Number and sizes of vessels depicted in two-stage processed images only.

| Vessel order | Number of detected vessels | |
|--------------|----------------------------|-------|
| | Arteries | Veins |
| 4 | 0 | 2 |
| 5 | 5 | 3 |
| 6 | 1 | 0 |

Examples of vessels revealed by the two-stage processing are the vessel branches (marked with blue arrows in Figure 5-4(b)) are not seen in the corresponding 3-D images exported from the Vevo 2100 scanner (Figure 5-4(a)). In other cases, the improved visualization produced by the two-stage method helped extract vessels that were otherwise obscured by image artifacts. An example for this type of improved visualization is illustrated in Figure 5-4 (c and d) by the vessels marked by the blue arrows.

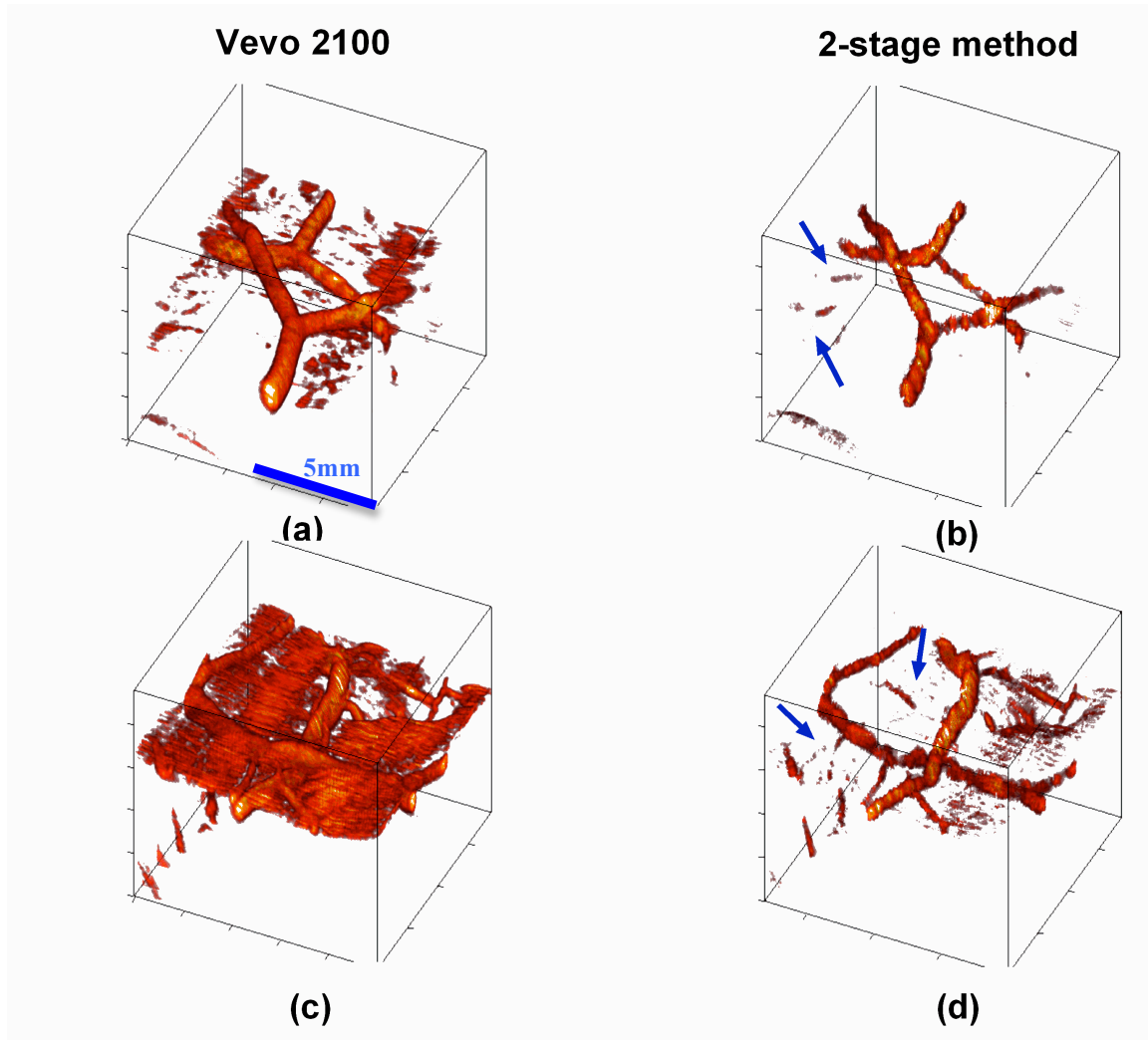


Figure 5-4: Improved vessel detection and visualization in 3-D images processed using our two-stage method versus commercial scanner (Vevo 2100) processed images showing extra branches of vessels (marked by blue arrows) in (b) and (d) not displayed in (a) and (c), respectively.

5.3.2 Level of striping artifact

Quantifying the striping artifact using the average number of colored voxels in each elevation line was consistent with the level of artifact observed by visual inspection. The variation in the amount of artifact between animals is expressed as the mean \pm 95

confidence interval as shown in Figure 5-5(a). Animals with a low level of artifact (e.g. CAM B) had fewer stripes, as seen in Figure 5-5(b), whereas CAM D, shown in Figure 5-5(d), represents an example of a high level of artifact with the stripes obscuring almost the full vascular network. For each individual animal, regardless of whether the Vevo 2100 images had a low or high level of artifact, our proposed two-stage method resulted in a significantly lower level of artifact ($p < 0.0001$ for all 9 animals) than the artifact level quantified in the Vevo 2100 images (Figure 5-5(a)).

In cases of low artifact (CAM B, Figure 5-5 (b and c)), the reduction of the artifact using the two-stage method (Figure 5-5(c)) did not cause loss of signal from any of the vessels depicted in the commercial system images (Figure 5-5(b)). Overall, using the two-stage method reduced the amount of artifact in all analyzed animals by $52.4 \pm 13.5\%$.

5.3.3 Accuracy of diameter measurement

Mean diameter measurements for each vessel order from the optical photographs were all within the ranges from data reported in literature as summarized in Table 5-2. The ranges of vessel diameters were extrapolated from reported ranges of first-, second- and third-order vessels (40-60, 70-90, 90-140 μm respectively) in [38] using the assumption that a lower order vessel would have a diameter 71% of its parent (higher order) vessel to achieve most efficient blood flow [39]. The extrapolated ranges were validated by taking sample full arterial trees (starting from the main artery to the smallest measurable branch) and confirming that each vessel order was within its corresponding diameter range. Although the lowest measurable vessel order from the optical images was commonly the third order, we only included measurements starting from the fifth order (200 - 280 μm) since this was the minimum detectable vessel order in images from both Doppler processing methods.

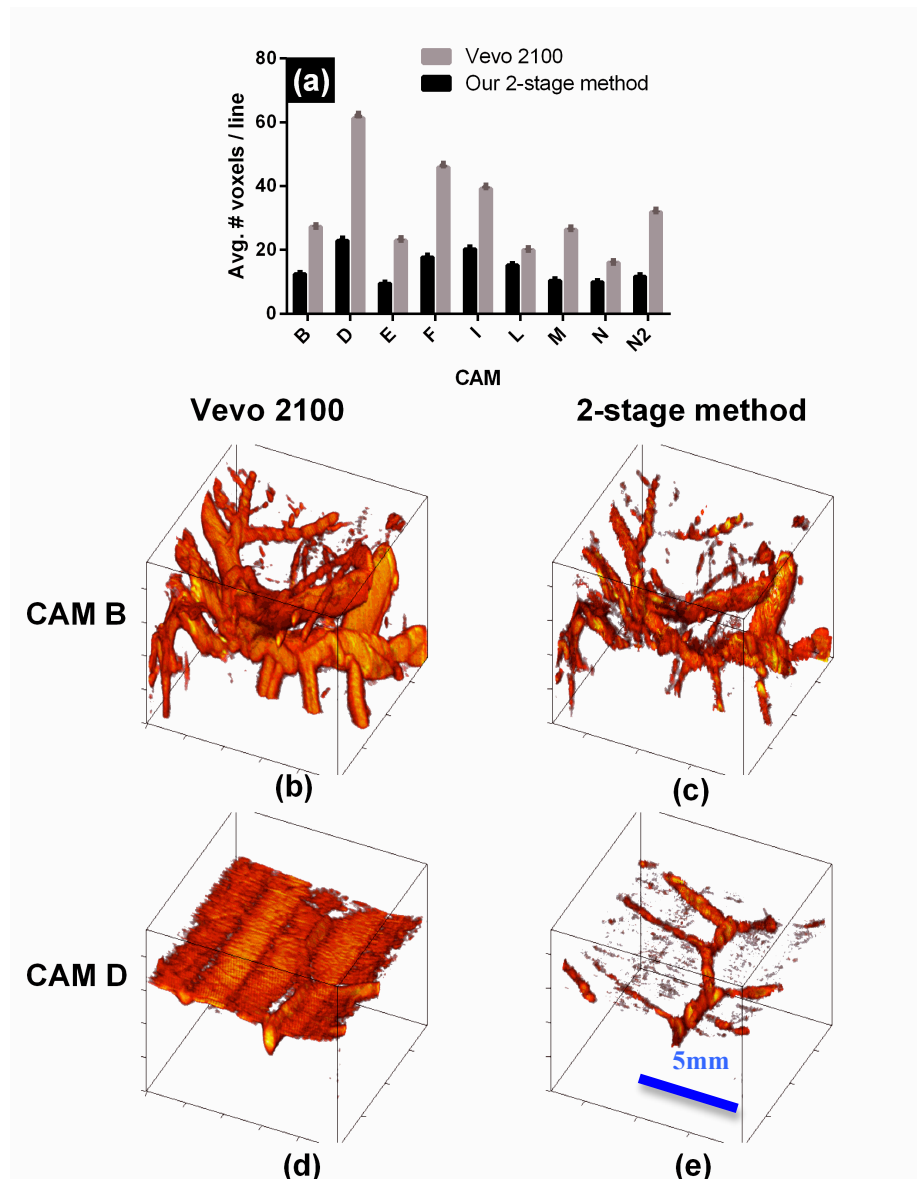


Figure 5-5: Quantified level of artifact from images processed using the two-stage method versus the commercial scanner (Vevo 2100) software for different animals. Images from a sample animal displaying a relatively low level of artifact (CAM B in (a)) show a reduction in sizes of vessels in (c) versus (b), which may indicate reduced blooming artifacts. Images from an animal with a relatively high level of artifact (CAM D in (a)) show a much-improved visualization of the vascular network when processed using our two-stage method (e) versus images exported from the scanner (d).

Table 5-2: The number and mean diameter measurements of vessels of different orders used in this study.

| Vessel order | Arteries | | Veins | | Diameter Range (μm) |
|--------------|--------------|-------------------------------------------|--------------|-------------------------------------------|----------------------------------|
| | # of vessels | mean diameter \pm SEM (μm) | # of vessels | mean diameter \pm SEM (μm) | |
| 4 | 0 | N/A | 0 | N/A | 140-200 |
| 5 | 0 | N/A | n=1 | 209.0 | 200-280 |
| 6 | n=10 | 367.1 \pm 82.1 | n=18 | 361.8 \pm 45.6 | 280-390 |
| 7 | n=11 | 448.0 \pm 61.3 | n=20 | 458.4 \pm 54.0 | 390-550 |
| 8 | n=3 | 514.0 \pm 43.6 | n=14 | 605.3 \pm 69.0 | 550-780 |
| 9 | n=2 | 656.5 \pm 14.5 | n=4 | 885.0 \pm 70.8 | 780-1098 |

* all diameter ranges calculated using diameter ranges from first to third orders vessels from [38] and the rule for diameter fractions between different orders from [39].

Diameter measurements using both Doppler methods were highly correlated with measurements from the optical photographs of the CAM. Measurements using images processed using our two-stage method showed slightly higher correlation ($r=0.82$, $p<0.0001$) than measurements from the Vevo 2100 exported images ($r=0.73$, $p<0.0001$) and the correlation coefficients were significantly different ($p<0.026$) using Steiger's Z-test.

In terms of overall diameter measurement accuracy, the two-stage method had a median absolute percentage error (MAPE) of 10.39%, which is almost half the MAPE computed from exported Vevo 2100 images of 28.18%. Errors computed by applying the two different processing methods were significantly different over all 83 vessel measurements ($p<0.001$). The distribution of these errors is illustrated by the histogram

in Figure 5-6. It is clear from the histogram that both methods resulted in some over- and underestimations of vessel diameters with more occurrences of overestimation than underestimation. Nevertheless, the distribution of errors using the two-stage method exhibits a narrow peak at 0% and a lower histogram tail at large positive error, indicating that applying the method frequently resulted in a more accurate estimate of the vessel diameter. In contrast, the histogram of errors resulting from images processed using commercial scanner software (Vevo 2100) had a wider peak centered at approximately 30% indicating the tendency of the images to depict blurred vessel boundaries that lead to overestimation of vessel diameters.

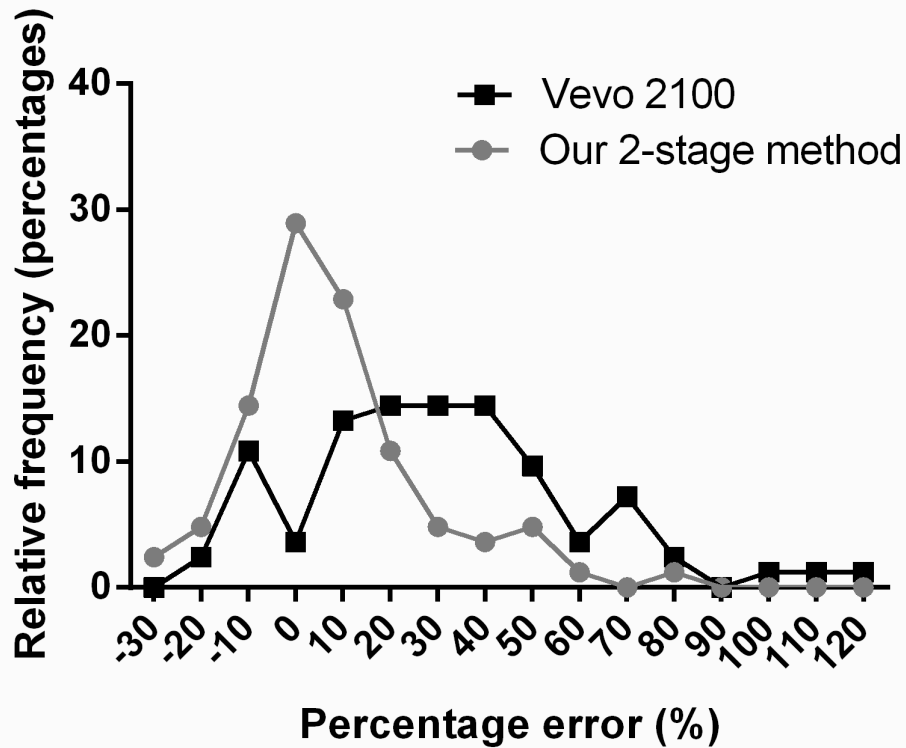


Figure 5-6: Comparison of the distributions of diameter measurement percentage errors from all 83 vessels used in this study from images processed using the two-stage method versus exported images from the commercial scanner (Vevo 2100).

When analyzing the performance of the two methods based on the type of vessel, the two-stage method resulted in lower MAPE estimates than Vevo 2100 processing for both arteries and veins (8.95% versus 30.55% and 11.07% versus 23.61%, respectively). The errors computed from 26 arteries and 57 veins were statistically significant ($p < 0.0001$ for each vessel type). The distribution of these errors is demonstrated by the histograms in Figure 5-7. Both types of vessels show similar ranges of overestimation and underestimation of vessel diameters using the two processing methods. However, the difference between the positions of the histogram peaks for the two methods appears to be dependent on the vessel type. For veins (Figure 5-7(b)), the shapes of the error histograms and the position of their peaks (close to 0%) are very similar whereas, for arteries (Figure 5-7(a)), the error distribution using the two-stage method appears to be centered at 0% while the peak of the distribution using Vevo2100 images appears shifted towards 30%.

The evaluation of the performance of the processing methods based on different vessel types and orders is illustrated in Figure 5-8. The improved accuracy provided by the two-stage method versus the commercial scanner processing, which was previously expressed in the overall mean errors, can still be observed for the different vessel orders as shown by the smaller ranges of error (length of the boxes) and lower median errors (midlines of the boxes) in Figure 5-8. In terms of variations based on vessel size, it can be observed that, for veins, the error decreases as the vessel diameter increases (*i.e.* as the vessel order increases). In addition, for larger vessels (order 8 arteries, order 8 and 9 veins), it is noticed that a larger fraction of the plots extend below the 0% line, indicating an underestimation of diameters. Images processed using the two-stage method appear to experience this underestimation more prominently than the exported Vevo 2100 images.

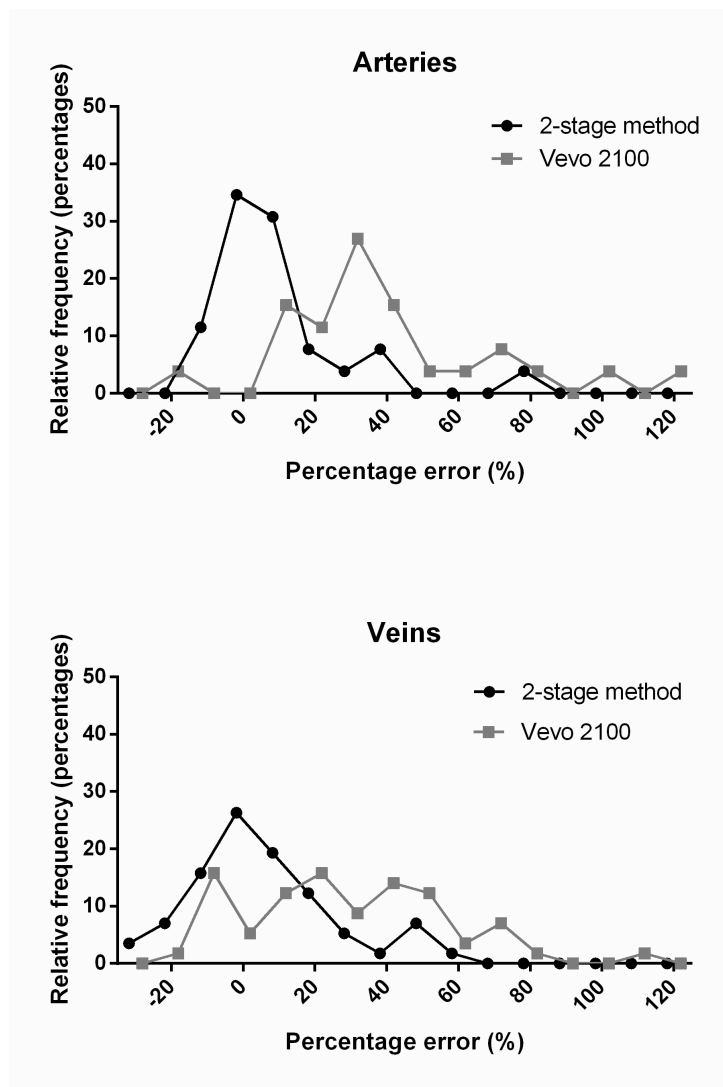


Figure 5-7: Separate comparisons of the distributions of diameter measurement percentage errors for (a) arteries and (b) veins from images processed using the two-stage method versus exported images from the commercial scanner (Vevo 2100).

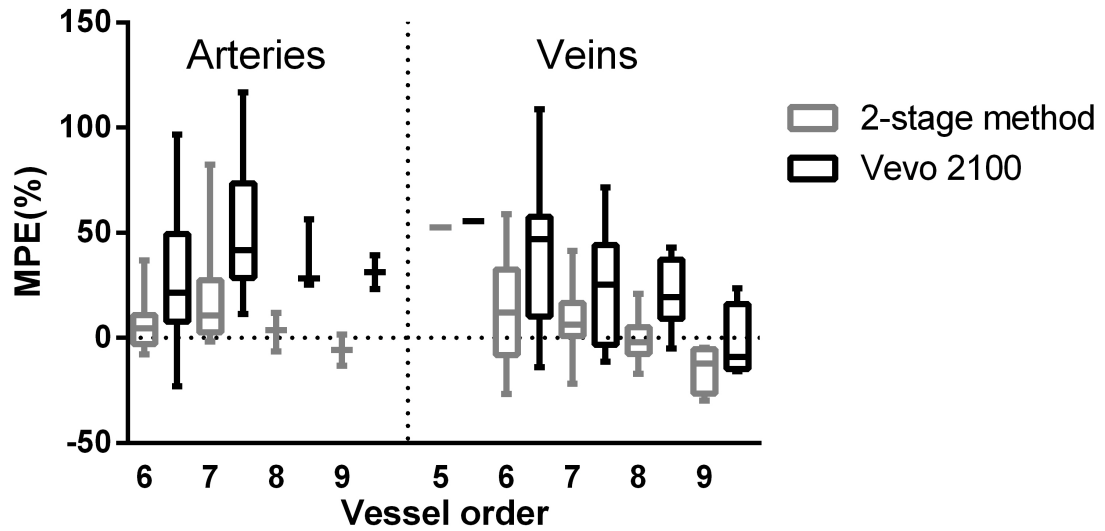


Figure 5-8: Box plot evaluation of the performance of the two-stage methods versus the commercial scanner (Vevo 2100) processing based on different vessel types and orders. For each vessel order, the whiskers display the minimum to maximum percentage error and the line within each box corresponds to the median error.

5.4 Discussion

The performance of the previously developed two-stage Doppler processing method [23] is evaluated for the use in vascular flow depiction applications by analyzing its effect on vessel detection, artifact reduction and diameter measurement accuracy. The chicken embryo chorioallantoic membrane (CAM) model, which is characterized by its simple, regularly distributed vascular network, was specifically selected for this study to allow more in-depth analysis of the proposed method and to provide a straightforward reference for validation using the optical images of the CAM.

The two-stage method improved detection of vessels that required a lower cut-off frequency than the optimum frequency for large vessels within the same frame. For example, the subregion enclosing the two vessels marked by white arrows in Figure 5-3(b) was automatically assigned a cut-off frequency of $0.06f_{\max}$ (where $f_{\max} = 0.5\text{PRF}$),

whereas the subregion enclosing the larger vessel was assigned a higher cut-off frequency of $0.39f_{\max}$. This was achieved by the spatial tuning of the cut-off frequency provided by the wall filter selection curve method based on the Doppler signal characteristics of vessels within the subregion. In other cases, the spatial tuning of the cut-off frequency helped improve the signal strength of successfully detected vessels such as the vessels marked by the white arrows in the lower panels (c and d) of Figure 5-3. The subregions enclosing these vessels were assigned lower cut-off frequencies ($0.25f_{\max}$ and $0.28f_{\max}$) than the cut-off frequency assigned to the subregion enclosing the bigger vessels ($0.87f_{\max}$). In this case, the lower cut-off frequency improved the power signal profile by increasing the sensitivity to signal variations within individual vessels, which is displayed as the gradual change of color within the vessels shown in Figure 5-3(d) instead of a single color corresponding to weak signal intensity (Figure 5-3(c)). The gradual decrease in signal intensity from the center of the vessel to the vessel walls has been reported in other studies to be a property of the power signal at a suitable gain setting [19]. Analyzing and understanding the relationship between the shape of the WFSCs and the type, velocity and signal intensity profile of blood flow within vessels enclosed in the corresponding subregion is a potential topic for further investigation.

By comparing vessel orders that were detected solely in images processed using the two-stage method and vessels that were common to the two sets of images (Tables 5-1 and 5-2), it is evident that the two-stage method allowed the detection of one vessel order lower than what was detected using the commercial scanner software. This may indicate that the proposed processing method improved the detection range of power Doppler mode using the Vevo 2100 scanner from vessels of diameters $> 200 \mu\text{m}$ to vessels as small as $140 \mu\text{m}$.

The improved detection of vessels in the 2-D frames was also translated to the overall 3-D view of the vessel network (Figure 5-4). The spatial tuning provided by the WFSC had the bigger role in depicting vessels that were not shown on the commercial scanner images (Figure 5-4 (a and b)), whereas the 3-D skeletonization method was particularly useful for extracting continuous vessel segments from artifact-obscured areas within the 3-D image (Figure 5-4(c and d)), resulting in an overall improvement in vessel

depiction. An additional advantage of the spatial tuning provided by the WFSC method is the reduction of blooming artifact (illustrated by the reduced diameters of vessels in Figures 5-4(b) and 5-5(b) in vessels for which the single cut-off frequency used in the Vevo 2100 images may be lower than the optimum cut-off, causing the exaggerated diameter as color bleeds outside the vessel. This assumption is later validated by the higher accuracy of diameter measurements (Section 5.3.3) from images processed using the two-stage method in comparison to images exported from the commercial scanner.

The main artifact in all Doppler images in this study is the jail-bar artifact. This artifact is known to be directly linked to the presence of a strong reflector in the range of the penetration depth provided by the imaging system [40]. The strong reflector signals result in saturation of some lines in the ROI, resulting in the appearance of stripes. The continuity of the jail-bar stripes along the elevation axis of 3-D image may be resulting from vibrations of the 3-D motor while stepping the transducer through the imaged volume. The jail-bar artifact is not typically reported as a common power Doppler artifact due to the specific setup needed for it to exist. However, Martins et al. reported the existence of vertical lines in power Doppler images of a water tank that disappeared when a 2 cm piece of bovine tissue was placed on the base of the tank causing attenuation of the reflected signals [40]. Another factor that may contribute to the severity of this artifact in the images is the nature of the CAM microcirculation. The CAM is characterized by having a superficial, very dense capillary mesh, which is supplied and drained by free-floating medium and large vessels [41]. Due to the limited resolution of ultrasound system, this capillary mesh would not be resolved and would appear as a blush of power signal above the vascular network, such as the obscuring layer of colored pixels illustrated in the lower panels (c and d) of Figure 5-5.

Using the average number of colored voxels in each elevation line within a 3-D image to quantify the image artifact was inspired by the work of Jamzad et al. [42], who used a similar approach to quantify twinkling artifacts in color Doppler images. In the case, as the number of stripes within an image increased, more elevation lines were almost fully formed of colored voxels, which shifted the mean number of colored voxels to a higher value indicating a high level of artifact.

The artifact-reduction effect of the two-stage method was particularly useful in images with high levels of artifact, such as the images of CAM D (Figure 5-5 (c and d)). Each of the two components of the method contributed in reducing these artifacts. The WFSC method helps by eliminating signals in subregions that do not form a meaningful selection curve (*i.e.*, a curve in which the CPD decreases gradually with increasing cut-off frequency) corresponding to the absence of the gradually changing power profile (illustrated in Figure 5-3) typically displayed for blood vessels in subregions enclosing these artifacts. Likewise, since the stripes do not form a connected 3-D structure similar to the vessel segments, the 3-D skeletonization method is able to discard most of them, resulting in an improved view of the vascular network such as the one shown in Figure 5-5(d).

The improved vessel detection and artifact (blooming and jail-bar) reduction using the two-stage method can be considered the key factors in improving the overall correlation and accuracy of diameter measurements to the reference optical images. The few over- and underestimations of the vessel diameter (shown by the end points of the histograms in Figure 5-6) may be attributed to the different resolutions in the three main directions (axial: 40 μm , lateral: 80 μm [43], and elevation: 180 μm based on an elevation f-number of 4.7 [44]), which affects the accuracy of the measurements depending on the orientation of the vessel. Similar reports of the inaccuracy of diameter measurements using different view windows of the vessels due to the different resolutions in Doppler images were found in the literature [45, 46]. Understanding the extent and effect of these resolution differences on the performance of the proposed two-stage method may be further investigated using the CAM microvasculature.

In addition to the improved overall accuracy of diameter measurements, having the peak of the two-stage method's histogram of estimation errors centered at 0% with a relatively narrow range (Figure 5-6) is a very good indication of its potential to reduce the consistently reported overestimation of power Doppler diameter measurements in clinical or preclinical studies [47, 48]. This frequently reported overestimation is expressed in the histogram of Vevo 2100 data by the shifted peak of the distribution at 30%. In this study, this error shift may have resulted from the need of the licensed

sonographer to select a relatively low cut-off frequency (causing more blooming in big vessels) to maintain signals from weak vessels, which were obscured by the strong reflections from the base, instead of losing their signal by applying a higher cut-off. This assumption is further supported by the differences between the error distributions in arteries and veins. As shown in Figure 5-7, the performance of the two processing methods is more similar in the case of measurements from venular networks (Figure 5-7(b)), while the histogram of errors from arterial network (Figure 5-7(a)) resembles the overall error histogram. This distinction between the methods' error distributions for arteries versus veins can be due to the pulsatile nature of the arteries that results in varying representations of a vessel diameter depending on the time point during the cardiac cycle at which a frame was acquired. These varying representations of vessel diameter would result in overestimation or underestimation of the diameter measurement depending on the wall filter cut-off setting in a typical instrument processing software and therefore, would particularly benefit from tuning the wall filter cut-off frequency based on their flow properties in the processed image. Therefore, the two-stage method can be of more value in studies involving measurements of the arterial network.

The deeper analysis of the methods' performance for vessels of different type and size is helpful for understanding the abstract performance measures represented by the MAPE and the error distributions discussed earlier. The inverse relationship between the amount of error and vessel size (Figure 5-8) is expected, since diameter measurements of smaller vessels require higher resolution and accuracy and thus can suffer from overestimation more frequently. This is a customary observation in studies that use power Doppler to measure different levels of stenosis and report that the measurement accuracy decreases with stenosis severity (*i.e.* smaller diameters) [4, 49]. On the other hand, the consistent underestimation of larger vessel diameters (order 8 arteries, order 8 & 9 veins in Figure 5-8) may reflect a tendency of the two-stage method to select a higher than optimum cut-off frequency in cases when the velocity in the vessels is very high such that the WFSC curve extends to a value close to the system's maximum velocity limit ($f_{\max} = 0.5\text{PRF}$) without the CPD decreasing to zero. This may affect the efficacy of the WFSC method to accurately define the end point of the characteristic interval and, accordingly, the optimum cut-off selection. Further analysis of the performance of the method with

larger, fast flow vessels and attempting to use different PRFs to match flow velocities within different subregions of the image may improve the accuracy of the cut-off selection. Finally, the consistently lower median error and smaller range of errors using the two-stage method for all studied vessel types and sizes is a strong indication of the potential of the proposed processing method to improve the accuracy of microvascular diameter measurements using 3-D power Doppler.

5.5 Conclusion

We presented a new power Doppler signal processing method that involves an automated, spatially tuned selection of the wall filter cut-off frequency instrument setting and an image post-processing algorithm to extract 3-D vascular networks. We evaluated the method's performance using a chick embryo CAM model. In comparison to images processed using commercial scanner software, the method showed improved depiction and detection of vessels in 2-D and 3-D images. It helped reduce the level of artifact in the images allowing improved visualization of the imaged vasculature. Most importantly, it increased the accuracy of diameter measurements for arterial and venous vessels of different sizes. Overall, the proposed method shows promising results for improving the usability of 3-D power Doppler imaging in flow depiction applications such as assessment of stenotic structures or analyzing the morphology of a 3-D vascular network.

References

- [1] J. M. Rubin, R. O. Bude, P. L. Carson, *et al.*, "Power Doppler Us - a Potentially Useful Alternative to Mean Frequency-Based Color Doppler Us," *Radiology*, vol. 190, pp. 853-856, 1994.
- [2] J. M. Wardlaw, J. C. Cannon, and R. J. Sellar, "Use of Color Power Transcranial Doppler Sonography to Monitor Aneurysmal Coiling," *AJNR Am J Neuroradiol*, vol. 17, pp. 864-867, 1996.
- [3] P. M. White, J. M. Wardlaw, E. Teasdale, *et al.*, "Power Transcranial Doppler Ultrasound in the Detection of Intracranial Aneurysms," *Stroke*, vol. 32, pp. 1291-1297, 2001.
- [4] B. Griewing, C. Morgenstern, F. Driesner, *et al.*, "Cerebrovascular Disease Assessed by Color-Flow and Power Doppler Ultrasonography. Comparison with Digital Subtraction Angiography in Internal Carotid Artery Stenosis," *Stroke*, vol. 27, pp. 95-100, 1996.
- [5] S. O. Oktar, C. Yücel, D. Karaosmanoglu, *et al.*, "Blood-Flow Volume Quantification in Internal Carotid and Vertebral Arteries: Comparison of 3 Different Ultrasound Techniques with Phase-Contrast Mr Imaging," *AJNR Am J Neuroradiol*, vol. 27, pp. 363-369, 2006.
- [6] W. A. Schmidt, "Technology Insight: The Role of Color and Power Doppler Ultrasonography in Rheumatology," *Nat Clin Pract Rheumatol*, vol. 3, pp. 35-42; quiz 59, 2007.
- [7] R. J. Wakefield, A. K. Brown, P. J. O'Connor, *et al.*, "Power Doppler Sonography: Improving Disease Activity Assessment in Inflammatory Musculoskeletal Disease," *Arthritis Rheum*, vol. 48, pp. 285-288, 2003.
- [8] D. J. Rubens, S. Bhatt, S. Nedelka, *et al.*, "Doppler Artifacts and Pitfalls," *Radiol Clin North Am*, vol. 44, pp. 805-835, 2006.
- [9] K. Mizushige, T. Ueda, M. Yuba, *et al.*, "Dependence of Power Doppler Image on a High Pass Filter Instrumented in Ultrasound Machine," *Ultrasound Med Biol*, vol. 25, pp. 1389-1393, 1999.
- [10] D. Garcia, M. Fenech, Z. Qin, *et al.*, "Signal Losses with Real-Time Three-Dimensional Power Doppler Imaging," *Ultrasound Med Biol*, vol. 33, pp. 1632-1639, 2007.
- [11] E. Quaia and SpringerLink (Online service), *Radiological Imaging of the Kidney*. Berlin, Heidelberg: Springer-Verlag Berlin Heidelberg, 2011.

- [12] R. B. Peterson, L. E. Atlas, and K. W. Beach, "A Comparison of Iir Initialization Techniques for Improved Color Doppler Wall Filter Performance," in *Ultrasonics Symposium, 1994. Proceedings., 1994 IEEE*, pp. 1705-1708 vol.1703, Oct. 31 1994-Nov. 3 1994.
- [13] S. Bjaerum, H. Torp, and K. Kristoffersen, "Clutter Filter Design for Ultrasound Color Flow Imaging," *IEEE Trans Ultrason Ferroelectr Freq Control*, vol. 49, pp. 204-216, 2002.
- [14] D. E. Kruse and K. W. Ferrara, "A New High Resolution Color Flow System Using an Eigendecomposition-Based Adaptive Filter for Clutter Rejection," *IEEE Trans Ultrason Ferroelectr Freq Control*, vol. 49, pp. 1739-1754, 2002.
- [15] Y. M. Yoo and Y. Kim, "New Adaptive Clutter Rejection for Ultrasound Color Doppler Imaging: In Vivo Study," *Ultrasound Med Biol*, vol. 36, pp. 480-487, 2010.
- [16] S. Z. Pinter and J. C. Lacefield, "Detectability of Small Blood Vessels with High-Frequency Power Doppler and Selection of Wall Filter Cut-Off Velocity for Microvascular Imaging," *Ultrasound in medicine & biology*, vol. 35, pp. 1217-1228, 2009.
- [17] S. Z. Pinter and J. C. Lacefield, "Objective Selection of High-Frequency Power Doppler Wall Filter Cutoff Velocity for Regions of Interest Containing Multiple Small Vessels," *IEEE Transactions on Medical Imaging*, vol. 29, pp. 1124-1139, 2010.
- [18] M. Elfarnawany, S. Z. Pinter, and J. C. Lacefield, "Improved Objective Selection of Power Doppler Wall-Filter Cut-Off Velocity for Accurate Vascular Quantification," *Ultrasound in medicine & biology*, vol. 38, p. 1429, 2012.
- [19] T. Schlosser, C. Pohl, S. Kuntz-Hehner, *et al.*, "Echoscintigraphy: A New Imaging Modality for the Reduction of Color Blooming and Acoustic Shadowing in Contrast Sonography," *Ultrasound Med Biol*, vol. 29, pp. 985-991, 2003.
- [20] Y. C. Lai, Y. S. Huang, D. W. Wang, *et al.*, "Computer-Aided Diagnosis for 3-D Power Doppler Breast Ultrasound," *Ultrasound Med Biol*, vol. 39, pp. 555-567, 2013.
- [21] M. Elfarnawany and J. C. Lacefield, "A New Three-Component Signal Model to Objectively Select Power Doppler Wall Filter Cut-Off Velocity for Quantitative Microvascular Imaging," in *SPIE, Medical Imaging 2013: Ultrasonic Imaging, Tomography, and Therapy*, Florida, USA, p. 86750J.
- [22] S. Z. Pinter, D.-R. Kim, M. N. Hague, *et al.*, "A Method to Validate Quantitative High-Frequency Power Doppler Ultrasound with Fluorescence in Vivo Video Microscopy," *Ultrasound in medicine & biology*, vol. 40, pp. 1908-1917, 2014.

- [23] M. Elfarnawany, M. R. Lowerison, M. N. Hague, *et al.*, "In Vivo Evaluation of an Objective Method to Select Power Doppler Wall Filter Cut-Off Frequency for Microvascular Quantification," in *Ultrasonics Symposium (IUS), 2014 IEEE International*, pp. 436-439, 3-6 Sept. 2014.
- [24] H. S. Leong, N. F. Steinmetz, A. Ablack, *et al.*, "Intravital Imaging of Embryonic and Tumor Neovasculature Using Viral Nanoparticles," *Nat Protoc*, vol. 5, pp. 1406-1417, 2010.
- [25] D. H. Ausprunk, D. R. Knighton, and J. Folkman, "Differentiation of Vascular Endothelium in the Chick Chorioallantois: A Structural and Autoradiographic Study," *Dev Biol*, vol. 38, pp. 237-248, 1974.
- [26] B. Fenton and B. W. Zweifach, "Microcirculatory Model Relating Geometrical Variation to Changes in Pressure and Flow Rate," *Annals of Biomedical Engineering*, vol. 9, pp. 303-321, 1981.
- [27] S. Blacher, L. Devy, R. Hlushchuk, *et al.*, "Quantification of Angiogenesis in the Chicken Chorioallantoic Membrane (Cam)," *IAS*, vol. 24, pp. 169-180, 2005.
- [28] D. Marr and E. Hildreth, "Theory of Edge Detection," *Proceedings of the Royal Society of London B: Biological Sciences*, vol. 207, pp. 187-217, 1980.
- [29] D. Prodanov, "Mexican Hat Filter Plugin for Imagej," ed. <http://rsb.info.nih.gov/ij/plugins/mexican-hat/index.html>, 2012.
- [30] A. G. Shanbhag, "Utilization of Information Measure as a Means of Image Thresholding," *CVGIP*, vol. 56, pp. 414-419, 1994.
- [31] D. Kruse, R. Silverman, S. Erickson, *et al.*, "Optimization of Real-Time High Frequency Ultrasound for Blood Flow Imaging in the Microcirculation," in *Ultrasonics Symposium, 2000 IEEE*, pp. 1461-1464, Oct 2000.
- [32] K. S. Park, B. I. Choi, H. J. Won, *et al.*, "Intratumoral Vascularity of Experimentally Induced Vx2 Carcinoma: Comparison of Color Doppler Sonography, Power Doppler Sonography, and Microangiography," *Invest Radiol*, vol. 33, pp. 39-44, 1998.
- [33] R. O. Bude, J. M. Rubin, and R. S. Adler, "Power Versus Conventional Color Doppler Sonography: Comparison in the Depiction of Normal Intrarenal Vasculature," *Radiology*, vol. 192, pp. 777-780, 1994.
- [34] K. Palàgyi and A. Kuba, "A 3d 6-Subiteration Thinning Algorithm for Extracting Medial Lines," *Pattern Recognit Lett*, vol. 19, pp. 613-627, 1998.
- [35] R. Auerbach, L. Kubai, D. Knighton, *et al.*, "A Simple Procedure for the Long-Term Cultivation of Chicken Embryos," *Dev Biol*, vol. 41, pp. 391-394, 1974.

- [36] J. H. Steiger, "Tests for Comparing Elements of a Correlation Matrix," *Psychol Bull*, vol. 87, pp. 245-251, 1980.
- [37] I. A. Lee and K. J. Preacher, "Calculation for the Test of the Difference between Two Dependent Correlations with One Variable in Common," ed. <http://quantpsy.org/corrtest/corrtest2.htm>., 2013.
- [38] D. O. DeFouw, V. J. Rizzo, R. Steinfeld, *et al.*, "Mapping of the Microcirculation in the Chick Chorioallantoic Membrane During Normal Angiogenesis," *Microvasc Res*, vol. 38, pp. 136-147, 1989.
- [39] M. B. Vickerman, P. A. Keith, T. L. McKay, *et al.*, "Vesgen 2d: Automated, User-Interactive Software for Quantification and Mapping of Angiogenic and Lymphangiogenic Trees and Networks," *Anat Rec (Hoboken)*, vol. 292, pp. 320-332, 2009.
- [40] W. P. Martins, N. J. Raine-Fenning, R. A. Ferriani, *et al.*, "Quantitative Three-Dimensional Power Doppler Angiography: A Flow-Free Phantom Experiment to Evaluate the Relationship between Color Gain, Depth and Signal Artifact," *Ultrasound Obstet Gynecol*, vol. 35, pp. 361-368, 2010.
- [41] A. Fuchs and E. S. Lindenbaum, "The Two- and Three-Dimensional Structure of the Microcirculation of the Chick Chorioallantoic Membrane," *Acta Anat (Basel)*, vol. 131, pp. 271-275, 1988.
- [42] A. Jamzad and S. K. Setarehdan, "A Novel Approach for Quantification and Analysis of the Color Doppler Twinkling Artifact with Application in Noninvasive Surface Roughness Characterization: An in Vitro Phantom Study," *J Ultrasound Med*, vol. 33, pp. 597-610, 2014.
- [43] VisualSonics, "Visualsonics Vevo Imaging System User Manual," 1.0 ed: FUJIFILM VisualSonics, Inc., 2012.
- [44] F. S. Foster, J. Mehi, M. Lukacs, *et al.*, "A New 15–50 Mhz Array-Based Micro-Ultrasound Scanner for Preclinical Imaging," *Ultrasound Med Biol*, vol. 35, pp. 1700-1708, 2009.
- [45] S. H. Little, B. Pirat, R. Kumar, *et al.*, "Three-Dimensional Color Doppler Echocardiography for Direct Measurement of Vena Contracta Area in Mitral Regurgitation: In Vitro Validation and Clinical Experience," *JACC Cardiovasc Imaging*, vol. 1, pp. 695-704, 2008.
- [46] D. Y. Or, M. K. Karmakar, G. C. Lam, *et al.*, "Multiplanar 3d Ultrasound Imaging to Assess the Anatomy of the Upper Airway and Measure the Subglottic and Tracheal Diameters in Adults," *Br J Radiol*, vol. 86, p. 20130253, 2013.

- [47] Z. Guo and A. Fenster, "Three-Dimensional Power Doppler Imaging: A Phantom Study to Quantify Vessel Stenosis," *Ultrasound Med Biol*, vol. 22, pp. 1059-1069, 1996.
- [48] M. Claudon, D. Waininger, S. Briançon, *et al.*, "Power Doppler Us: Evaluation of the Morphology of Stenoses with a Flow Phantom," *Radiology*, vol. 218, pp. 109-117, 2001.
- [49] G. Cloutier, Z. Qin, D. Garcia, *et al.*, "Assessment of Arterial Stenosis in a Flow Model with Power Doppler Angiography: Accuracy and Observations on Blood Echogenicity," *Ultrasound Med Biol*, vol. 26, pp. 1489-1501, 2000.

Chapter 6

Summary and Future Work

6.1 Summary

Vascular imaging and quantification, typically called angiography, is becoming a core need for almost all clinical and research application involving pathology diagnosis, treatment and surgical interventions. Ultrasound stands its position as a valuable vascular imaging technique with its low cost, lack of ionizing radiation and being the non-invasive. Doppler ultrasound flow imaging techniques provide a wealth of information about vascular characteristics that can be presented using a number of different display modes. Power Doppler is characterized by its ability to image small vessels with slow flow, which makes it particularly useful as a vascular quantification tool. However, the sensitivity to operator-dependent instrument settings and the likelihood of image artifacts are challenges for quantitative power Doppler imaging. Therefore, development of new signal processing methods to overcome some of these challenges can enhance the usability of power Doppler imaging in quantitative microvascular angiography.

6.1.1 Chapter 2: Improved objective selection of power Doppler wall-filter cut-off velocity for accurate vascular quantification

An improved (relative to the original method presented in[1]) automatic, objective method for the selection of one of the ultrasound operator-depend instrument settings, namely, the wall filter cut-off frequency is presented. The method, called the wall filter selection curve (WFSC) method has three key features: first, it automatically identifies the cut-off frequency ranges enclosing the optimum cut-off frequency based on the characteristics of the imaged vasculature, secondly, using a multi-step decision algorithm, the method identifies an operating point within these ranges. Finally, using the first and second features, the method performs spatial tuning of the cut-off frequency by selecting a cut-off frequency for subregions within a region of interest. Evaluation the WFSC method using multiple-vessel flow phantom images demonstrated the improved depiction

of blood-mimicking fluid flow with smoother and sharper vessel boundaries in comparison to images processed and displayed using typical commercial scanner software. Vascular quantification of images processed using the improved WFSC method was accurate to within 3% of the vascular volume fraction of the phantom.

6.1.2 Chapter 3: A new three-component signal model to objectively select power Doppler wall filter cut-off velocity for quantitative microvascular imaging

Building on the theoretical basis of the WFSC method presented in Chapter 2 and using experimental WFSCs from flow-phantom images, a new signal model describing the relationship between wall filter cut-off frequency and the ratio of colored pixels displayed in a power Doppler image (color pixel density (CPD)) was developed. The new model showed an improved fit to experimental flow-phantom selection curves in comparison to the original theoretical model developed in [1]. Monte Carlo simulations of different vascular environments by changing the number of vessels and the mean and standard deviation of blood and background tissue velocity distributions in conjunction with reference values derived using a cost function were used to analyze the performance of the WFSC method to automatically select an operating cut-off frequency. These simulations were also used to identify conditions necessary for the development of an online implementation of the WFSC method including the reliable number of samples on a selection curve (100 samples) and the upper limit to fluctuations to CPD within a region of interest (5% of reference vascular volume fraction), the length of a reliable characteristic interval (longer than 6mm/s) and the threshold for the starting cut-off velocity of an interval is set to 3 mm/s. Evaluation of the accuracy of cut-off selection using reference values from the cost function supported the satisfactory performance of the multi-step decision algorithm for operating cut-off frequency selection developed in Chapter 2. This theoretical analysis was necessary to establish the expectation that the WFSC method can improve the accuracy and reproducibility of power Doppler for quantitative microvascular imaging by adapting the cut-off frequency to spatial and temporal variations in blood conditions.

6.1.3 Chapter 4: A two-stage process to improve quantitative three-dimensional power Doppler angiography of tumor microvasculature

A three-dimensional vascular network reconstruction method was developed and combined with the improved WFSC method from Chapters 2 and 3 to present a two-stage power Doppler processing method targeted at improving the quantitative performance of power Doppler angiography. Evaluated using power Doppler images of a murine tumor model, the two-stage method showed improved visualization of the vascular network. Quantifying vasculature using power Doppler angiography indices (vascularization index, flow index and vascularization flow index (VFI)) showed significant variations when images processed using the two-stage method were compared to images processed using typical, fixed wall filter cut-off frequency without vascular network reconstruction. Small improvements in correlation of the power Doppler angiography metric, VFI, with contrast-enhanced ultrasound image quantification over typical Doppler-processing images were reported. The first *in vivo* evaluation of the performance of the improved WFSC method (Chapter 2) demonstrated the relevance of spatially and temporally adjusting the cut-off frequency within a 3-D image as the mean WFSC-selected cut-off showed large variation within each 3-D image, and among images acquired at different time points across different animals (two-way ANOVA, $p < 0.0001$). The vascular feature responsible for these variations of cut-off frequency selection was identified as the ratio between total vascular length and vascular volume. These results suggest that the two-stage process has the potential to improve the reliability of visualization and quantification of complex, dense vasculature using 3-D power Doppler angiography.

6.1.4 Chapter 5: Improving microvascular depiction in three-dimensional power Doppler ultrasound using a two-stage processing method

The two-stage method developed in Chapter 4 was evaluated using an *in vivo* model of the chicken embryo chorioallantoic membrane as a vascular depiction application of power Doppler imaging. Applying the two-stage method to power Doppler signal data improved vessel detection and visualization and resulted in significant image artifact reduction in comparison to images processed using a commercial scanner software and set up by a licensed sonographer. Vessel diameter measurements from

images processed using the two-stage method were more accurate than measurements made using raw images exported from the commercial scanner (with a median absolute percentage error = 10.39% versus 28.18% respectively). Further analysis of the types and orders of vessels contributing to the overall error showed that higher errors in diameter measurements were associated with vessels of lower orders (orders 6 and 7, which have diameters of approximately 280 to 550 μm). It was also shown that a diameter overestimation bias of approximately 30% was observed for arterial diameter measurements using scanner exported images whereas measurement errors from the two-stage method images were centered at 0%. Thus, the proposed method shows promising results for improving vascular quantification, detection and visualization using 3-D power Doppler imaging suitable for flow depiction applications.

6.2 Future Work

The ultimate goal of this project is to have an online implementation of the developed methods in a commercial ultrasound scanner. Integrating these methods in typical Doppler processing software can provide improved visualization and quantification of imaged vasculature using power Doppler imaging while having the option of an automatic wall filter cut-off frequency setting, making it possible for non-specialist or time-sensitive operators, such as the users of portable scanners and preclinical scanners to reproducibly acquire diagnostic-quality, quantitatively accurate Doppler images.

There are some future direction paths to take in order to reach this ultimate goal. First, to further understand the relationship between properties of the wall filter selection curve (WFSC) such as its shape, range, number of detected intervals and the corresponding features of the imaged vasculature within a subregion, a study using the simple, organized vasculature of the chorioallantoic membrane (CAM) described in Chapter 5 can be setup in which WFSCs of subregions enclosing vessels with known characteristics (type, order, blood velocity) are analyzed. Having this clear connection

between vascular features and properties of the WFSC can help improve the operating cut-off selection algorithm to improve the overall performance of the method.

Another future direction is to work on improving the currently developed methods and overcoming some of their limitations. One potential subject for improvement is developing two- and three-dimensional smoothing algorithms for the selected cut-off frequencies within an image to reduce fluctuations in representations of the different sections of the same vessel across multiple frames or subregions.

Furthermore, developing some supplemental tools to improve the usability of the currently developed methods is another step on the way to have an online implementation of the method. One example of a supplemental tool is developing vascular network analysis software similar to [2] that allows the user to perform diameter measurements or estimates of vascular density using the processed images. Using images from the CAM vasculature in Chapter 5, this tool is currently being designed in our lab by a summer student, which can later be integrated with the previously developed method to compute power Doppler angiography metrics presented in Chapter 4.

Finally, a future project investigating the feasibility of using the wall filter selection curve method to automatically select other operator-dependent instrument settings such as the pulse repetition frequency (PRF) or the priority settings. A suitable value of PRF can possibly be determined from the range of cut-off frequencies that yields non-zero color pixel density value indicating the maximum velocity of vasculature within a subregion. Similarly, the shape of the WFSC can be used to determine whether some pixels correspond to signal from moving blood or from a highly echogenic solid tissue which is typically eliminated using the priority setting.

6.3 Final Remarks

Three-dimensional power Doppler angiography is actively being pursued as reliable vascular quantification and visualization in many clinical applications. As an attempt to expand upon current state-of-the art signal processing methods in commercial ultrasound scanners, this thesis has pursued the development of power Doppler signal

processing methods that provide an automatic, spatially tuned selection of the wall filter cut-off frequency setting and apply image post-processing methods to reduce image artifacts and improve visualization of three-dimensional vascular networks. Since power Doppler imaging is already widely available in commercial ultrasound systems, it is hoped that the signal processing methods presented in this thesis can eventually be integrated into typical Doppler processing software on existing ultrasound systems. As a result, power Doppler imaging users can worry less about operator dependence of the wall-filter settings while experiencing the improved visualization and quantification of imaged vasculature for their flow depiction or quantification applications.

References

- [1] S. Z. Pinter and J. C. Lacefield, "Detectability of Small Blood Vessels with High-Frequency Power Doppler and Selection of Wall Filter Cut-Off Velocity for Microvascular Imaging," *Ultrasound Med Biol*, vol. 35, pp. 1217-1228, 2009.
- [2] M. B. Vickerman, P. A. Keith, T. L. McKay, *et al.*, "Vesgen 2d: Automated, User-Interactive Software for Quantification and Mapping of Angiogenic and Lymphangiogenic Trees and Networks," *Anat Rec (Hoboken)*, vol. 292, pp. 320-332, 2009.

Appendix A: Copyright Agreements

This thesis contains downloaded visual media (Chapter 1, Figure 1-5) from Medcyclopaedia website, a division of GE Healthcare providing electronic downloadable publications; scientific and medical data and information downloadable from the Internet [1]. GE HEALTHCARE does not require prior written permission if content is downloaded and printed, in whole or in part, for uses that are not competitive with or derogatory to GE HEALTHCARE or its group, provided that all copyright or other proprietary notices intact are kept intact [2].

This thesis also contains material from previously published manuscripts in Elsevier, *Ultrasound in Medicine and Biology* (Chapter 2) and *SPIE Conference Proceedings* (Chapter 3). Elsevier, *Ultrasound in Medicine and Biology* [3] and *SPIE* [4] do not require that the author of a publication receive copyright permission for duplication of the published article for the purpose of a thesis or dissertation, as long as the source of the material is properly referenced. Appropriate reference to the published sources is given in the co-authorship section.

- [1] Medcyclopaedia Trade-Mark (word), Canadian trade-mark data, Canadian Intellectual Property Office. <http://www.ic.gc.ca>
- [2] Medcyclopaedia Terms of Use, www.medcyclopaedia.com
- [3] Elsevier. (2015). *Elsevier Copyright Information, Journal Author Rights*. Available: <http://www.elsevier.com/about/company-information/policies/copyright>
- [4] SPIE. (2015). *Spie Reprint Permissions, authors Reproducing Their Own Spie Material*. Available: <http://spie.org/x1125.xml>

Appendix B: Ethics Approval for Animal Subjects

Fwd: eSirius Notification - New Animal Use Protocol is APPROVED2... imap://imap.uwo.ca:993/fetch>UID>/Animal protocols>4?header=.

>>> eSiriusWebServer <esiriusadmin@uwo.ca> 2013/12/10 2:00 PM >>>



AUP Number: 2009-072

PI Name: Chambers, Ann

AUP Title: Steps Of Breast Cancer Metastasis: Experimental Models And Identification Of Targets For Intervention

Approval Date: 12/10/2013

Official Notice of Animal Use Subcommittee (AUS) Approval: Your new Animal Use Protocol (AUP) entitled "Steps Of Breast Cancer Metastasis: Experimental Models And Identification Of Targets For Intervention

" has been APPROVED by the Animal Use Subcommittee of the University Council on Animal Care. This approval, although valid for four years, and is subject to annual Protocol Renewal.2009-072::5

1. This AUP number must be indicated when ordering animals for this project.
2. Animals for other projects may not be ordered under this AUP number.
3. Purchases of animals other than through this system must be cleared through the ACVS office. Health certificates will be required.

The holder of this Animal Use Protocol is responsible to ensure that all associated safety components (biosafety, radiation safety, general laboratory safety) comply with institutional safety standards and have received all necessary approvals. Please consult directly with your institutional safety officers.

Submitted by: Kinchlea, Will D
on behalf of the Animal Use Subcommittee
University Council on Animal Care

The University of Western Ontario
Animal Use Subcommittee / University Council on Animal Care
Health Sciences Centre, • London, Ontario • CANADA – N6A 5C1
PH: 519-661-2111 ext. 86768 • FL 519-661-2028
Email: auspc@uwo.ca • <http://www.uwo.ca/animal/website/>

This information is directed in confidence solely to the person named above and may contain confidential and/or privileged material. This information may not otherwise be distributed, copied or disclosed. If you have received this e-mail in error, please notify the sender immediately via a return e-mail and destroy original message. Thank you for your cooperation.

Curriculum Vitae

- Name:** Mai H. Elfarnawany
- Post-secondary Education and Degrees:** Western University
London, Ontario, Canada
2010-2015, Ph.D., Biomedical Engineering
Thesis: “Signal Processing Methods for Quantitative Power Doppler Microvascular Angiography”
Supervisor: Dr. James C. Lacefield
- Cairo University,
Cairo, Egypt
2004-2009 B.B.S.E., Biomedical Engineering Department
Graduation Project: “Enhanced A-scan Biometry system”
- Awards and Scholarships:** National Science and Engineering Research Council (NSERC)
Post Graduate Scholarship – D (PGS-D)
2012-2015
- Western Graduate Research Scholarship,
Western University,
2010-2015, Tuition Deferral
- Ontario Graduate Scholarship (OGS)
declined
2012
- 1st prize poster winner at the 10th Imaging Network Ontario Symposium (ImNO),
Toronto, ON,
2012
- Ontario Graduate Scholarship (OGS)
2011-2012
- Nominated for NSERC Vanier Canada Graduate Scholarship (VCGS) Award,
2011

2nd prize poster winner at the London Imaging Discovery (LID) Day Conference,
London, ON,
2010

First Ranking Graduation Award, Faculty of Engineering,
Cairo, Egypt,
2010

Information Technology Academia Collaboration (ITAC) Graduation Project Award, Information Technology Industry Development Agency (ITIDA) Egypt,
Cairo, Egypt,
2009

Young Innovators' Awards (YIA) Program,
Nahdet ElMahrousa,
Cairo, Egypt,
2009

Related Work Experience:

Teaching Assistant, Microprocessors and Microcomputers,
Department of Electrical and Computer Engineering,
Western University
Winter term, 2015

Teaching Assistant, Digital Logic Systems, Department of Electrical and Computer Engineering,
Western University
Fall term, 2013

Teaching Assistant, Digital Logic Systems, Department of Electrical and Computer Engineering,
Western University
Fall term, 2011

Teaching Assistant, Programming fundamentals for engineers,
Department of Electrical and Computer Engineering,
Western University
Winter term, 2011

Teaching Assistant, Discrete Structures for Software Engineers,
Department of Electrical and Computer Engineering,
Western University
Fall term, 2010

Refereed Journal Publications

M. Elfarnawany, N. Govindaraju, S. Pardhan, A. Makela, P. Foster, H. S. Leong, J. C. Lacefield, "Improving microvascular depiction in three-dimensional power Doppler ultrasound using a two-stage processing method," *IEEE Transactions on Medical Imaging*, 2015 (in preparation).

M. Elfarnawany, M. R. Lowerison, M. N. Hague, A. F. Chambers and J.C. Lacefield, "A two-stage process to improve quantitative three-dimensional power Doppler angiography of tumor microvasculature," *Ultrasound in Medicine and Biology*, 2015 (in preparation).

M. Elfarnawany, S. Z. Pinter, and J. C. Lacefield, "Improved Objective Selection of Power Doppler Wall-Filter Cut-Off Velocity for Accurate Vascular Quantification," *Ultrasound in Medicine & Biology*, vol. 38, p. 1429, 2012.

Refereed Conference Proceedings

M. Elfarnawany, M. R. Lowerison, M. N. Hague, *et al.*, "In Vivo Evaluation of an Objective Method to Select Power Doppler Wall Filter Cut-Off Frequency for Microvascular Quantification," in *Ultrasonics Symposium (IUS), 2014 IEEE International*, pp. 436-439, 3-6 Sept. 2014.

M. Elfarnawany and J. C. Lacefield, "A New Three-Component Signal Model to Objectively Select Power Doppler Wall Filter Cut-Off Velocity for Quantitative Microvascular Imaging," in *SPIE*, 2013, article 86750J.

Refereed Conference Presentations

* presented

M. Elfarnawany, M. R. Lowerison, M. Nicole Hague, A. F. Chambers, J. C. Lacefield, "In vivo Evaluation of An Objective Method to Select Power Doppler Wall Filter Cut-Off Frequency for Microvascular Quantification," Accepted for oral presentation at 2014 IEEE IUS, Chicago, Illinois, USA, Sept. 3-6, 2014.*

M. Elfarnawany, and J. C. Lacefield, "A New Three-Component Signal Model to Objectively Select Power Doppler Wall Filter Cut-Off Velocity for Quantitative Microvascular Imaging," Accepted for oral presentation at *SPIE Medical Imaging*, Florida, USA, Feb. 9–14, 2013.

M. Elfarnawany, and J. C. Lacefield, "A New Three-Component Signal Model to Objectively Select Power Doppler Wall Filter Cut-Off Velocity for Quantitative Microvascular Imaging," Accepted for oral presentation at 8th International Conference on Ultrasonic Biomedical Microscanning (UBM) ST-Paulin, Quebec, QC, Sept. 24-27, 2012.*

M.Elfnawany, S. Z. Pinter and J. C. Lacefield, “Improved Objective Selection of Power Doppler Wall Filter Cut-Off Velocity for Accurate Vascular Quantification,” Accepted for poster presentation at Canadian Institute of Health Research (CIHR) Symposium on Novel Cancer Therapies and Innovations in Treatment Monitoring, Toronto, ON, Nov. 14-1, 2011.*

M. Elfnawany, S. Z. Pinter and J. C. Lacefield, “Improved Objective Selection of Power Doppler Wall Filter Cut-Off Velocity for Accurate Vascular Quantification,” Accepted for oral presentation at 6th Canadian Student Conference on Biomedical Computing and Engineering (CSCBCE), London, ON, May 26-28, 2011.*

M. Elfnawany, S. Z. Pinter, and J. C. Lacefield, “Improved method for objective selection of power Doppler wall filter cut-off velocity for microvascular imaging,” Accepted for oral presentation at 160th Meeting of the Acoustical Society of America, Cancun, Mexico, Nov. 16-19, 2010, with published abstract in *J Acoust Soc Am* vol. 128, pp. 2304, 2010.*

Professional Societies

Institute of Electrical and Electronics Engineers (IEEE), Student Member 2008-present

Institute of Electrical and Electronics Engineers (IEEE) Women in Engineering, Member 2013-present

I Institute of Electrical and Electronics Engineers (IEEE) Young Professionals Member 2013-present